DEVELOPMENT AND APPLICATION OF TOOLS FOR AVALANCHE FORECASTING, AVALANCHE DETECTION, AND SNOWPACK CHARACTERIZATION

by

Scott Christopher Havens

A dissertation

submitted in partial fulfillment

of the requirements for the degree of

Doctor of Philosophy in Geophysics

Boise State University

December 2014

BOISE STATE UNIVERSITY GRADUATE COLLEGE

DEFENSE COMMITTEE AND FINAL READING APPROVALS

of the dissertation submitted by

Scott Christopher Havens

Dissertation Title: Development and Application of Tools for Avalanche Forecasting, Avalanche Detection, and Snowpack Characterization

Date of Final Oral Examination: 17 October 2014

The following individuals read and discussed the dissertation submitted by student Scott Christopher Havens, and they evaluated his presentation and response to questions during the final oral examination. They found that the student passed the final oral examination.

Hans-Peter Marshall, Ph.D.	Chair, Supervisory Committee
John Bradford, Ph.D.	Member, Supervisory Committee
Alejandro N. Flores, Ph.D.	Member, Supervisory Committee
Jeffrey B. Johnson, Ph.D.	Member, Supervisory Committee
Edward E. Adams, Ph.D.	External Examiner

The final reading approval of the dissertation was granted by Hans-Peter Marshall, Ph.D., Chair of the Supervisory Committee. The dissertation was approved for the Graduate College by John R. Pelton, Ph.D., Dean of the Graduate College.

ABSTRACT

Avalanche formation is a complex interaction between the snowpack, weather, and terrain. However, detailed observations typically can only be made at a single point and must be extrapolated over the slope or regional scale. This study aims to provide avalanche forecasters with tools to evaluate the snowpack, avalanche hazard, and avalanche occurrence when manual observations are not feasible.

Avalanches that occur within the new storm snow are a prevalent problem for the avalanche forecasters with the Idaho Transportation Department (ITD) along Highway 21. We have implemented a real time SNOw Slope Stability (SNOSS) model that provides an index to the stability of that layer. SNOSS has been run real time starting during the winter of 2011/2012 with model results outputted to a webpage for easy viewing by avalanche forecasters.

To further improve the accuracy of SNOSS, the model was evaluated with a large database of avalanches from the Utah Department of Transportation (UDOT). Using weather data and SNOSS results, the probability of an avalanche day producing a natural direct action avalanche was calculated using a Balanced Random Forest (BRF). In the future, we hope that the BRF can provide a probability of an avalanche occurrence given the current weather and snowpack conditions that can be utilized by avalanche forecasters in their normal operations.

The concern for avalanche forecasters with highway operations is the threat of an avalanche releasing and hitting a highway. Infrasound generated by an avalanche moving downhill can be detected and tracked using array processing techniques. This will allow avalanche forecasters to evaluate the avalanche hazard more effectively by

determining when and where avalanches have occurred. An avalanche detection system has been developed to detect avalanches in near real time using infrasound arrays. The system processes the infrasound data on-site, automatically detects events, and classifies the events using multiple neural networks. If an avalanche has been detected, the system will transmit the necessary information over satellite to be viewed by avalanche forecasters on a webpage.

TABLE OF CONTENTS

LIST OF TABLES

LIST OF FIGURES

CHAPTER 1:

INTRODUCTION

Avalanches occur when the snowpack fails, releasing a portion of the snowpack that begins to rapidly move downslope. The failure can occur when a cohensionless surface layer releases or as a cohesive block of snow that produces a loose snow avalanche or slab avalanche, respectively. Slab avalanches are a cohesive block of snow that fractures at a weak layer and can propagate for large distances before moving downslope. The failure layer for slab avalanches occurs on a buried layer due to new snow instabilities or on a persistent weak layer.

In the United States, most avalanches occur in remote mountainous regions and do not have a direct impact on infrastructure. When avalanches do pose a threat to infrastructure, they can prove hazardous to residential construction, highways, railroads, mountain travelers, utilities, commercial/industrial use, ski areas, and recreational users (*Mears*, 1992). In Ketchum, Idaho, homes are encroaching on avalanche terrain and the number of avalanche incidents are on the rise (*Kellam*, 2012). Interstate 90 in Washington was closed for 89 hours in January-February 2008, which produced an estimated economic loss of just under $28 million dollars (*Ivanov et al.*, 2008).

Avalanche occurrence is difficult to predict due to a complex interaction of the snowpack, weather, and terrain. Avalanche forecasters and backcountry recreationalists must continually evaluate these factors to determine the current avalanche hazard. What makes predicting avalanches difficult is not only the interaction of the three

factors (Figure 1.1), but also the complexities within each factor. For an avalanche to occur, the snowpack must be unstable, which can be caused from too much load on an internal weak layer. Understanding the snowpack at a single point on a slope can be helpful but the snowpack properties can change drastically over short length scales due to weather and terrain factors.

The weather plays an important role in applying an increased load to the snowpack either from new precipitation or wind deposited snow. When a new layer forms and becomes part of the snowpack, there is possibility that the layer may become the instability within the snowpack. Even clear weather can adversely affect the snowpack through the formation of near surface facets or surface hoar that occur due to the energy balance at the surface.
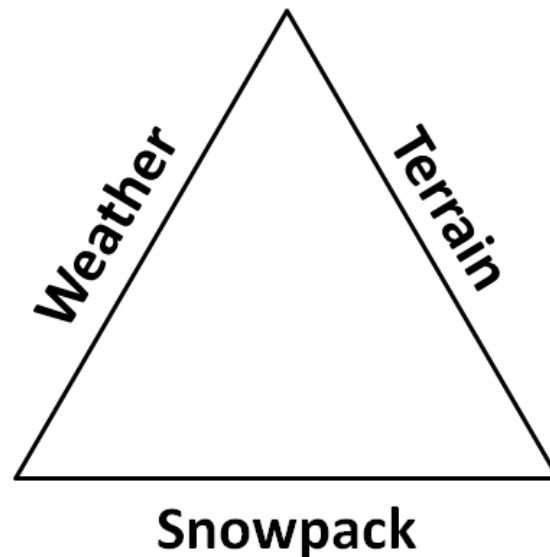
Figure 1.1: Interaction of factors that can lead to an avalanche.

A slope must be steep enough to avalanche. A flat field will never produce an

avalanche because the terrain is not capable of such an event. Therefore, a slope (typically 38°) is required to begin moving the snowpack downhill after release. There are many terrain factors that can lead to stability or instability within the snowpack. For example, a convexity in the slope will put the snowpack layers under greater stress, making it easier to trigger an avalanche.

These three factors - snowpack, weather, and terrain - must work together to create an unstable slope. The factors can produce a highly spatially variable snowpack that is difficult to evaluate. My work focuses on how to use snowpack properties at a point, either measured or modeled, and how to relate those properties to avalanche occurrences.

1.1   Snow Slope Stability at a Point

The snowpack is a collection of different layers that form from new or blowing snow. The different layers lead to stability problems when two snowpack layers have large differences in grain size, grain type, and hardness. The snowpack can be estimated with models that use weather data like precipitation and air temperature to model the snowpack (e.g., SNOWPACK *Bartelt and Lehning*, 2002; *Lehning et al.*, 2002a,b). The models can provide insight as to how the snowpack is evolving through time when manual snowpack observations are not feasible.

Snowpack models not only model the snowpack evolution, but can also provide an estimate of the snow stability (e.g., SNOSS *Conway and Wilbour*, 1999). However, the models must assume a simplified failure mode. Given multiple layers within a snowpack, the shear strength of each layer can be estimated. As the overburden load due to new snow increases and begins to reach the shear strength of the layer,

avalanches are expected to occur within a region. Modeling the snowpack over a large landscape can be very problematic as both weather and terrain factors must be taken into account, which leads to a complex spatially distributed snowpack.

1.2   Measuring Snowpack Properties

The snowpack at a point must be evaluated to determine the snowpack properties, either for stability assessment or model validation. The current method of measuring snowpack properties is through a manual snow pit that is highly dependent on observer skill. Manual snow pits can contain errors in the location of layer boundaries, grain size, and grain type (*Pielmeier and Schneebeli*, 2003). Therefore, a robust method to quickly characterize snowpack properties is needed.

The Snow Micro Penetrometer (SMP, *Schneebeli and Johnson*, 1998) is an instrument that takes mechanical snowpack profiles at speeds much greater than a traditional snowpit. The signal from the SMP (Figure 1.2) can be used to estimate snowpack properties like grain type, grain size, hardness, and strength. Certain microstructural properties estimated through the SMP inversion procedure agree well with previous studies of measured parameters and make physical sense, while others do not (*Marshall and Johnson*, 2009). Using tools like the SMP can provide a method of characterizing the snowpack that is faster and can provide more spatial information than a traditional snowpit for both stability and model verification.

The SMP signal and the resulting microstructural and micromechanical properties have distinctive values depending on the grain type. A database of SMP and manual snow pit profiles from Colorado and Switzerland provide a method to test if the SMP signals for three grain types can be differentiated. The estimated microstructural and

micromechanical properties from the SMP can then be used to classify the snowpack into precipitation particles, rounded grains, and faceted grains.

Figure 1.2: The Snow Micro Penetrometer being used to evaluate snowpack layering.

1.3 Understanding Where and When Avalanches Occur

The best way to evaluate the stability of the snowpack is avalanches. If an avalanche has occurred recently, there is a high probability that the snowpack is unstable and precautions should be taken when traveling. However, knowing when and where an avalanche has occurred can be a difficult task as we may not see exactly

when an avalanche occurred until a much later time. We are left to hypothesize when the avalanche occurred based solely on our understanding of the current snowpack and weather conditions.

Avalanches emit low frequency noise (1-10 Hz *Bedard Jr. et al.*, 1988) that is below the level of human hearing. Using instruments that are sensitive to infrasound (1-20 Hz band), we aim to detect avalanches that occur within a small mountainous region. This information will be valuable for highway department avalanche forecasters as large avalanches can be detected to determine if a road has been affected. Information on smaller avalanches that do not affect a road can be useful as an indicator of the instability being released from the snowpack.

To properly tune an avalanche forecasting model, the avalanche times must be known with some accuracy. Infrasound provides a method to accurately determine the avalanche time for a small region. The time can be fed back to the forecasting model, like SNOSS, to ensure that modeled stability is low when the avalanches are occurring. *Chritin et al.* (1996) used infrasound arrays to determine avalanche times, which updated a nearest neighbor forecasting model. Infrasound combined with a forecasting model tuned to actual avalanche times can provide avalanche forecasters with the ability to not only forecast when an avalanche may occur, but detect when and where avalanches are occurring.

To understand where and when avalanches occur, I used infrasound arrays placed near major avalanche paths. With the infrasound arrays, I have developed new methods to detect and track avalanches and demonstrate how to calculate the velocity of one avalanche; as such, I have developed a real time avalanche detection system using infrasound.

1.4 Dissertation Organization

This dissertation is organized to address point scale measurements of the snow-pack. Appendix A reviews the current knowledge of snow densification. Chapter 2 and 3 evaluate the SNOw Slope Stability (SNOSS) model at a point. The goal is to use SNOSS as a tool to help avalanche forecasters evaluate avalanche hazard. By applying SNOSS to a large dataset of avalanche and weather observations, factors that produce natural avalanches can be explored.

Chapter 4 shows how the SMP can be used as a tool to classify grain types in support of remote sensing validation campaigns. The differences in grain types within the snowpack affect remote sensing measurements of snow water equivalent (SWE) and are an important factor to include in SWE retrieval algorithms. A relatively new classification technique is applied to a large database of SMP measurements in different types of snow in Switzerland and Colorado.

Chapter 5 provides the background information on avalanche infrasound generation, current infrasound research, and array processing techniques. Chapter 5 and Chapter 6 use infrasound emitted by avalanches to detect and track where and when an avalanche occurs. Four winters of avalanche activity have been recorded along Highway 21 in Central Idaho. Automatic avalanche detection is explored using array processing techniques combined with non-parametric background modeling to determine when infrasound signal is present (Chapter 5). In Chapter 6, I calculate the avalanche velocity of a fast moving avalanche at a high spatial and temporal resolution.

Chapter 7 describes the real time avalanche detection system developed for the Idaho Transportation Department. The goal of the project is to use an infrasound

array to detect when and where an avalanche occurs in real time. When an avalanche is detected by the on-site computer processing the data in near real time, the system will send out a message to alert the avalanche forecasters of the event.

Appendix B provides a literature review of seismic detection of avalanches. Detection with infrasound will borrow heavily from the seismic community and understanding the latest in seismic detection is critical.

1.5 Published Papers

Two chapters in this dissertation have been published in peer reviewed journals. The first paper was titled "Automatic Grain Type Classification of Snow Micro Penetrometer Signals with Random Forests" and was published in *IEEE Transactions on Geoscience and Remote Sensing* (*Havens et al.*, 2013). This paper is shown in Chapter 4.

The second paper was titled "Calculating the Velocity of a Fast Moving Snow Avalanche Using an Infrasound Array" and was published in *Geophysical Research Letters* (*Havens et al.*, 2014). This paper is shown in Chapter 6.

CHAPTER 2:

REAL TIME SNOW SLOPE STABILITY

MODELING

2.1   Research Project Statement

Avalanches routinely occur on Highways 21 and 12 each winter, posing a safety threat to maintenance workers and the traveling public. Currently, avalanche forecasters based in Lowman, ID forecast for Highway 21 between Grandjean and Stanley, ID and Highway 12 near Lolo Pass, ID. An avalanche forecasting model would provide avalanche forecasters with an additional tool when evaluating the possibility of avalanche activity. The work aims to enhance avalanche forecast accuracy, especially during darkness and for highway areas (like Highway 12) a long distance from the forecast office. During times of avalanche activity, Highway 21 routinely closes until the end of an avalanche cycle and reopens after the clean up effort. The goal of the ITD avalanche forecasters is to maintain the public safety while trying to keep Highway 21 open (Figure 2.1).

2.2   Study Site

The Idaho Transportation Department produces forecasts for Highway 21, located 2.5 hours (170 kilometers) northeast of Boise, Idaho (Figure 2.2). The study area is in an intermountain climate, which typically sees moderate snowfall (300 inches
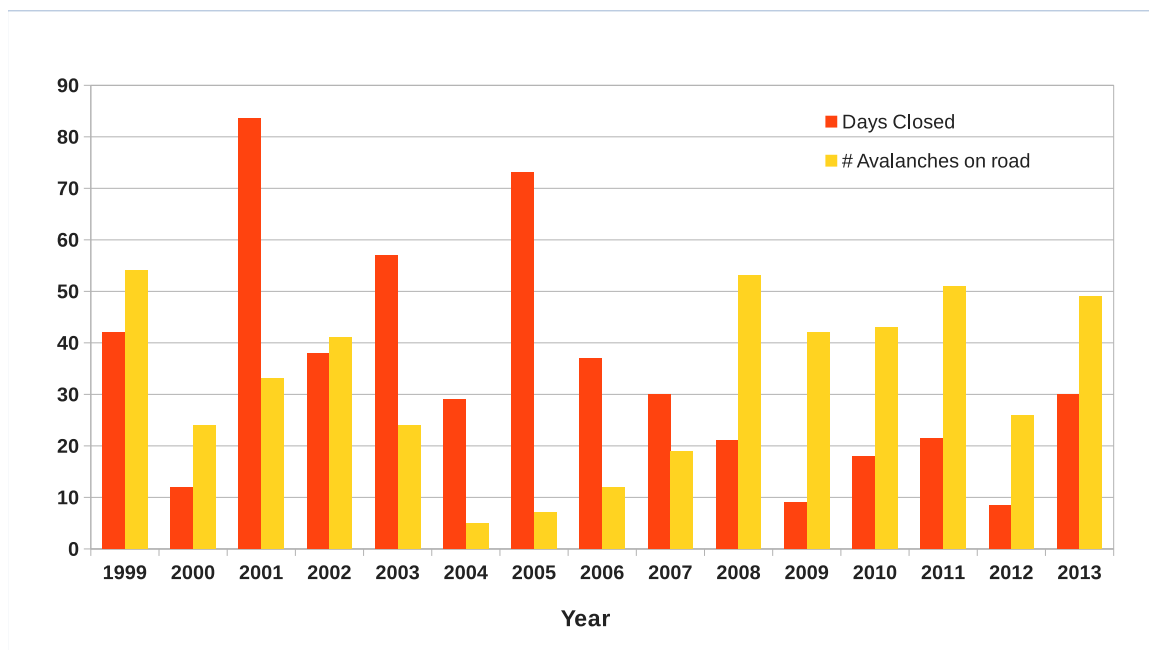
Figure 2.1: The number of avalanches that hit Highway 21 in relation to the number of days Highway 21 is closed.

average), extremely cold temperatures between storms (-30 to -15 C), and rain on snow events throughout the winter. ITD has a limited explosive avalanche mitigation program due to the complex terrain in the start zones and the highway location. Avalanche activity is mostly direct action avalanches due to storm snow or rain on snow, with at least one major wet slide cycle during the spring. Both lanes of Highway 21 are frequently covered during avalanche cycles and the road is often closed for several days at a time.

Highway 12, located near Lolo Pass, ID is approximately 7 hours (520 kilometers) north of Boise, Idaho (Figure 2.2). The area has a more maritime snowpack that is representative of warmer temperatures and a dense snowpack. Maritime climates typically do not have persistent weak layers and are more prone to direct action avalanches within the new storm snow. Highway 12 is at a low elevation (900 to 1800

meters above sea level) and frequently encounters rain on snow events.
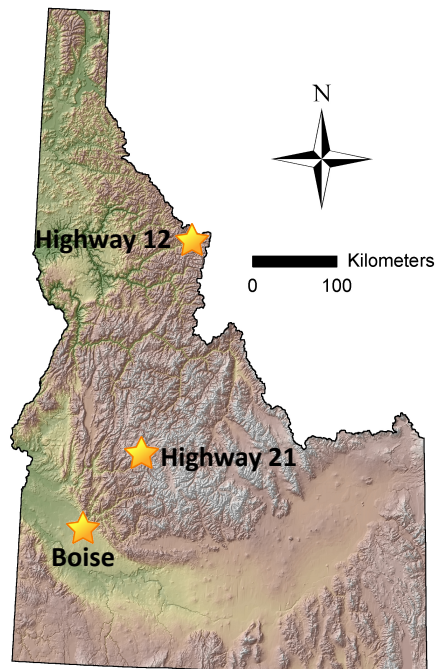
Figure 2.2: Location of current avalanche forecasting operations by ITD for Highway 21 and Highway 12.

2.3   SNOw Slope Stability Model

The SNOw Slope Stability (SNOSS) model developed by *Conway and Wilbour* (1999) is a simple one-dimensional avalanche forecasting model comparing the overburden shear stress caused by new snow to the strength throughout the snowpack. SNOSS is currently used operationally on I-90 at Snoqualmie Pass, WA, and on the Milford Road in New Zealand.

2.3.1 Overburden Shear Stress

The stress applied by the snow slab in the down slope direction is the overburden shear stress $\sigma_{xz}(t)$. The shear stress is a function of the amount of overburden snow above a given layer and a function of time as more snow layers are added from precipitation events. The shear stress at the base of the layer is dependent on the weight of water above the layer and is formulated as:

$$\sigma_{xz}(t) = g \int \dot{P}_w \cos\theta \sin\theta \, dt \tag{2.1}$$

where g is the gravitational constant, $\dot{P}_w$ is the accumulation rate, and θ is the slope angle (Figure 2.3). The accumulation rate is measured at precipitation gauges, typically at hour increments.
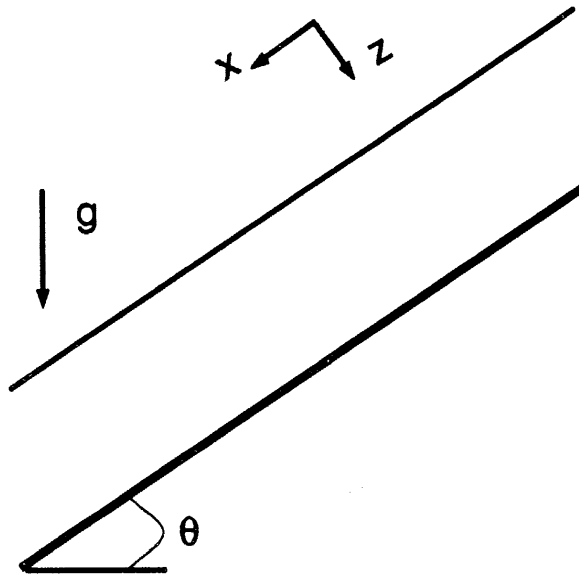
Figure 2.3: A planar snow slab on an incline θ. From *Conway and Wilbour* (1999).

2.3.2 Basal Shear Strength

The strength of a weak layer is highly dependent on snow microstructure and crystal type. A first order approximation of a weak layers shear strength is to relate the shear strength to the snow density. *Jamieson* (1995) performed numerous field measurements of shear strength of persistent weak layers and their associated density. Jamieson's results show a power law relationship between shear fracture strength and density:

$$\sigma_f = A_1 \left(\frac{\rho_s}{\rho_i} \right)^2 \tag{2.2}$$

where ρ_s and ρ_i are the density of snow and ice respectively. The parameter A_1 is estimated from the measurements and varies from 1.8×10^4 Pa for faceted grains to 2.2×10^4 Pa for decomposing new snow with the best fit to all the measurements of $A_1 = 1.95 \times 10^4$ Pa. However, Figure 2.4 shows a large range in strength for any given density, which can be attributed to different grain types or microstructural differences.

2.3.3 Snow Densification

The viscosity relates the stress to the strain rate through the following constitutive equation:

$$\dot{\epsilon} = \frac{\sigma}{\eta_z} \tag{2.3}$$

where η_z is the compactive viscosity of the snow layer. The overburden stress $\sigma_{zz}(t)$ contributes to the stress applied to the snow layer and for an inclined snowpack $\sigma_{zz}(t) = g \int \dot{P_w} \cos^2 \theta dt$. The metamorphic component σ_m will range from positive for equilibrium metamorphism to negative for kinetic growth metamorphism. The
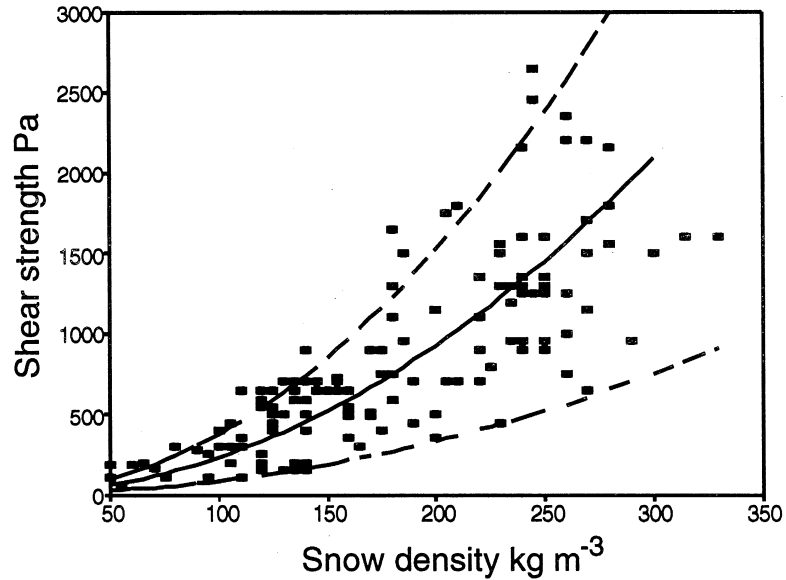
Figure 2.4: The relationship between shear stress σ_f and snow density ρ_s can be represented by a power law relationship. From *Jamieson* (1995).

metamorphic component has a value of 75 Pa during a storm, where we expect equilibrium metamorphism to dominate especially near the surface when $\sigma_{zz}(t) \approx 0$ (*Marshall et al.*, 1999). A snow layer with thickness h and density ρ compacted over a time t will have a thickness of $h - dh$ and density of $\rho + d\rho$. Therefore, the new constitutive equation is:

$$\dot{\epsilon}(t) = -\frac{1}{h(t)}\frac{dh}{dt} = \frac{1}{\rho(t)}\frac{d\rho}{dt} = \frac{1}{\eta_z(t)}\left[\sigma_m(t) + \sigma_{zz}(t)\right] \tag{2.4}$$

Kojima (1967) performed numerous field measurements over multiple seasons to relate the compactive viscosity to the snow layer density. *Conway and Wilbour* (1999) modified the viscosity with an Arrhenius type temperature term to take into account

the affect of layer temperature on snow densification:

$$\eta_z(t) = B_1 e^{B_2(\rho_z(t)/\rho_i)} e^{E/(RT_z)} \tag{2.5}$$

where $B_1 = 6.5 \times 10^{-7}\,\mathrm{Pa\,s}$, $B_2 = 19.3$, the activation energy $E = 67.3\,\mathrm{kJ^{-1}\,mol^{-1}}$, the gas constant $R = 0.0083\,\mathrm{kJ\,mol^{-1}\,K^{-1}}$, and the layer temperature T_z in Kelvin.

2.3.4 New Snow Density

Equation 2.4 requires an estimate of the density of any new snow layer. New snow density is not measured at the hourly time scale and must be estimated with a representative model (reference unknown).

$$\rho_0 = 134.2 e^{(19.95T_a)/(273+T_a)} \tag{2.6}$$

where T_a is the air temperature in Celsius. This approximation has a significant amount of uncertainty since it does not take other weather parameters into account, like wind.

2.3.5 Stability Index

The ratio of the shear strength σ_{fz} to the overburden shear stress σ_{xz} is the stability index (*Fohn*, 1987) and is calculated for each layer at depth z:

$$\overline{\Sigma}_z(t) = \frac{\sigma_{fz}(t)}{\sigma_{xz}(t)} \tag{2.7}$$

As the value approaches 1, the probability of an avalanche theoretically increases. However, past studies have shown that avalanches typically occur at a higher stability index value (e.g., above 1.4), which varies between sites (*Conway and Wilbour*, 1999; *Lehning et al.*, 2004; *Schweizer et al.*, 2006). This is possibly due to a difference in model forcings and snowpack properties between available weather stations and starting zones.

2.3.6 Time to Failure

The time to failure is the expected length in hours until the critical stability index is reached. The time to failure assumes the current conditions stay the same and the slope of the stability index at the current time does not change.

$$t_f(t) = \frac{\overline{\Sigma}_z(t) - \overline{\Sigma}_c}{d\overline{\Sigma}_z/dt} \tag{2.8}$$

where $d\overline{\Sigma}_z/dt$ is the slope of the stability value for the layer at the current time and $\overline{\Sigma}_c$ is the critical stability index value, typically set to 1 when failure is expected as the overburden shear stress reaches the layers shear strength.

2.3.7 Model Calibration

SNOSS calibration can be performed in two ways: 1) snow densification and 2) avalanche times. Calibrating snow densification targets the equations in Section 2.3.3 that attempt to reproduce how the snowpack density changes through time. To perform the calibration, I took the measured snow depth from the weather station at Banner Summit and compared with the modeled SNOSS snow depth. The viscosity

parameters were determined by changing $B1$ and $B2$ until the root mean square error (RMSE) was minimized. The results produced $B_1 = 2.69 \times 10^{-8}\,\mathrm{Pa\,s}$ and $B_2 = 30.27$, which are significantly different than the values found for the maritime climate of Washington in *Conway and Wilbour* (1999).

The second step of calibration is avalanche times, which are used to calibrate the basal shear strength (Equation 2.2) and provide insight into the significant values for the stability index and time to failure. However, determining when an avalanche has occurred can prove problematic along Highway 21 as the road can be closed for multiple days at a time, making visual confirmation of an avalanche occurrence not possible for hours to days after the avalanche event. What is required for proper calibration is sub hourly resolution of when the avalanche events occurred. To perform the calibration, we have deployed infrasound arrays to detect when and where an avalanche has occurred (Chapter 5) but the catalog of avalanche events is still under development.

2.4   Real Time Application

Three independent processes occur simultaneously in the real time application (Figure 2.5) and all the algorithms were setup by me. The first process obtains weather data for all the desired weather stations and stores the data in a database. The second process runs SNOSS given the weather data and stores the results in a database. The third process uses a webpage to access the weather and SNOSS results databases for easy viewing. Each process is described in detail below.
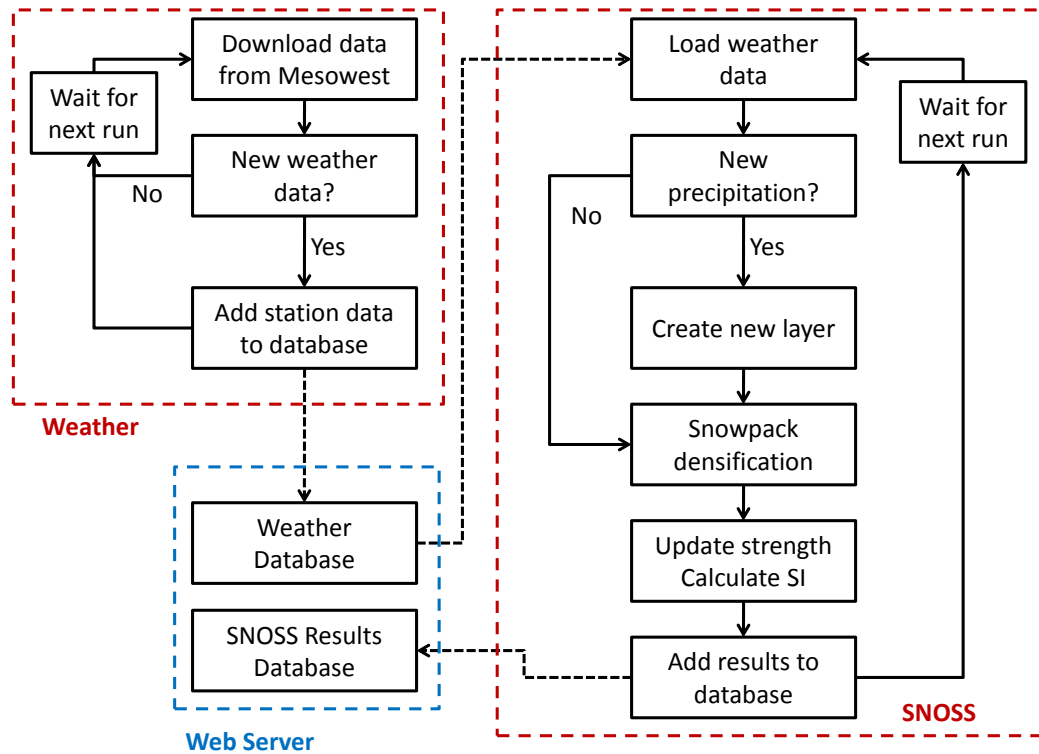
Figure 2.5: Flow chart for real time application of SNOSS. Three independent processes occur to obtain weather data, run SNOSS, and view the results on a webpage.

2.4.1 Weather Data

Mesowest collects, processes, archives, integrates, and disseminates weather data collected from over 43,000 automated weather stations (*Horel et al.*, 2002). Mesowest has two methods for obtaining real time data: first through a file located on their FTP server, which is updated four times an hour. The second method is in beta testing but uses an Application Programming Interface (API) to provide data through a web service. For this project, the weather data is downloaded from the FTP server.

The weather data is downloaded using a Python script that runs four times an hour on a server. The script downloads the data file from the FTP server and looks

through the file for the desired weather stations. If the weather station is found, the data is added to a MySQL database (Figure 2.5). Typically, new weather data is available approximately 20 to 30 minutes after the measurement.

2.4.2 SNOSS

The real time application of SNOSS can be run for any weather station with a minimum of hourly temperature and precipitation measurements. SNOSS is run four times an hour to ensure the most up to date results. When only one new measurement exists for a station, the processing time is less than one second and 2,100 hourly measurements can be processed in approximately 10 seconds.

The flow chart in Figure 2.5 outlines the processing flow for SNOSS. For each weather station, the previous SNOSS results are loaded along with new weather data obtained since the last model run. If there is precipitation for that time step, a new layer is created with an initial density based on the air temperature. The algorithm proceeds with snow densification given the overburden and viscosity for each layer (Equations 2.4 and 2.5) and the new layer densities are calculated. Given the new layer densities, the shear strength is updated. Finally, the stability index (Equation 2.7) is calculated for each layer with the new strength and overburden.

To keep the displayed results simple, the avalanche forecaster for ITD requested to plot only the most likely failure layer. At each time step, the layer with the minimum value of the stability index becomes the potential failure layer. Information about the layer is extracted and saved to a MySQL database.

2.4.3 Displaying Results on a Webpage

Over the life of the project, the results have been presented on a webpage in three different iterations, which are listed below.

1) First MATLAB Figures

The first results (Figure 2.6) tracked the basal layer from the beginning of the current storm. After 12 hours of no new precipitation, SNOSS began tracking the basal layer of the next storm, when precipitation resumes. However, tracking only the basal layer posed problems if the possible failure layer was not the basal layer due to initial density changes within the new snow.

Figure 2.6 shows the typical results displayed for the winter of 2011/2012 and how to interpret the figure. The figures were created in MATLAB and uploaded to the web server where the avalanche forecasters could look at the image. The figure worked well initially, but was not as informative or straight forward to interpret. If the basal layer was not the failure layer, the figure would not be able to effectively communicate the other potential weak layer.

2) Second MATLAB Figures

During the 2011/2012 season, ITD avalanche forecasters used SNOSS to determine qualitatively what values of the stability index and time to failure were useful for predicting direct action avalanches. The avalanche forecasters found that the time to failure was not as relevant for Highway 21. Therefore, a new results figure was created to improve on the previous figure and supply more information. The new figure (Figure 2.7) included the hourly precipitation and temperature measurements
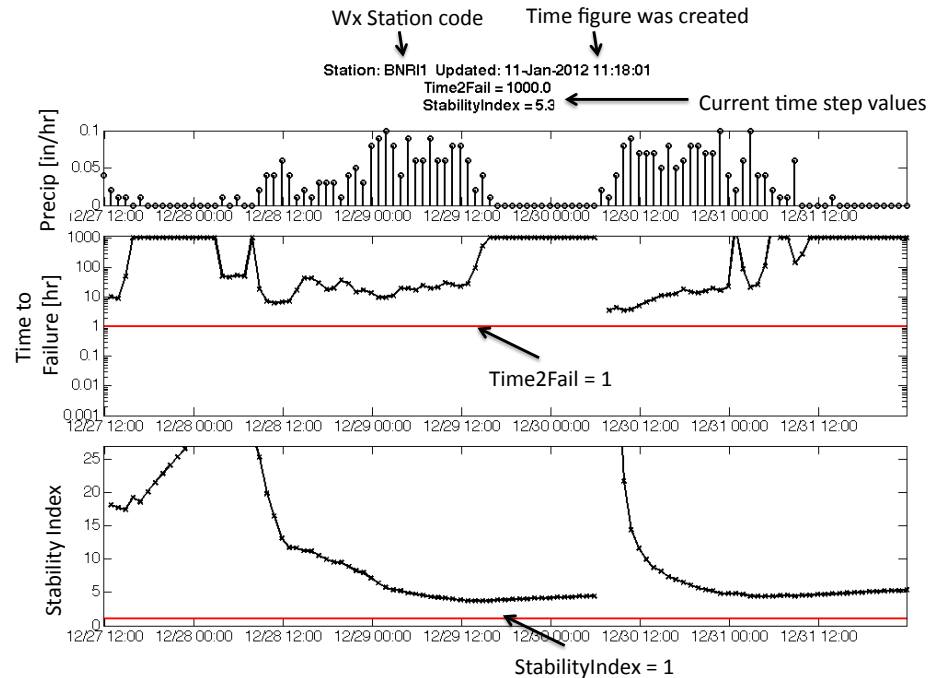
Figure 2.6: Real time SNOSS webpage output, updated when a new weather measurement is acquired. The top panel shows the hourly precipitation measurement, the middle panel is the time to failure, and the bottom panel is the stability index.

used in the model. Below the inputs, the minimum stability index value is found at each time step instead of tracking the basal layer. The minimum stability index value and the corresponding depth to that layer are displayed. To the right is an image of the modeled snowpack colored by the stability index value. This allows the forecasters to see other potential failure layers within the new snow. The figure was created in MATLAB and uploaded to the web server after the model was run.
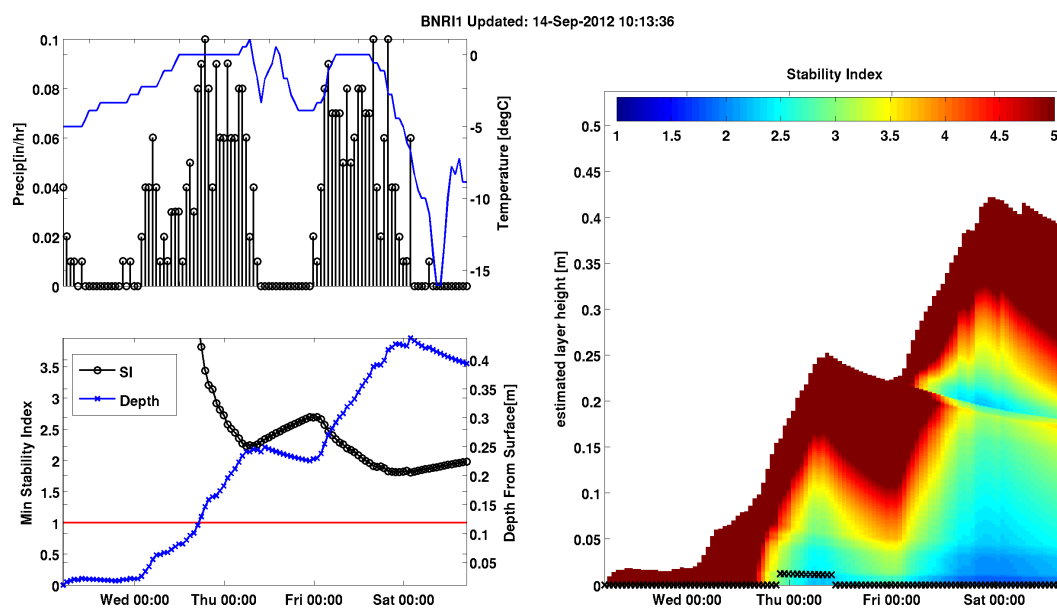
Figure 2.7: The new results figure was used starting for the 2012/2013 winter, which includes hourly precipitation, temperature, minimum SI and the estimated depth, and the SI for all layers.

3) Web-Based Plotting Charts

Figures created in MATLAB are difficult to interact with and do not provide an easy way to look up past data without storing all of the past images. Many options exist for web-based plotting; I chose to use jqPlot (www.jqPlot.com) which is a javascript/jQuery based plotting library. jqPlot was chosen due to the elegant look and its ability to interact with the data.

On the webpage, the user can select the date range and weather station from which to display data. The server loads the desired data from the weather and SNOSS databases given the date range and station. The webpage uses tabs to display the weather data and SNOSS results (Figure 2.8) to help organize the look of the webpage. Each data point on the chart can be highlighted to provide the time and value of

that point. Web-based plotting allows the ITD avalanche forecasters an easy and interactive method to look at weather and SNOSS results.
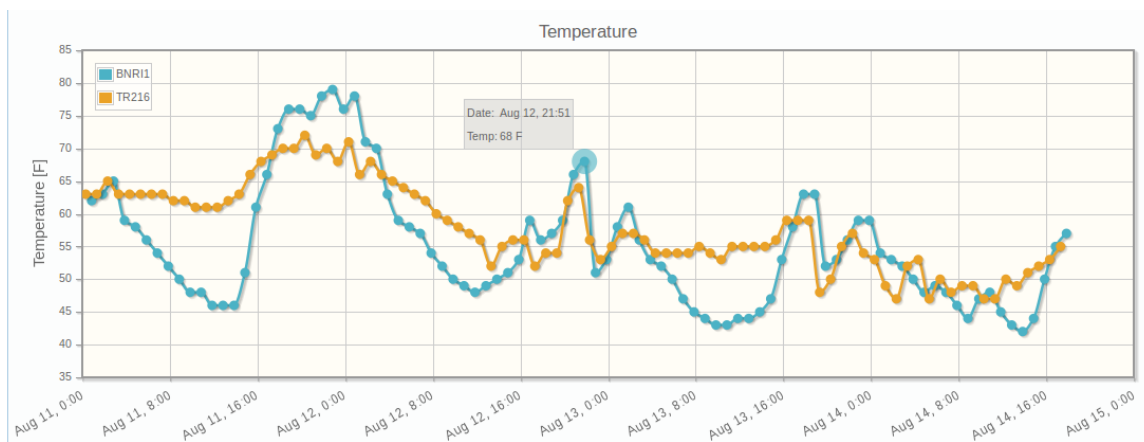
Figure 2.8: Example of the new webpage design with new charts to display the weather and SNOSS results. Hovering over a data point brings up a tool tip and shows the time and value of the point.

2.5   Conclusion

The simple 1-D snow densification model SNOSS forecasts for direct action avalanches using the stability index. I have adapted SNOSS to run in real time and provides the ITD avalanche forecasters an additional tool for their avalanche forecasting operation. SNOSS runs by using weather data obtained from Mesowest and models how new snowfall creates instability within the new snow. The SNOSS results are displayed on a webpage using an elegant and interactive plotting library. The charts allow the ITD avalanche forecasters to look quickly at weather and model results for any desired date and station.

A large avalanche cycle occurred in mid-January 2012 that produced 57 avalanches during the storm (see Chapter 6 for more information). Infrasound arrays were in-
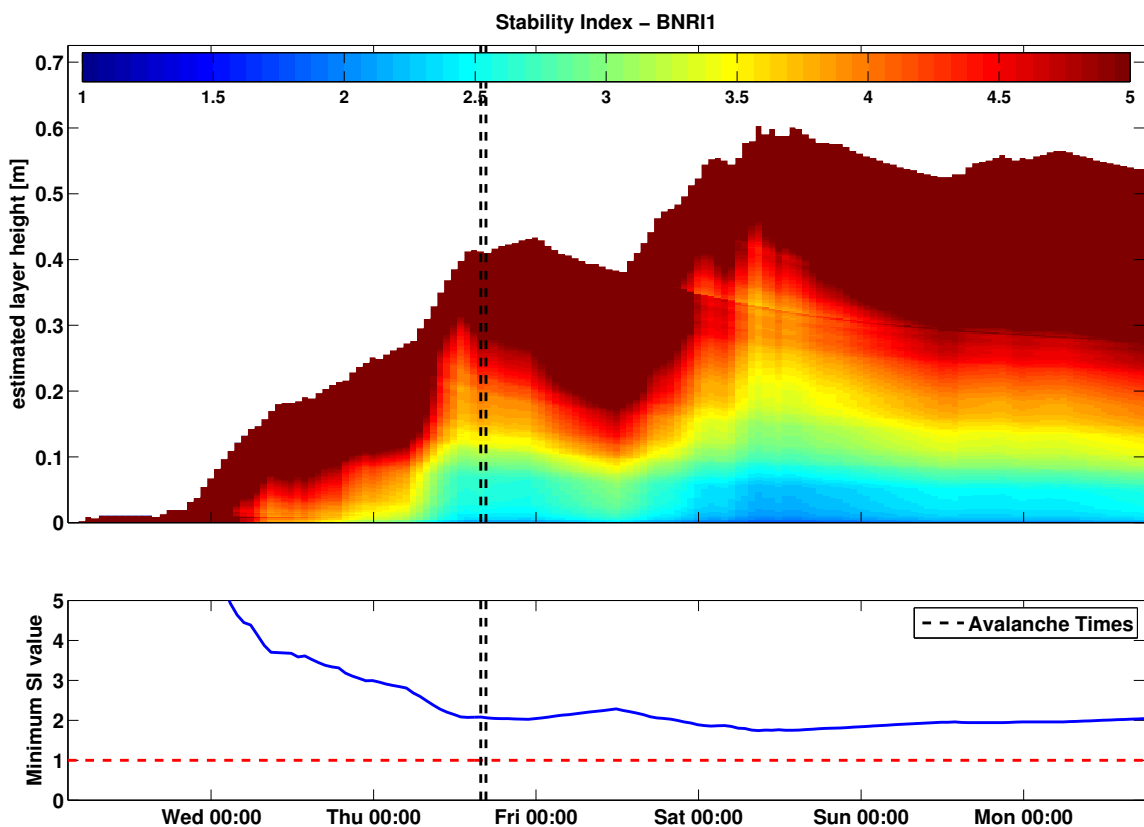
Figure 2.9: SNOSS model output of the stability index for a large storm that produced 57 avalanches (more avalanche cycle information in Chapter 6). The black lines indicate two avalanche events that were identified through infrasound.

stalled around the major avalanche paths, but due to wind and array power problems, only 2 avalanches were confirmed in the infrasound data. Figure 2.9 compares the SNOSS stability index for the entire storm and the minimum values for each hour with the two known avalanche times. When the two avalanches occurred, the minimum stability index value was just above 2 right as the first part of the storm was ending. The minimum value occurred at the base of the new snow, which was the expected failure layer for the avalanche cycle. This single example shows the potential for SNOSS to be used by avalanche forecasters, however, more storm, snowpack, and

avalanche validation data will be required to fully understand the SNOSS results that indicate potential avalanche hazard.

CHAPTER 3:

AVALANCHE CLASSIFICATION WITH BALANCED RANDOM FORESTS AND SNOWPACK MODELING

3.1   Abstract

Improved prediction of the timing of direct action avalanches that occur during storms is needed for highway forecasting operations. The SNOw Slope Stability model (SNOSS) compares the overburden stress caused by new snow to the estimated strength within the new snow. This provides estimates of the stability of the new snow layer and whether a regional direct action avalanche cycle can be expected. The Utah Department of Transportation in Little Cottonwood Canyon has a unique dataset of weather and avalanche observations dating back to the early 1970s. SNOSS results and weather data were used in Balanced Random Forests to determine the probability of a natural storm related avalanche from avalanche occurrence information. Results show a low classification rate of 57% to 67% depending on the combinations of variables used. The most important variables for classification were the 48 hour maximum air temperature at the peak, the 48 hr minimum snow drift factor, the 48 hr SNOSS stability index value, and the 12 hr estimated layer strength from SNOSS.

3.2   Introduction

Avalanche forecasting models ingest weather and snowpack data in order to determine if the complex interaction of weather and snowpack data will lead to avalanche activity. Similar to an avalanche forecaster, the model attempts to use the available weather, snowpack, and avalanche information to determine if the current and future conditions will lead to avalanche activity. Avalanche forecasting models will not replace the experience and knowledge of an avalanche forecaster any time soon, but will help communicate how the multitude of information relates to avalanche activity.

Previous studies have primarily used meteorological data to predict avalanche activity. The classification schemes use either manually collected weather data (*Davis et al.*, 1999; *Floyer and McClung*, 2003) or data from automatic weather stations (*Hendrikx et al.*, 2005; *Cordy et al.*, 2009; *Eckerstorfer and Christiansen*, 2011). The most popular method is to forecast avalanche days (i.e., whether or not an avalanche has occurred over a specified time window). These studies reported results that vary between a 70-85% correct classification rate for both natural and artificially released avalanches. The model results are simple to interpret but require a significant amount of past avalanche data to test the model. Classification performance improves with the quality of the meteorological data available.

The limitation of statistical avalanche forecasting models based on weather data is the lack of information of the snowpack properties. For example, information about existing weak layers within the snowpack is not used nor estimated, since acquiring hourly or daily snowpack data is not feasible for most areas. Furthermore, predictive models applied to different locations have different model parameters and predictor variables, requiring tuning for each individual site. Tuning requires a large historical

data set for calibration to produce robust results.

Snowpack modeling can provide the required hourly snowpack property information that would be needed for avalanche forecasting models. Snowpack models typically use a minimum of hourly precipitation and temperature measurements, and from these measurements construct and evolve the snowpack through time. The physically based SNOWPACK model (*Bartelt and Lehning*, 2002; *Lehning et al.*, 2002a,b) has been used to create snow profiles during times of avalanche activity. Measured snowpack stability from pit and Ruchblock tests were compared with SNOWPACK outputs of snow strength to evaluate how well SNOWPACK can determine stability rating (*Lehning et al.*, 2004; *Schweizer et al.*, 2006; *Schirmer et al.*, 2010). *Schirmer et al.* (2010) found that SNOWPACK variables were better at detecting rather stable conditions when compared with the regional avalanche hazard forecast. However, SNOWPACK has not been compared with a large database of avalanche activity to test the model results.

The French SAFRAN-Crocus-MEPRA (SCM) chain (*Durand et al.*, 1999) is an operational avalanche forecasting model that uses meteorological data as input to the snowpack model Crocus. The results from Crocus are analyzed with an expert system of rules (MEPRA) to determine if natural or skier triggered avalanche activity is likely to occur.

This study aims to use the much simpler and more computationally simple model, SNOw Slope Stability (SNOSS; *Conway and Wilbour*, 1999) to model the snowpack using only an input of hourly precipitation and temperature measurements. SNOSS models the densification of each new snow layer through time, and uses density to estimate strength (*Jamieson and Johnston*, 2001). Stability indices are calculated to

estimate avalanche regional activity.

3.3   Study Site

The Utah Department of Transportation (UDOT) has an avalanche forecasting program for the Little Cottonwood Canyon road between Salt Lake City and Alta, Utah in the Wasatch Mountains (Figure 3.1). UDOT has an extensive explosive avalanche mitigation program employing multiple Avalaunchers and large artillery. Avalanche records affecting the road date back to 1974 and provide a large dataset of high quality avalanche observations alongside a long history of weather observations. A significant amount of the avalanches in the area are direct action avalanches due to storm snow and occur during or directly after a storm. However, the climate is intermountain and can produce depth hoar at the base of the snowpack during the early season. Here we focus on slide paths with multiple events per year to target direct action events. Avalanche records between years 2001 and 2010 were used along with data from two weather stations. Alta Guard (2682 meters) measures hourly precipitation, air temperature and snow accumulation on a storm board. Alta Baldy (3373 meters) measures air temperature, wind speed, and wind direction.

3.4   SNOw Slope Stability Model

The SNOw Slope Stability (SNOSS) model developed by *Conway and Wilbour* (1999) is a simple one-dimensional avalanche forecasting model comparing the over-burden shear stress caused by new snow to the strength throughout the snowpack. A full explanation of SNOSS can be found in Section 2.3.

Little Cottonwood Canyon, Utah Avalanche Paths
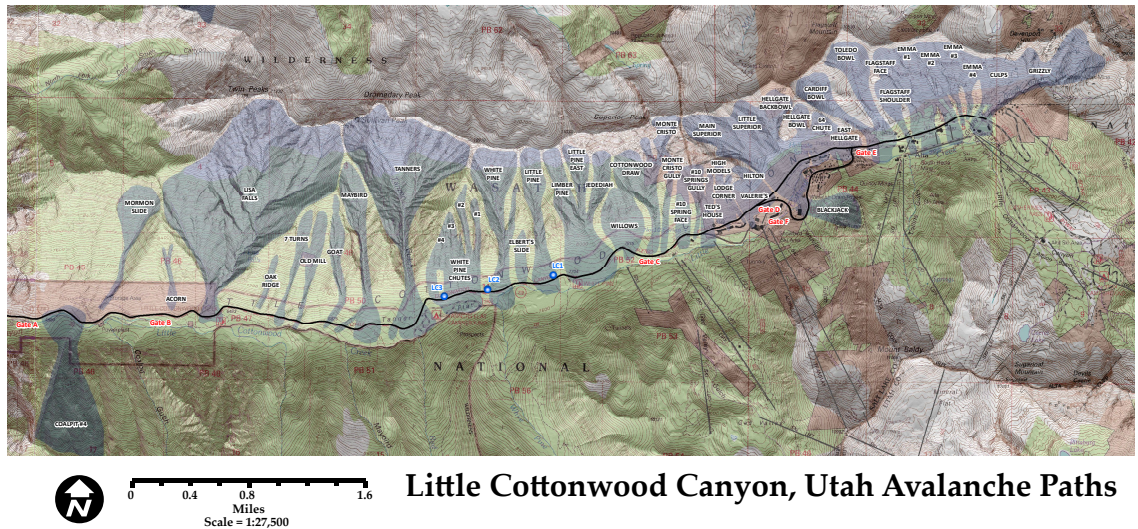
Figure 3.1: Avalanche paths along Little Cottonwood Canyon that have the ability to affect the road.

3.5 Methods

3.5.1 Natural Avalanche Days

A small subset of the total avalanche records for Utah between 2001 and 2010 were used to calibrate natural avalanche prediction. The subset was chosen because the years included weather data at an hourly resolution, which is required to run SNOSS. Each season of weather and avalanche data were searched using a moving 12-hour window. Each 12-hour window was classified as an avalanche day or non-avalanche day depending on whether or not a natural avalanche occurred within that window. Only records that contained natural avalanches that indicated direct action avalanches were included. These avalanche types are typically soft slab and loose avalanches. The non-avalanche days could not contain any type of avalanche event, including artificially released or wet avalanches as these avalanches are not applicable

for SNOSS. This ensures that the non-avalanche day does not contain any type of avalanche that would produce biased results.

Since we are looking at predicting natural avalanches that occur during storms, we want to have non-avalanche days that reflect times of significant storms. This will allow us to directly compare why certain storms produced avalanches and others did not. The criterion for a storm was more than 1.3 cm of water, less than 2 degrees C at the peak weather station, and less than 2 hours elapsed since the last precipitation measurement. These criteria produced 42 avalanche days and 358 non-avalanche days. The number of avalanches days already show that there are times of significant storms that still do not produce avalanches.

3.5.2 Meteorological and SNOSS Predictor Variables

For each avalanche day, meteorological and SNOSS predictor variables were created for the 12, 24, 48, and 72 hours prior to the end of each time window (Table 3.1). The minimum (Min), average (Avg), maximum (Max), and range (Range) values of the meteorological variables are calculated for each time window. Since total snow depth is not measured at Alta Guard, the hourly snow accumulation was determined when the snow board registered an increase in snow depth from the snow depth sensor placed on the snow board. The snow accumulation was then either summed or averaged for the time windows to create the total snow accumulation or average snow accumulation respectively. The snow drift parameter is the total water weight measured at Alta Guard multiplied by the peak wind speed raised to the fourth power (i.e., *Davis et al.*, 1999; *Hendrikx et al.*, 2005).

The hourly precipitation from Alta Guard and the air temperature from Alta

Baldy were used to run SNOSS for the 12, 24, 48, and 72 hours windows. The minimum stability index and time to failure of the new snow was restricted to the last 12 hours of model output to ensure that the minimum value occurs in the avalanche day window. At the minimum stability index value (the most likely failure layer), the depth below the snow surface, layer settlement, and layer strength were used for the SNOSS predictor variables (Table 3.1).

A total of 108 predictor variables were created: 88 from meteorological factors and 20 from SNOSS model results (Table 3.1). A different subset of the predictor variables was used to determine the most important variables for predicting natural avalanches. The subsets included:

1. All the predictor variables

2. Significant meteorological and SNOSS variables (18 total)

3. Meteorological variables

4. SNOSS variables

The significant meteorological and SNOSS variables are the most significant variables from the all predictor variables tested.

3.5.3 Balanced Random Forests

Random forests are an ensemble of single classification trees (*Breiman*, 1996, 2001). Random forests are built with random subsets of the original data and use random subsets of the predictor variables at each node. Lower error rates can be achieved with random forests versus a single classification tree. The random sam-

Table 3.1: Meteorological and SNOSS predictor variables. XX denotes the time for each of the variables. Bold variables were used for the significant variable test.

Variable Description	Symbol	Time
Alta Guard		
Sum of precipitation	BaseWaterSumXX	12, 24, 48, 72
Maximum hourly precipitation	BaseWaterMaxXX	12, **24**, **48**, 72
Average of hourly precipitation	BaseWaterRateXX	12, 24, 48, 72
Air temperature, average	BaseTempAvgXX	12, 24, 48, 72
Air temperature, minimum	BaseTempMinXX	12, 24, 48, 72
Air temperature, maximum	BaseTempMaxXX	**12**, **24**, **48**, **72**
Air temperature, range	BaseTempRangeXX	12, 24, 48, 72
Sum of snow accumulation	BaseSnowAccXX	12, 24, 48, 72
Average of snow accumulation	BaseSnowRateXX	12, 24, 48, 72
Alta Baldy		
Air temperature, average	PeakTempAvgXX	**12**, 24, **48**, 72
Air temperature, minimum	PeakTempMinXX	**12**, **24**, **48**, 72
Air temperature, maximum	PeakTempMaxXX	**12**, **24**, **48**, **72**
Wind speed, average	PeakSpeedAvgXX	12, 24, 48, 72
Wind speed, minimum	PeakSpeedMinXX	12, 24, 48, 72
Wind speed, maximum	PeakSpeedMaxXX	12, 24, 48, 72
Wind speed, range	PeakSpeedRangeXX	12, 24, 48, 72
Wind direction, average	PeakDirAvgXX	12, **24**, **48**, 72
Wind direction, range	PeakDirRangeXX	12, 24, 48, 72
Combined Meteorological Variables		
Snow drift factor, average	SnowDriftMinXX	12, 24, 48, **72**
Snow drift factor, minimum	SnowDriftMinXX	12, 24, **48**, 72
Snow drift factor, maximum	SnowDriftMinXX	12, 24, 48, 72
SNOSS		
Stability index	snossSIXX	12, 24, **48**, **72**
Time to failure	snossTFXX	12, 24, 48, 72
Layer settlement	snossDZXX	**12**, **24**, **48**, **72**
Depth from surface to layer	snossDEPTHXX	12, 24, 48, 72
Layer shear strength	snossSTRENGTHXX	**12**, **24**, **48**, **72**

pling reduces correlation between each classification tree in the ensemble leading to a stronger classifier.

Balanced Random Forests (BRF; *Chen et al.*, 2004) are used when the dataset is imbalanced. This occurs when the class of interest (i.e., avalanche occurrence) is the minority class and contains significantly less values than the majority class. Classification of imbalanced datasets is biased towards the majority class where the highest accuracy can be obtained by correctly classifying only the majority class. However, the process ignores the minority class that we are interested in classifying and understanding.

A random forest randomly samples with replacement from all the dataset values to create a bootstrap sample (B) the same size as the original data. This can lead to problems with imbalanced classes because there is a high probability that the minority class will not be well represented in B. Therefore, *Chen et al.* (2004) proposed to randomly sample with replacement from each class separately. The minority class is randomly sampled with replacement to create a bootstrap sample that is the same size as the minority class. The same number of cases is randomly sampled with replacement from the majority class. This produces a bootstrap sample with an equal number of cases from each class. Class labels may appear multiple times or not at all in B. Cases that are not selected for B are considered out-of-bag (OOB) samples. On average, $\sim$37% of the minority cases will be OOB and significantly more for the majority class.

Figure 3.2 shows a flow chart of the BRF procedure. A single classification tree is grown from the balanced bootstrap sample using a random subset of the predictor variables at each node. The randomization of the predictor variables strengthens the

predictive power and reduces correlation between trees in the ensemble. The random selection of B was repeated for the desired number of trees, each time storing the OOB cases and the classification tree to create a BRF.

To make a prediction, the predictor variables are run through the BRF, producing a predicted class from each tree. In the majority of random forest studies, the class with the highest probability of classification is the predicted class. However, in this study, we are more interested in the probability of an avalanche given the current weather and snowpack model. The probability of an avalanche is determined from the number of trees predicting a class over the number of trees in the random forest. A high probability indicates a high number of trees voted for the class and a low probability indicates a low number of trees voted for the class. Therefore, the probability of an avalanche will provide information to avalanche forecasters on the probability of an avalanche occurring given the current conditions.

The importance of a predictor variable can be determined from the change in error rate when noise is added to the mth variable. The mean change in error rate over the standard deviation of the change in error rate gives the variable importance. A variable with a high value indicates that the variable is important to distinguish between an avalanche and non-avalanche day.

3.5.4   Performance Evaluation

The OOB cases are used to evaluate the performance of the BRF. OOB predictions are run through the ensemble only on trees where the case has been OOB before. The OOB cases are also significantly different for unbalanced datasets and the normal fitness metrics cannot accurately capture the true accuracy of the BRF. The OOB
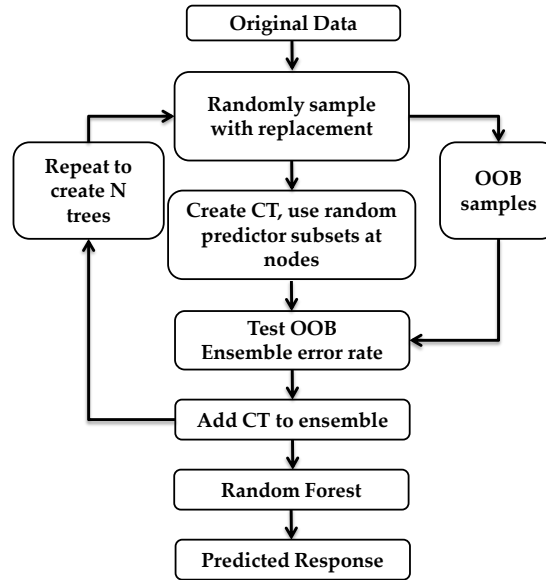
Figure 3.2: Flow chart for balanced random forests. Definitions: CT - Classification tree; OOB - Out-of-Bag

cases are classified as avalanche day or non-avalanche day and a confusion matrix can be created.

Table 3.2: Confusion matrix.

		Observation		
		True	Negative	Total
Predicted	True	a	b	$a+b$
	Negative	c	d	$c+d$
	Total	$a+c$	$b+d$	N

To determine the accuracy, the unweighted average accuracy (UAA) metric will be used as this metric weights evenly the accuracy of predicting an avalanche day and the accuracy of predicting a non-avalanche day. The UAA is calculated

$$\text{UAA} = 0.5 \left(\frac{a}{a+c} + \frac{d}{b+d} \right) \tag{3.1}$$

The creation of the BRF was repeated 100 times to estimate the uncertainty in the both the UAA and the probability of classification.

The true positive rate, or sensitivity, is a measure of how well the predictive model can identify the true class label. The sensitivity is defined as:

$$\text{Sensitivity} = \frac{a}{a + c} \tag{3.2}$$

When the sensitivty approaches 1, the number of false negatives approaches 0, indicating that the majority of true classes are identified correctly. A low sensitivity means a high number of the true class were classified incorrectly (false negatives), indicating a poor predictive model.

The true negative rate, or specificity, is a measure of how well a predictive model can identify the false class label. The specificity is defined as:

$$\text{Specificity} = \frac{d}{b + d} \tag{3.3}$$

When the specificity approaches 1, the number of false positives are minimized, indicating that the majority of the negative classes are identified correctly. A low specificity means a high number of the negative class were incorrectly classified as true (false positives), indicating a poor predictive model. In a two class problem, the specificity of one class is the same as the sensitivity of the other.

3.6   Results

3.6.1   Overall Correct Classification

The average overall correct classification was low for all subsets of predictor variables (Figure 3.3a). The significant variables had the lowest UAA with an overall correct classification only slightly better than a random guess (0.57). The sensitivity (Figure 3.3b) was low with an average value of 0.4, which indicates that the avalanche days were not being correctly identified (a high false negative). The specificity (Figure 3.3c) was within reason at 0.75, which indicates that the non-avalanche days were being correctly identified, and a limited number were classified as an avalanche day.

The second lowest scoring test was using only SNOSS predictor variables with an average UAA of 0.62 (Figure 3.3a). The sensitivity (Figure 3.3b) was higher with an average value of 0.55, which indicates that about half of the avalanche days were not being correctly identified (a high false negative). The specificity (Figure 3.3c) was the lowest of all tests at 0.71, which indicates that a significant number of non-avalanche days were being correctly identified, and a limited number were classified as an avalanche day.

Using all the variables or only meteorological variables produced similar results with an average UAA of 0.66 and 0.67, respectively (Figure 3.3a), with no statistical difference between the two tests. The sensitivity was higher with an average value of 0.55 for both tests, which indicates that about half of the avalanche days were not being correctly identified similar to the SNOSS test. The specificity (Figure 3.3c) were the highest at 0.78 and 0.79 for all and only meteorological variables, respectively. This indicates that these variables were correctly classifying a non-avalanche day

better than the other tests.
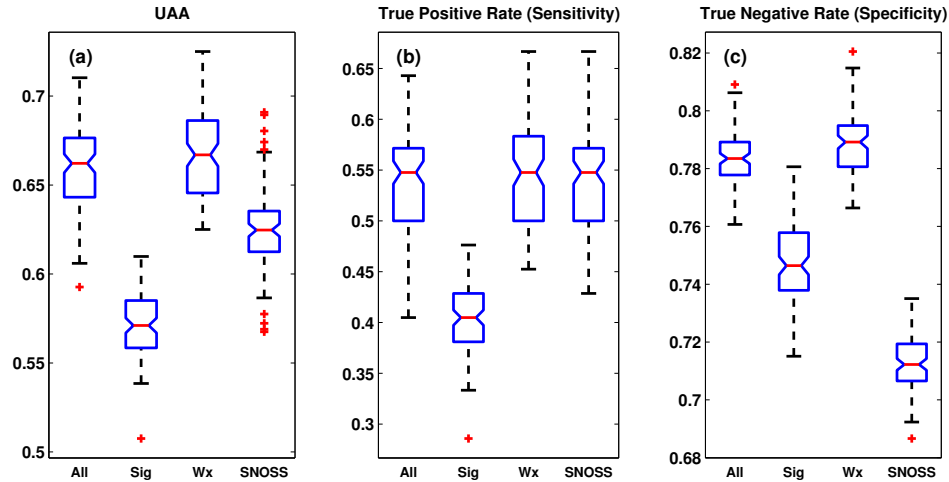
Figure 3.3: (a) UAA, (b) the true positive rate, or sensitivity, and (c) the true negative rate, or specificity.

3.6.2 Variable Importance

The top ten most important variables for each test were evaluated using Figure 3.4. There were four variables that were important for three out of the four tests: PeakTempMax48, SnowDriftMin48, snossSI48, and snossSTRENGTH12. Six variables were important for two out of the three tests: BaseTempMax48, BaseWaterMax24, snossDZ24, snossDZ72, snossSTRENGTH24, and snossSTRENGTH72. Six out of the top ten most frequent variables are attributed to SNOSS model outputs of settlement, strength, and the stability index. Out of the top 20 for all and important variables, 9 were from SNOSS and 11 were from meteorological variables.

The SNOSS variable snossDZ24 showed as the most important variable in two tests, with the BaseTempMax48 and PeakTempMax48 also placing high in the top
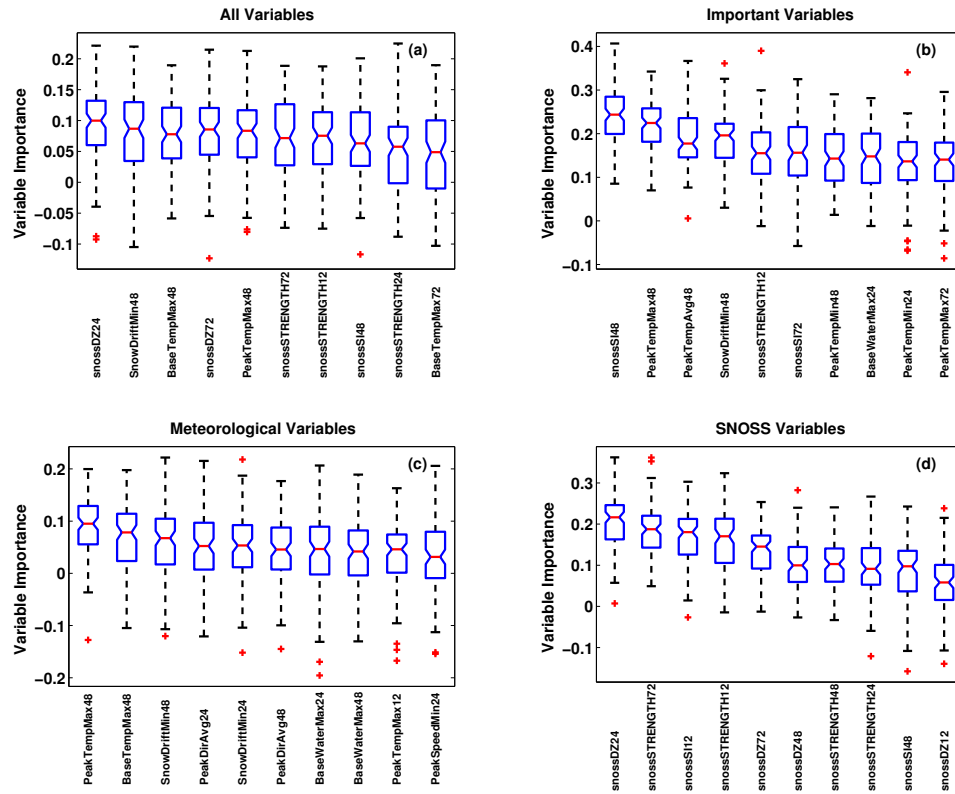
Figure 3.4: The top ten most important variables for the different predictor variable tests. The bar represents one standard deviation about the mean. (a) All variables, (b) important variables, (c) meteorological variables, and (d) SNOSS variables.

ten variables.

3.6.3 Probability of an Avalanche

Figure 3.5 shows the probability distribution function (PDF) for the percent of trees within the BRF voting for an avalanche given the current conditions. Figure 3.5a is the PDF for all the avalanche days. The significant variables have a peak around 0.41 with all other tests between 0.52 to 0.55. Figure 3.5b is the probability of an avalanche for non-avalanche days with the significant variables have a peak
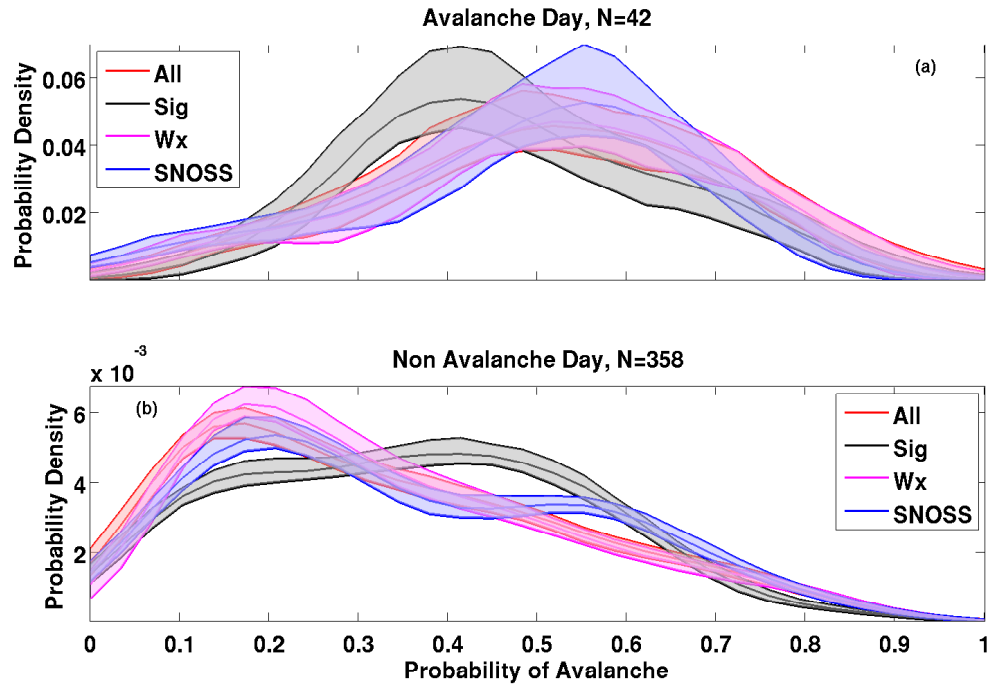
Figure 3.5: The distribution of the probability of an avalanche occurring (a) given the current conditions that produced a natural avalanche and (b) conditions when no avalanches occurred.

around 0.41 with all other tests between 0.17 to 0.21. The non-avalanche day are those days that did not produce an avalanche and should have a lower probability of predicting an avalanche.

3.7   Discussion and Conclusion

A subset of the avalanche records at Alta, UT were used in order to determine when a natural soft slab avalanche will occur during a storm. Previous studies either randomly sampled non-avalanche days from the rest of the weather record (*Hendrikx et al.*, 2005), removed long periods of no new snow (*Davis et al.*, 1999), or use all

the data from the previous seasons (*Cordy et al.*, 2009). These studies attempted to predict all avalanche activity, both natural and artificial. Since we are attempting to predict natural avalanches due to new snow loading, the non-avalanche and avalanche days consisted of large storms with more than 1.3 cm of water. This creates a difficult classification problem to try and predict whether or not an avalanche will occur in a storm.

Balanced random forests (BRF; *Chen et al.*, 2004) is a method of implementing the random forest procedure outlined by *Breiman* (2001). BRF account for an unbalanced dataset and randomly sample the inputs based on the smallest class size, reducing classification bias. BRF benefit when variables are correlated as the random sampling at each stage reduces the affect of correlation between variables (*Breiman*, 1996, 2001). This allows for a large amount of predictor variables from 12, 24, 48, and 72 hours prior to the avalanche day.

Other studies that use classification trees (*Davis et al.*, 1999; *Hendrikx et al.*, 2005) or nearest neighbor techniques (*Purves et al.*, 2003; *Cordy et al.*, 2009) have only used meteorological variables. This is the first study to try and relate the snow pack model SNOSS, along with meteorological variables, to avalanche activity. The average overall correct classification for predicting natural soft slab avalanche activity during a storm was between 57% to 67%. The sensitivity (Figure 3.3b) shows that only about 55% of the avalanche days were being correctly identified. This indicates that there may be other variables that we could not account for, like a persistent weak layer. If persistent weak layers were present, SNOSS would not be able to predict instability and the model would have to rely on the meteorological variables.

The important variables for predicting natural soft slab avalanches were Peak-

TempMax48, SnowDriftMin48, snossSI48, snossSTRENGTH12, BaseTempMax48, BaseWaterMax24, snossDZ24, snossDZ72, snossSTRENGTH24, and snossSTRENGTH72. The snow drift parameter has shown up before in a study performed at Alta, UT (*Davis et al.*, 1999) and in maritime climates (*Hendrikx et al.*, 2005). The other important variables are based on the air temperature and the maximum hourly precipitation rate or intensity (BaseWaterMax24). All important SNOSS variables have a quantitative meaning to the snowpack. The settlement of the failure layer calculated from SNOSS appears to be the most important SNOSS variable in separating avalanche from non-avalanche day with the snow layer strength also an important predictor.

Instead of a "yes" or "no" vote from the BRF, the number of trees within the BRF voting for an avalanche is the probability of an avalanche given the current conditions. The distributions between the two days (Figure 3.5) are quite different as the probability distribution is skewed towards higher probabilities when a natural avalanche has occurred. This shows that the BRF predicts a higher probability of an avalanche when a natural avalanche occurred. The error rates (Figure 3.3a) reflect a cutoff value of 50% of the trees voting for a particular class. It may be that the cutoff value is actually lower since most avalanches are centered around the 52% to 55% range. Error rates may improve by optimizing the cutoff value.

The BRF can be used as a tool by avalanche forecasters to help evaluate the probability of an avalanche given the current meteorological and snowpack conditions. Instead of a "yes" or "no" to an avalanche occurring, we believe that a percent chance will be more useful for avalanche forecasters when the are evaluating avalanche hazard.

Acknowledgements

CHAPTER 4:

SNOW MICRO PENETROMETER SIGNAL CLASSIFICATION WITH RANDOM FORESTS

Summary

The spatial variability of snowpack properties can be fairly difficult to measure given the current method of snow pits. Snow pits are highly subjective to observer skill and can take a significant amount of time to complete. Digging multiple snow pits for spatial variability studies is time intensive and may not be able to accurately capture the true variability. The Snow Micro Penetrometer (SMP) is a tool that can take full mechanical profiles of the snowpack in only a couple of minutes. With the SMP, it is possible to cover large distances while getting useful mechanical snowpack profiles.

This work is the first step in the direction of using the SMP to automatically classify grain types. While on a remote sensing and validation campaign, the SMP can be used to classify the stratigraphy of an area at speeds much greater than the traditional snowpit. The results of this work show that we can classify the SMP signal into new snow, rounds, and facets using an ensemble of classification trees. Future work will include applying this technique to full SMP profiles, which will enable the user to quickly characterize a site.

The paper was published June 2013 in *IEEE Transactions on Geoscience and Remote Sensing* (*Havens et al.*, 2013). This is my first publication during my program

at Boise State University. This paper targets an audience in the snow remote sensing community to show the difficultly in representing a complex snowpack as a single grain type. We hope that our results will show that with different grain sizes, the grain sizes and shapes are significantly different and need to be accounted for in radiative transfer models or in snow water equivalent retrieval algorithms.

Some minor changes were made to the following version to address questions from my committee.

Automatic Grain Type Classification of Snow Micro Penetrometer Signals with Random Forests

Scott Havens[*], Hans-Peter Marshall[*], Christine Pielmeier,[†] and Kelly Elder[‡]

[*]Center for Geophysical Investigation of the Shallow Subsurface, Boise State University, Boise, Idaho, USA

[†]WSL Institute for Snow and Avalanche Research SLF, Davos, Switzerland

[‡]USDA Forest Service, Rocky Mountain Research Station, Fort Collins, CO, USA.

4.1   Abstract

Snow microstructure plays an important role in the remote sensing of snow water equivalent (SWE) for both passive and active microwave radars. The accuracy of microwave SWE retrieval algorithms is sensitive to (usually unknown) changes in microstructure. These algorithms could be improved with high-resolution estimates of microstructural properties by using an advanced instrument such as the Snow Micro Penetrometer (SMP), which measures penetration force at the millimeter scale and is sensitive to microstructure. The SMP can also take full micromechanical measurements at much greater speed, resolution, and without observer bias than a traditional snow pit. Previous studies have shown that the snowpack stratigraphy and grain type can be accurately classified with one SMP measurement using basic statistics and classification trees. For this study, we used basic statistical measures of the penetration force and micromechanical estimates from an SMP inversion algorithm to significantly improve classification accuracy of grain type and layer discrimination. We applied

random forest techniques to classify three snow grain types (new snow, rounds, and facets) from SMP measurements collected in Switzerland and Grand Mesa, Colorado. Random forests performed up to 8% better than single classification trees, with overall misclassification errors between 17-40 percent. The coefficient of variation of the penetration force proved to be the most important variable, followed by variables that contain information about grain size like micro scale strength and the number of ruptures.

4.2 Introduction

The complicated structure of the seasonal snowpack is important for snow avalanches, snow hydrology, and microwave remote sensing. Snow microstructure controls snow strength and complicates retrieval of important hydrological quantities, such as snow water equivalent (SWE) for both passive and active radars (*Rees*, 2006; *Baenninger et al.*, 2008; *Wojcik et al.*, 2008). Microstructural properties such as hardness, grain size, and grain shape vary significantly between layers in the snowpack (e.g., *Pielmeier and Schneebeli*, 2003) and are important to characterize to properly describe the seasonal snowpack (*Shapiro et al.*, 1997).

Accurate and objective methods to determine snow stratigraphy are needed, as stratigraphy is a major influence on microwave emission models (*Durand et al.*, 2008). Current algorithms assume a homogeneous one-layer snowpack, typically with grain size (and sometimes stickiness), as a tunable parameter that is chosen to minimize the error between in-situ ground data and estimates from microwave inversion algorithms (*Yueh et al.*, 2009; *Rott et al.*, 2010). These techniques can produce errors in SWE estimates that range from 70 to 200 percent (*Azar et al.*, 2008).

The current method for determining snowpack properties is manual measurements of snow stratigraphy, which include grain type, density, and hardness. These properties show large variability between snow layers at a single location and over distances on the order of tens of meters (*Sturm et al.*, 2004). Manual snow pit profiles are highly dependent on observer skill. They are time intensive and can introduce uncertainty if the snow pit is mischaracterized. Therefore, an objective method is needed to accurately estimate stratigraphy and grain type for use in the interpretation of microwave emission models and radar backscatter for remote sensing algorithms.

Previous SMP classification studies have applied nearest neighbor methods using only penetration force values (*Satyawali et al.*, 2009). Our preliminary work used single classification trees that included microstructural estimates (*Havens et al.*, 2010) with field experiments that were carried out in a dry seasonal snowpack. Recently, classification tree methods have been improved with ensemble sampling approaches developed by *Breiman* (2001).

The objective of the current study is to use random forests to automatically classify layers of new snow, rounds, and facets in SMP measurements using predictor variables based on SMP estimated microstructure. Random forests are an ensemble of classification trees created using bootstrapping techniques that vote for the most popular class (*Breiman*, 1996, 2001). Random forests have been applied to many classification problems recently, ranging from detection of rock glaciers (*Brenning*, 2009), land cover (*Gislason et al.*, 2006), protein classification (*Jain and Hirst*, 2010), and ecohydrological distribution modeling (*Peters et al.*, 2007).

4.3   Methods

4.3.1   Manual Snow Pit

Manual snow pits were used to classify snow stratigraphy, which includes hardness, density, temperature, grain size, and grain types at high vertical resolution ($\sim$10 mm) in comparison to the horizontal variability of snow properties. Grain types were classified based on the International Classification for Seasonal Snow on the Ground (*Fierz et al.*, 2009), which categorizes snow into nine groups. These nine groups were further simplified into three main groups: new snow, rounds, and facets. New snow (PP) was comprised of precipitation particles and decomposing fragmented particles. Rounds (RG) consisted of small and large rounded grains. Facets (FC) were comprised of faceted grains, including depth hoar. Figure 4.1 shows typical crystals found at Grand Mesa for each of the three main groups.

Dry seasonal snowpacks were observed at all study sites. Melt freeze crusts and wet grains were present at some pit locations but not included in the SMP penetration data due to the limited number of layer samples. Whereas it has been shown that melt freeze crusts and wet grains highly influence radar measurements, they are beyond the scope of this study; however, they will be incorporated in the future.
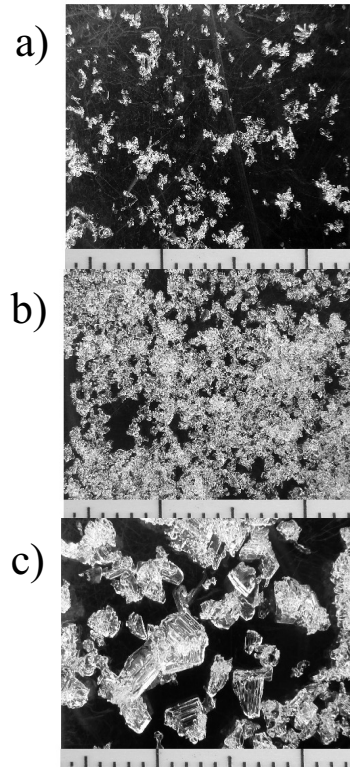
Figure 4.1: Typical crystals found at Grand Mesa for a) precipitation particles, b) rounded grains, and c) large facets. Scale is 1 mm between tick marks.

4.3.2 Snow Micro Penetrometer Measurements

The Snow Micro Penetrometer (*Schneebeli and Johnson*, 1998) measures snow penetration resistance every 4 μm with a 5 mm diameter, 60° cone tip that results in sub-millimeter vertical resolution. There is a larger area of snow influenced due to the "bulb" of snow that develops around the tip as the SMP moves through the snowpack (*LeBaron et al.*, 2014). At this scale, the SMP is primarily measuring the force required to break bonds between snow crystals. From the signal geometry, microstructural and micromechanical properties such as strength, structural element length, and modulus of elasticity can be calculated (*Johnson and Schneebeli*, 1999;

Marshall and Johnson, 2009). For this study, we used the improved inversion procedure described by *Marshall and Johnson* (2009). See *Marshall* (2009) for source code.

Switzerland

The Switzerland database was derived from 93 sites surveyed during 2002-2010 and was used by *Marshall et al.* (in review) to determine how microstructural properties affect snow stability for skier triggered avalanches. Therefore, the manual snow pits tended to be in snowpacks that were targeted for evaluating regional snow stability, and often had a large fraction of faceted snow grains.

Altitudes ranged between 1800 and 2800 m a.s.l. and the slope angles ranged between 24° and 40°. The majority of the measurements were taken on north-facing slopes (NW-N-NE: 60%, SE-S-SW: 22%, E: 7%, W: 11%). This is one of the largest and most comprehensive databases of coincident SMP and stability tests in existence, covering a wide range of conditions, spanning eight years and several different locations in Switzerland. Each of the 890 SMP measurements (taken with multiple SMPs) were qualitatively checked in detail for obvious signal errors and classified into four quality categories (*Lutz*, 2009; *Pielmeier and Marshall*, 2009).

In this analysis we used SMP measurements from 75 of the 93 sites where a slope normal SMP measurement was taken at a manual snow pit.

Grand Mesa, Colorado

SMP measurements were taken over four days during the 3rd NASA Cold Land Processes Experiment (CLPX-III) on Grand Mesa, Colorado during February 2010.

Altitudes ranged from 3200 to 3400 m a.s.l. with relatively flat underlying topography. The objective of the field campaign was to provide ground truth measurements of snowpack properties for both airborne and spaceborne microwave radar measurements. For this campaign, it was more valuable to characterize basic stratigraphy over a large area than to perform detailed stratigraphic profiles at limited locations. Therefore, snow pits were classified using simple grain types (new snow, rounds, and facets) and located in flat open areas.

Four SMP measurements were taken along the backside of the pit face at 20 pits across the study area. After qualitatively checking the SMP measurements, three to four SMP measurements from 19 independent pits were retained for analysis in this study, for a total of 74 SMP measurements.

4.3.3   Database Creation

Table 4.1: Number of layer samples for each grain type by site. Global is a combination of Switzerland and GMM. PP: precipitation particles, RG: rounds, FC: facets.

Site	PP	RG	FC	**Total**
Switzerland	76	131	223	**437**
GMP	15	162	60	**237**
GMM	56	166	65	**287**
Global	132	297	295	**724**

A database of SMP measurements and pit observations were divided into four groups: 1) Switzerland; 2) Grand Mesa using snow pit layer boundaries (GMP); 3)

Grand Mesa with manual delineation of layers in the SMP signal (GMM); and 4) Global (Switzerland and GMM combined). The number of layer samples for each site and grain type is shown in Table 4.1.

For GMP, the SMP force measurements were sampled based on the stratigraphy information from the separate manual snow pit observations. Only layers greater than 100 mm were used. Force samples were buffered on the top and bottom by 15 mm to help remove possible boundary effects that may have been caused by the uncertainty in the location of the stratigraphic boundaries or by a slow transition between two layers. The purpose of this group was to show how manual delineation of layers in the SMP signal are needed during the creation of the database.

The layer boundaries in Switzerland and GMM were manually delineated in each SMP measurement by a trained observer. Layers greater than 20 mm were included since layer boundaries could be visually located with better accuracy in the SMP force signal. Force samples were buffered on the top and bottom depending on the layer thickness.

At Grand Mesa, large discrepancies on the order of 10–20 mm were discovered between GMM and GMP, possibly due to observer error or spatial variability between the pit wall and SMP measurements. Differences in layer boundaries can be seen in Figure 4.2.
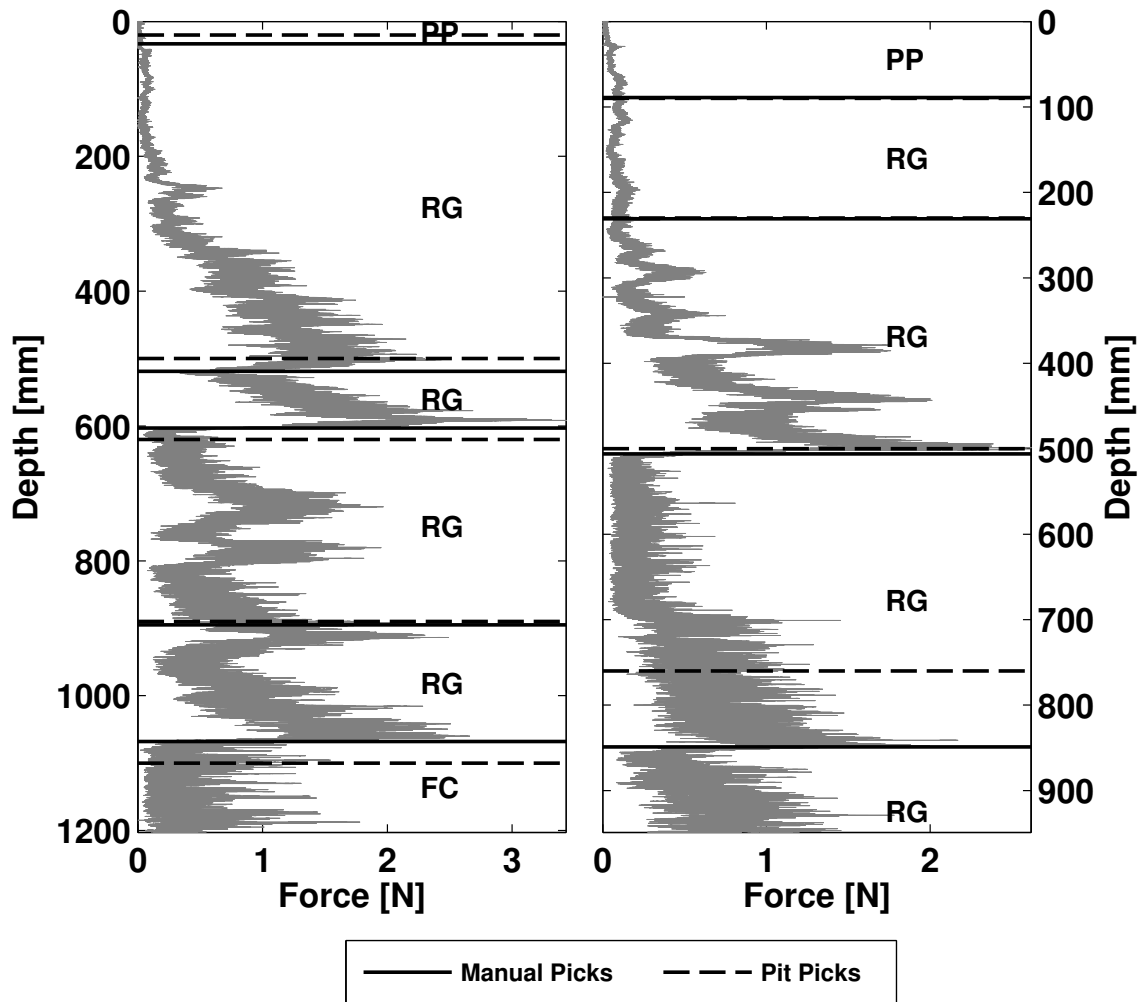
Figure 4.2: Two SMP measurements from Grand Mesa showing how layer boundaries can differ between pit measurements and the SMP signal. Some pit measurements are similar to the manual delineation, however some layer boundaries are up to 20 mm off.

Using the improved analysis procedure described by *Marshall and Johnson* (2009), 13 microstructural and micromechanical properties (Table 4.2) were calculated using a 10 mm window, moving in 1 mm increments for each layer sample. *Marshall and Johnson* (2009) found that a 10 mm window could more accurately reproduce key microstructural values and acts as a filter that smooths outlying values that can

occur during the inversion procedure. The properties in Table 4.2 are estimated from the geometry of the penetration force signal with the rupture force of an individual bond (f), structural element length (L_n), and the deflection of rupture (δ) estimated directly from the signal. All other properties are calculated based on these three variables.

The moving window produces multiple microstructural and micromechanical estimates for each layer where the mean, median, standard deviation, inter-quantile range (IQR), coefficient of variation, and IQR divided by median were calculated for each of the 13 properties, resulting in 78 predictor variables for each layer sample.

Table 4.2: Microstructural and micromechanical values inverted from SMP measurements. See *Johnson and Schneebeli* (1999) and *Marshall and Johnson* (2009) for descriptions and calculations for each variable.

Variable	Description
F	Mean penetration force, normal to SMP tip
L_n	Structural element length
f	Rupture force normal to tip
P_c	Probability of contact (δ/L_n)
P_{c2}	Probability of contact 2 (N_e/N_a)
k	Micro scale stiffness
E_{micro}	Micro scale elastic modulus
σ_{micro}	Micro scale strength
N_T	Number of total ruptures
N_a	Number of available elements
δ	Deflection at rupture
N_e	Number of engaged elements
N_m	Number of measured ruptures per mm

4.4 Classification Analysis

Grain type classification was performed with single classification trees and random forests. The commonly used single classification tree provides a baseline performance for random forests. 90 percent of the layer samples were randomly selected for the learning set (L), ensuring that the test set (the remaining 10%) were comprised of an equal number of layer samples from each grain type to avoid bias. Each sample

comprised of a class label (rounded grains, facets, or new snow) and 78 predictor variables for that layer. 150 Monte Carlo simulations were used to randomly create L for comparing error rates of random forests and single classification trees. The test set placed a value on the uncertainty in the error rate of a future SMP measurement not included in the database.

4.4.1 Classification Trees

From the layer samples in L, a single classification tree was grown and pruned using 10-fold cross-validation. The remaining 10% of the data not in L was applied to the classification tree to get the predicted grain type. The error rate (ER) was calculated using Equation 4.1 (similar to *Satyawali et al.*, 2009).

$$\mathrm{ER} = 1 - \frac{\text{Number of Correctly Classified}}{\text{Total in Original}} \tag{4.1}$$

4.4.2   Random Forests
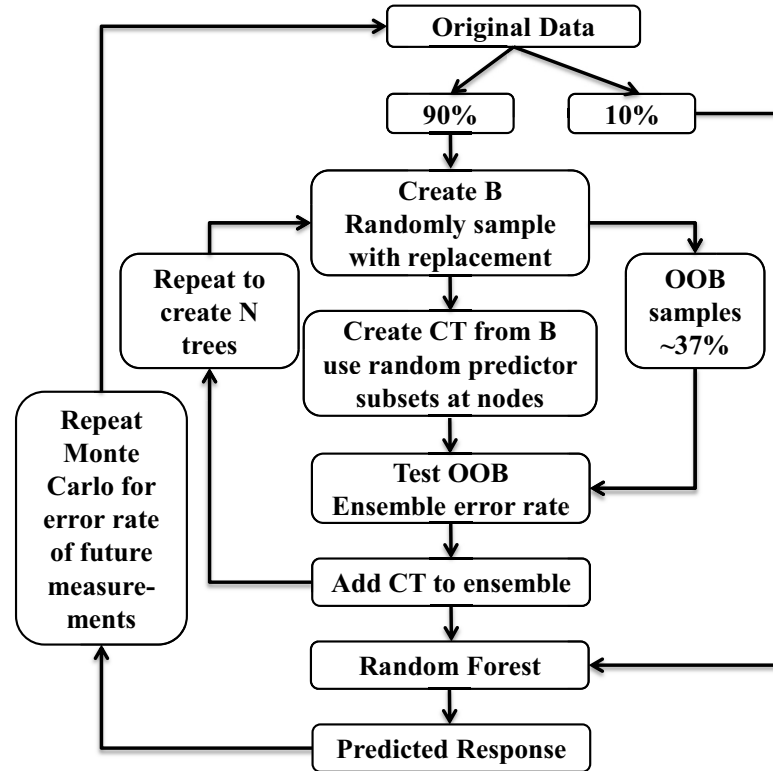
Figure 4.3: Flow chart of the random forest process. Definitions: CT - classification tree; OOB - out-of-bag; B - bootstrap sample. See text for in-depth explanations.

Random forests use random subsets of the original data to build an ensemble of classification trees intended to improve the predictive power and reduce the error rate variance. Figure 4.3 shows a flow chart of the random forest procedure following implementation by *Breiman* (1996, 2001). The layer samples in L were randomly sampled with replacement to create a bootstrap sample learning set (B) the same size as L (*Breiman*, 1996). Class labels found in B may appear multiple times or not at all. On average, 37% of L was left out and was stored as an out-of-bag (OOB) sample. Comparing the OOB error rate to single classification trees was difficult, as

the number of OOB samples and grain classes can vary. Therefore, for this study, the OOB error rate was ignored when comparing random forests with single classification trees, and focuses on the error rates calculated from the test set.

From B, a single classification tree was grown from approximately 250 layer samples from GMM and GMP, 395 samples from Switzerland, and 650 samples from Global. At each node of the classification tree, only a random subset of the predictor variables (the square root of the number of predictor variables) were used to determine the best split, giving rise to the random forest implementation. Randomizing the predictor variables lowers the correlation between trees within the ensemble and adds strength to the predictive power of this technique. The random selection of B was repeated, each time storing the classification tree to create a random forest.

To determine the number of classification trees to construct, the OOB samples were run through the ensemble only on trees where the sample had been OOB previously. This constraint ensured that the error rate was not calculated for samples used in the creation of classification trees. The OOB error rate converges exponentially to a minimum once a certain number of trees were added to the ensemble. Adding more trees to the ensemble will not improve the error rate, but may increase the correlation between trees within the ensemble. Therefore, the number of classification trees included in the random forest was selected where the OOB error rate converged, whereas still limiting the number of trees.

The random selection of B was repeated to create a random forest ensemble. The number of classification trees within the ensemble depends on where the OOB error rate converges. For this study, the random forest was constructed of 75 classification trees grown. The predictor variables from the 10% of the original data not used for

training were applied to the random forest producing a predicted grain type from all 75 trees. The majority vote from the random forest was the predicted grain type.

Predictor variables important for classification were determined by adding noise to the mth variable in each OOB sample. The change in error rate was computed for each OOB sample for all classification trees in the random forest. The measure of importance was calculated as the mean divided by the standard deviation of the change in error rate. The measure of variable importance indicated how well the mth variable distinguishes between grain types.

A major benefit of random forests is when two predictor variables are correlated. Due to the randomness in creating B and the randomness at each classification tree node, each predictor variable is picked with about the same frequency. When noise is added to each variable, the increase in error rate will be similar. Therefore, using correlated variables together will not decrease the error rate (*Breiman*, 2001).

4.4.3 Classification Scenarios

Classification was broken up into two separate scenarios, with the first classifying all three grain types simultaneously. The second scenario classified each grain type in a binary fashion by classifying true or false from a single classification tree or random forest. Each scenario was run using a different number of predictor variables based on the 13 force and microstructural parameters (Table 4.2) to determine the best type of predictors for classification. These runs used the mean, mean and standard deviation, median and IQR, all 78 predictor variables, and the three force statistics used in *Satyawali et al.* (2009). An additional run added the coefficient of variation (CV) of the penetration force (CV(F)) as the mean and standard deviation variables

as the CV(F) has been shown to be a powerful predictor (*Satyawali et al.*, 2009; *Havens et al.*, 2010). The number of variables in each scenario are N=13, N=26, N=26, N=78, N=3, and N=27, respectively.

4.5 Results

4.5.1 Classifying All Grain Types Simultaneously

Table 4.3: Error rates for classifying all grain types simultaneously for random forests and classification trees using the given variables.

Variables	Num Vars.	Switzerland		GMP		GMM		Global	
		RF	CT	RF	CT	RF	CT	RF	CT
All	78	27.8	40.1	40.1	46.9	17.8	22.9	24.9	29.5
Mean	13	33.8	33.9	43.3	49.6	20.6	21.6	28.1	28.6
Mean + Std	26	29.2	35.3	39.9	48.3	16.8	23.3	24.0	28.4
Median + IQR	26	28.3	32.0	44.4	46.8	19.1	27.4	25.3	30.4
Satyawali et al., 2009	3	41.3	38.6	45.1	47.3	21.1	23.6	31.4	30.7
Mean + Std + CV(F)	27	29.2	34.3	39.7	47.3	16.4	22.1	24.5	27.8

Random forests and classification trees were grown for the five different scenarios with the mean results of the Monte Carlo simulations shown in Table 4.3. Depending on the predictors used, the mean error rate for random forest classification was between 27.8–41.3% for Switzerland, 39.7–45.1% for GMP, 16.4–21.1% for GMM, and 24.0–31.4% for Global. Mean error rate for single classification trees were between 32.0–40.1% for Switzerland, 46.8–49.6% for GMP, 21.6–27.4% for GMM, and 27.8–30.7% for Global. However, there was not a single best combination of predictor

variables that produced the lowest error rates for all four sites. In general, the lowest error rates occurred when using the mean, standard deviation, and CV(F) predictor variables, with a 16.4% error rate for GMM, 29.2% error rate for Switzerland, and 24.5% error rate for Global. Note that a random choice of grain type would give an error rate of 67%. Random forests performed better than classification trees for all sites with Switzerland having the smallest margin (Figure 4.4).
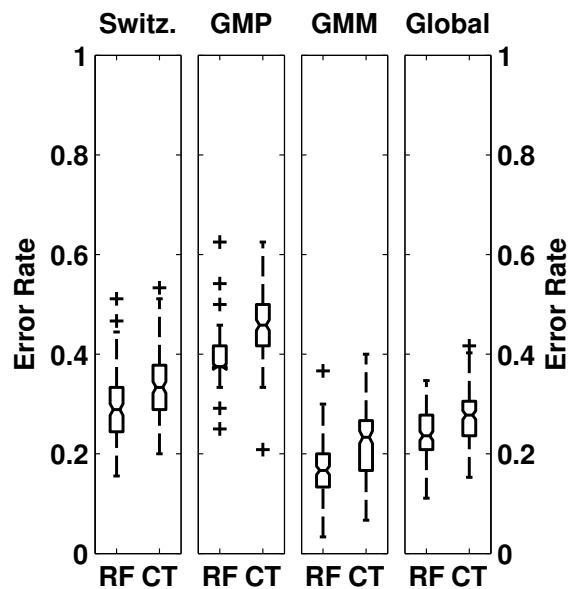
Figure 4.4: Monte Carlo results using the mean, standard deviation, and CV(F) predictors for random forests (RF) and a single classification tree (CT). The results between RF and CT are statistically different with lower error rates for RF at all sites.

Predictor variables used by *Satyawali et al.* (2009) lead to the highest error rates in this study. By using information about the distribution or microstructure and hardness, classification performance was improved by 12% for Switzerland, 7% for Global, and 5.5% for GMM.

The variable importance for the mean, standard deviation, and CV(F) predictor

variables are shown in Figure 4.5, and a commonality was seen between all sites. The most important variable was CV(F), which was similar to findings by *Satyawali et al.* (2009) and *Havens et al.* (2010). The standard deviation of the penetration force was the most important variable for Global and was in close second for GMM. The mean and standard deviation of the rupture force were important for Switzerland. The mean and standard deviation of σ_{micro} are key variables for both GMM and Switzerland. Seven out of the top 10 predictor variables contain information about the grain size (i.e., N_T, σ_{micro}, N_m, and L_n), showing that changes in grain size was an important distinguishing factor.

The results from GMM and GMP show a significant difference in classification accuracy (GMP: 39.7%, GMM: 16.4%). Three of the most important variables, the standard deviation of F and the mean and standard deviation of σ_{micro} (Figure 4.5), show major differences.
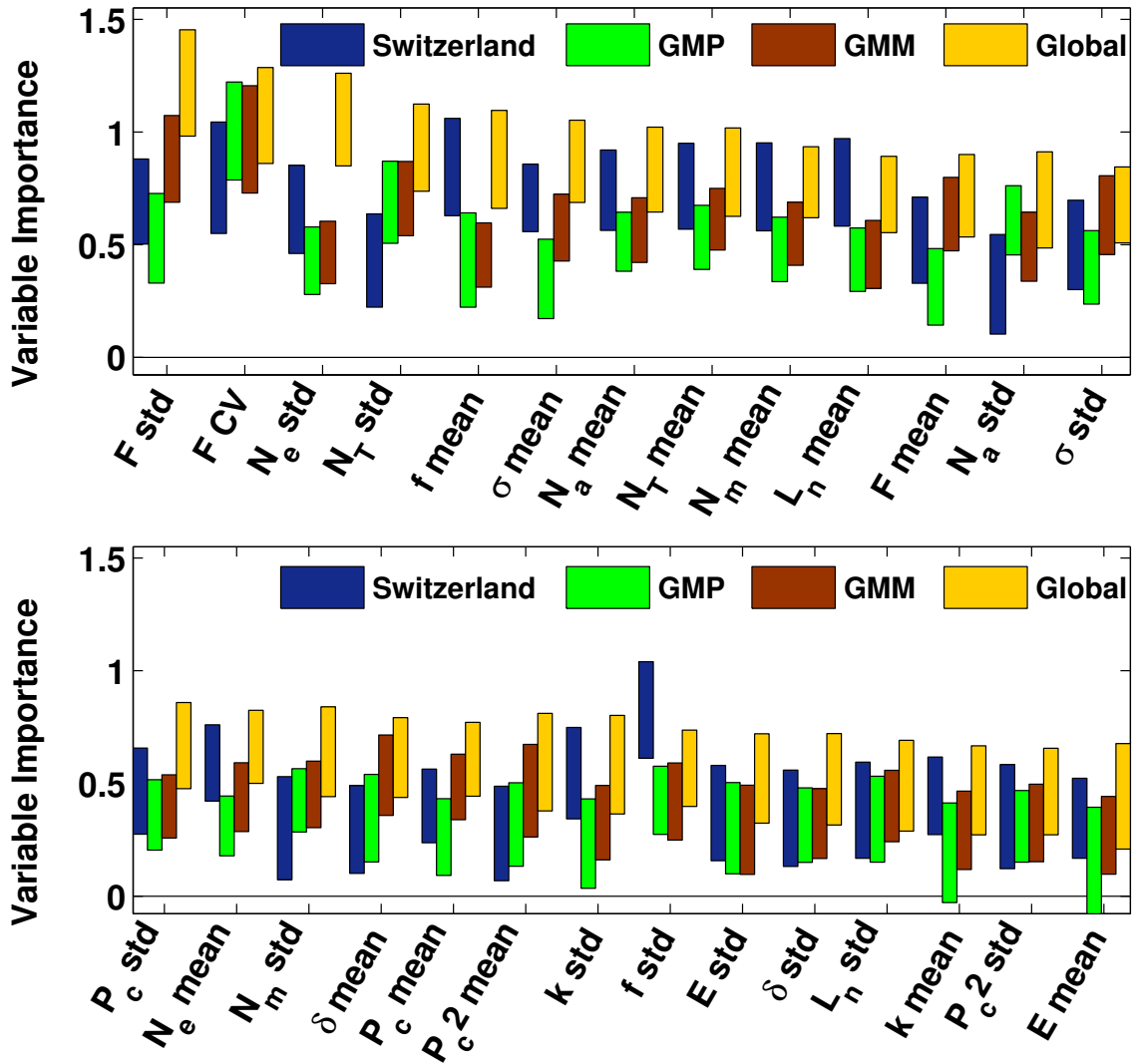
Figure 4.5: Variable importance for simultaneously classifying three grain types with mean, standard deviation, and CV(F) predictor variables. The bars show two standard deviations about the mean over the Monte Carlo simulations. Negative values occur when there is a decrease in the error rate after adding noise to the mth variable. Organized by highest to lowest Global importance.

4.5.2   Binary Classification

Table 4.4: Binary random forest error rates for each grain type, using the mean, standard deviation, and CV(F) predictor variables. The mean is an average of the three individual error rates.

Site	PP	RG	FC	Mean
Switzerland	21.2	28.2	21.8	**23.7**
GMP	50.0	18.7	13.3	**27.3**
GMM	12.2	15.0	15.1	**14.1**
Global	19.3	21.7	19.8	**20.2**

Binary classification showed similar results to simultaneous classification for the five different scenarios with the lowest error rates for mean, standard deviation, and CV(F) (Table 4.4). Classifying in a true or false manner shows noticeable improvement of 2–12% in the mean classification accuracy over each of the sites as compared to simultaneous classification.

In binary classification, a random guess will result in a misclassification of 50%, with almost all grain types falling well below these values. Precipitation particles had the highest misclassification for sites without manually delineated layer boundaries (GMP) due to a small sample of new snow. However, we see that even with a random guess, the overall mean misclassification was still significantly lower than simultaneous classification.

Figure 4.6 shows the important variables broken down by site and grain type for the mean, standard deviation, and CV(F) predictor variables. Similar important variables with simultaneous classification are seen with the CV(F) as the most important

variable for distinguishing between facets and rounds at all sites. The standard deviation of F was an important variable for classifying precipitation particles at GMM and Global. The next important variables vary between sites but were very similar to the simultaneous classification with 7 out of the 10 top variables containing information about grain size.
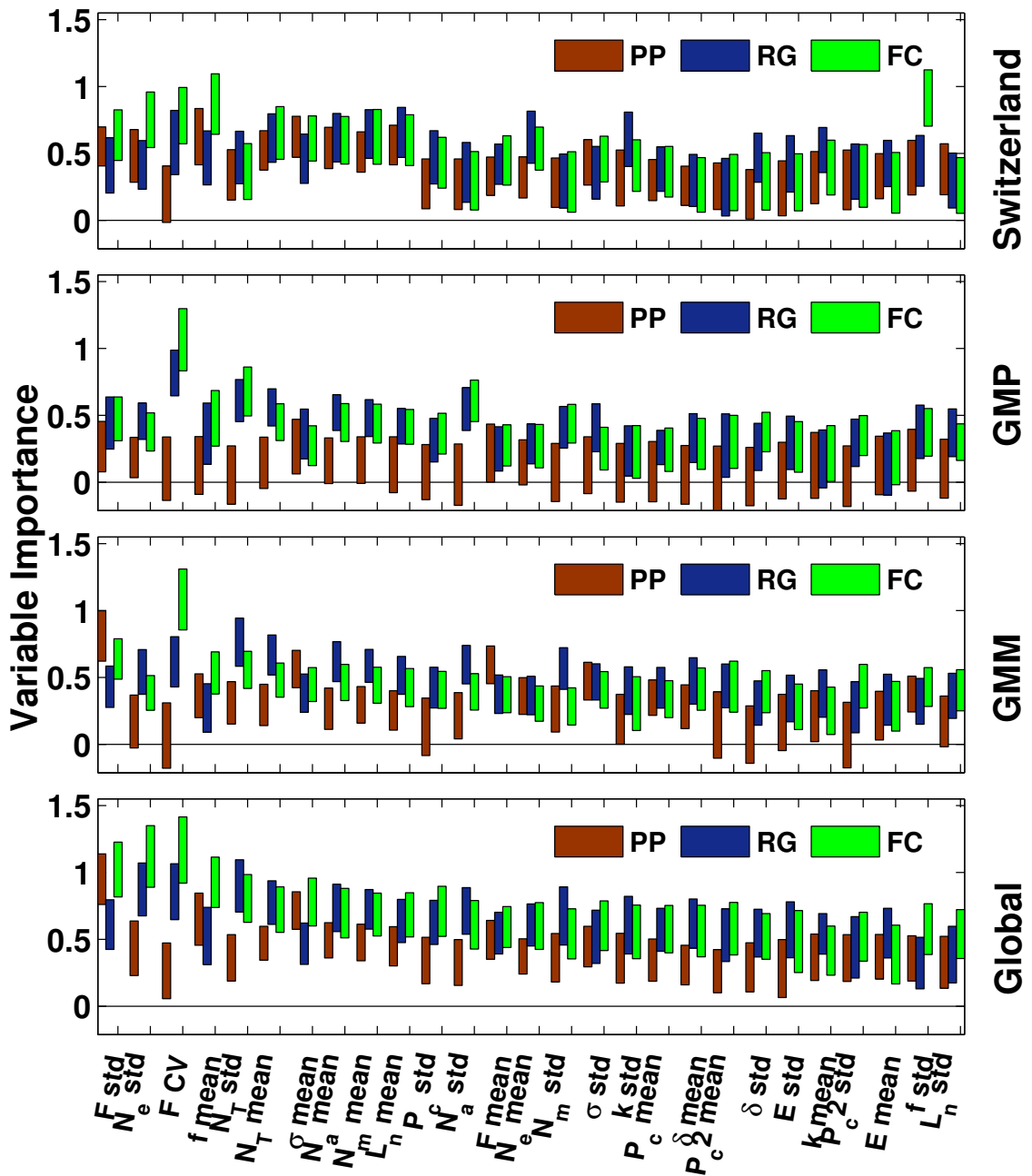
Figure 4.6: Variable importance for binary classification of three grain types, using the mean, standard deviation, and CV(F) predictor variables. The bars show two standard deviations about the mean over the Monte Carlo simulations. Organized by highest to lowest mean Global importance.

4.6 Discussion

4.6.1 Random Forests for Classification

For the first time, random forests have been applied for automatic grain type classification using SMP estimated microstructural estimates. Information about the distribution of microstructural properties within a layer significantly lowered the error rates as compared to single classification trees using only penetration force statistics.

The majority of the most important variables (i.e., N_T, σ_{micro}, L_n) contain information on the grain size or the distribution of grain size within the layer. The results suggest that knowledge of the grain type can provide insight into the grain size distribution within that layer and how the distribution varies between layers. The grain size distribution is a significant factor in interpreting remote sensing data.

Outside of the top variables, most of the 27 predictor variables carry a similar amount of predictive power. However, without these variables, the error rate increases. Therefore, including information about the microstructure distribution greatly improves classification performance in random forests even if the variables are not of great predictive power individually.

Time scales in this study vary from one week (Grand Mesa) to eight years (Switzerland). The large time scales for Switzerland may account for the higher error rate. However, Switzerland still has a relatively low mean error rate of $29.2 \pm 6.6\%$. This indicates that random forests are ideal for Switzerland where the data spans multiple years, multiple locations, and uses multiple SMPs since the uncertainty due to these factors are incorporated randomly into the ensemble.

Global was the largest database in our study with the least amount of bias between

rounds and facets. Having more balanced layer samples for the learning set makes outliers less likely to affect classification and decreasing the overall misclassification error. Switzerland and GMM share common important variables and combining these two databases strengthens the classifier. Global shows that the fundamental differences between grain types were similar on two separate continents and from season to season. Therefore, local SMP calibration may not be necessary anymore if enough SMP profiles can be obtained to create a single global classification scheme.

The next step will be to classify a full SMP measurement. Previous studies have shown that full measurement classification can be difficult and expert rules were introduced to constrain the classification (*Bellaire et al.*, 2009; *Havens et al.*, 2010; *Satyawali et al.*, 2009).

4.6.2   Manual Layers

There are two possible explanations for the significant differences in classification error between GMM and GMP. Although GMM has 50 more layer samples than GMP, this is not a significant increase in percentage of total samples and cannot be the major factor in cutting the misclassification error in half. Another likely cause for the large difference in error was due to the methods of the manual snow pit profile and SMP sampling. *Pielmeier and Schneebeli* (2003) showed that snow pits could only account for 76% and 82% of layers and layer boundaries respectively, whereas the SMP could detect all layers and layer boundaries when compared with detailed microstructural measurements from surface sections. The results show the inherent uncertainty in manual snow pit profiles for classifying layer boundaries.

The SMP can more accurately capture layer boundaries requiring manual delin-

eation of layers for direct comparison with snow pits. This process will minimize the uncertainty due to errors in the snow pit and true variability between the location of the pit wall and the SMP measurement. A snow pit layer boundary that is off by only 10 mm (the average thickness of a human finger and the typical resolution of a snow pit profile) contains 2,500 SMP force samples. When falsely associated with an adjacent layer, the number of samples can significantly alter the underlying property distribution for the microstructural and micromechanical properties for each layer, especially for thin layers. This will affect the performance of classification schemes.

4.6.3   Remote Sensing Application

The majority of ground-based microwave radar reflections can be associated with layer boundaries seen in the SMP measurement (*Marshall et al.*, 2007). These layer boundaries occur at changes in grain type, which can be associated with a change in grain size. Determining the grain types (and stratigraphy) of a full SMP measurement will help with the interpretation and location of major radar reflections and overall radar backscatter.

Applying grain type classification to SMP measurements in combination with ground-based radar may provide a method for quickly quantifying snow stratigraphy accurately over large areas. Radar reflections can be associated with layer boundaries determined by the SMP, then tracked throughout the radar profile to determine the spatial variability of the grain types. Determining the spatial distribution would benefit remote sensing campaigns, avalanche studies, and would also provide much needed data for improving and validating multi-layer snowpack models.

4.7   Conclusion

The Snow Micro Penetrometer is a unique instrument that quickly determines snowpack properties at a high vertical resolution, as compared to the time intensive manual snow pit profiles. Random forests have been shown to be a robust classifier in determining three major grain type classes automatically, with error rates ranging from 16.4% to 29.2%. However, time intensive SMP layer picking was needed to obtain the most accurate results.

SMP measurements have been shown to be sensitive to snowpack stability, and recent studies have shown that microstructural estimates from the SMP can be used to accurately classify the stability of several different stability tests (*Bellaire et al.*, 2009; *Bellaire and Schweizer*, 2011; *Pielmeier and Marshall*, 2009; *Marshall et al.*, in review). Nonetheless, a manual delineation in the SMP measurement of the weak layer was required. In contrast, *Lutz* (2009) employed the derivative of a moving window to find significant changes in the coefficient of variation, indicating the weak layer boundary. Differences in layer properties are important for snowpack instability, possibly more than the absolute property value. This classification of grain type will be used in future work to help guide an automatic estimate of the weak layer location and to classify the character of the stability release.

Coincident SMP and ground based active microwave radar measurements will become an important tool in the future for the interpretation of airborne and spaceborne microwave radar validation and calibration campaigns. Together, these two tools can be used to map the distribution of new snow, rounded, and faceted grains over large distances. Understanding how SMP estimated microstructure and stratigraphy affects microwave radar will significantly improve remote sensing SWE retrieval

algorithms.

Acknowledgment

CHAPTER 5:

AVALANCHE DETECTION WITH INFRASOUND

5.1   Introduction

There are two types of avalanches, dry and wet. A dry avalanche occurs when the snowpack is below freezing temperature and there is minimal free water within the snow. Dry avalanches typically move faster than wet avalanches, at speeds of 30-50 m/s (Section 6), and generate a powder cloud. Wet snow avalanches typically occur due to a decrease in strength of the snowpack due to warming and free water within the snow. Since there typically is an excess of liquid water, a wet snow avalanche moves slower (5-30 m/s) and does not develop a powder cloud. Wet snow avalanche infrasound generation is not well understood or characterized, and typically signal amplitudes are much lower. Therefore, I will concentrate on the infrasound generation from dry snow avalanches for this review, which is currently better understood. Wet avalanches do produce infrasound but not in a similar manner as dry avalanches (see example in Section 5.4.2).

A dry avalanche typically is made up of three layers (Figure 5.1). The dense flow portion of the avalanche flows over the snowpack, entraining snow. The movement over the snowpack generates seismic signals that can be detected and are a function of the avalanche path characteristics (see Appendix B for review of avalanche generated seismic signals). The shear stress caused by interaction with the air against the dense

flow leads to a saltation layer that moves faster than the dense flow. If avalanche speeds are great enough, turbulent eddies form to create a powder cloud or suspension layer that covers the avalanche core (*McClung and Schaerer*, 2006).
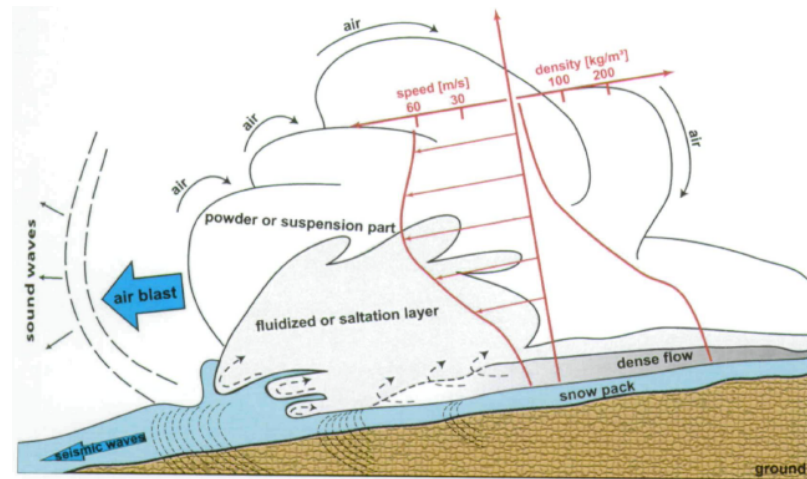
Figure 5.1: Dry avalanche flow, showing the three layers and possible sources of both infrasound and seismic signals. From *Kogelnig et al.* (2011).

Infrasound (1-20 Hz) is generated from the turbulent flow from the suspension layer of the avalanche, which is moving at a higher speed than the dense flow and saltation layers (*Kogelnig et al.*, 2011). The suspension layer typically forms in the upper part of the avalanche path and looses energy as the avalanche slows down (*Comey and Mendenhall*, 2004; *Kogelnig et al.*, 2011). *Kogelnig et al.* (2011) concluded that the size of the suspension layer observed on pressure pylons and the avalanche velocity were proportional to the infrasound amplitude.

Even though the entire avalanche core is covered by the powder cloud, the theory is that only a small portion of the avalanche creates the measurable infrasound signals. Infrasound signals are generated when the avalanche displaces a large amount of the atmosphere. The most violent part of a dry avalanche is the front and where you can

typically see large, forceful vertical eruptions of the powder cloud. These eruptions should coincide with large spikes in the infrasound amplitude. Between eruptions, the turbulent eddies at the avalanche front generate less intense infrasound signals. However, no one has been able to verify these theories with quantitative data yet.

5.1.1 Current Avalanche Infrasound Research

The first avalanche infrasound research was performed at the National Oceanic and Atmospheric Administration (NOAA) in Boulder, CO. The authors (*Bedard Jr.*, 1989, 1994; *Bedard Jr. et al.*, 1988) found that avalanches generate acoustic signals in the 1-5 Hz region. They could detect avalanche signals on their atmosphere infrasound sensors deployed for atmospheric studies.

In Europe, *Chritin et al.* (1996) developed an avalanche detection system using infrasound sensors. Their system was called ARFANG and was used to detect avalanches using an array of four sensors to update a database of avalanche occurrences. With the accurate timing of the avalanche known from the infrasound, a nearest-neighbor avalanche forecasting model could be updated to more accurately evaluate the current avalanche hazard. The ARFANG system is still operational but has not been updated since it was first implemented.

In the United States, using infrasound for avalanche detection was first developed at Teton Pass, WY and Jackson Hole Mountain Resort, WY using a single infrasound sensor. Several winters of data were collected to create a catalogue of avalanche signals (*Scott and Lance*, 2002). The avalanche detection algorithm for the one sensor was based off the catalogue of events, statistics, digital filtering, and weighted threshold decision-making to determine if a signal was a potential avalanche. The results are

mixed as wind noise can interfere with signal detection and classification (*Scott et al.*, 2004). The next step was to use multiple sensors to detect coherent signals (*Comey and Mendenhall*, 2004; *Scott et al.*, 2007). An array of sensors was placed in a line 150 meters wide. With this array, the authors could beamform where the signal was generated. Since it's a commercial detection system, the actual processing steps are not well known nor published but most likely use correlation to determine the travel time differences between sensors.

Currently, the system developed by *Scott et al.* (2007) is applied operationally at Teton Pass, WY and Alta, UT. Multiple arrays of six sensors in a circle are used to identify coherent avalanche signals. The data is processed near real time using Matlab functions and displayed with a GUI. This commercial system is the most popular in the United States but lacks many array processing techniques that could more accurately detect and locate avalanches, and is of very high cost (close to $1M for recent Alta, UT system).

Recently, work by *Ulivieri et al.* (2011) in the Aosta Valley, Italy has brought modern array processing techniques to avalanche detection. *Ulivieri et al.* deployed a 4 sensor array and detected all events using multi-channel correlation method (*Cansi*, 1995).

5.2   Study Site

The Idaho Transportation Department (ITD) forecasts for Highway 21, located 2.5 hours (170 kilometers) northeast of Boise, Idaho in an intermountain climate. The area typically sees moderate snowfall (300 inches average), often extremely cold temperatures between storms (-30 to -15 C), and rain on snow events throughout the

winter. ITD has a limited explosive avalanche mitigation program due to the complex terrain of the start zones and highway location. Avalanche activity is mainly direct action avalanches due to storm snow or rain on snow, with at least one major wet slide cycle during the spring. Both lanes of Highway 21 are frequently covered during avalanche cycles and the road is often closed for several days at a time. The average return frequency for avalanches reaching the highway in relation to the infrasound arrays are shown in Figure 5.2.
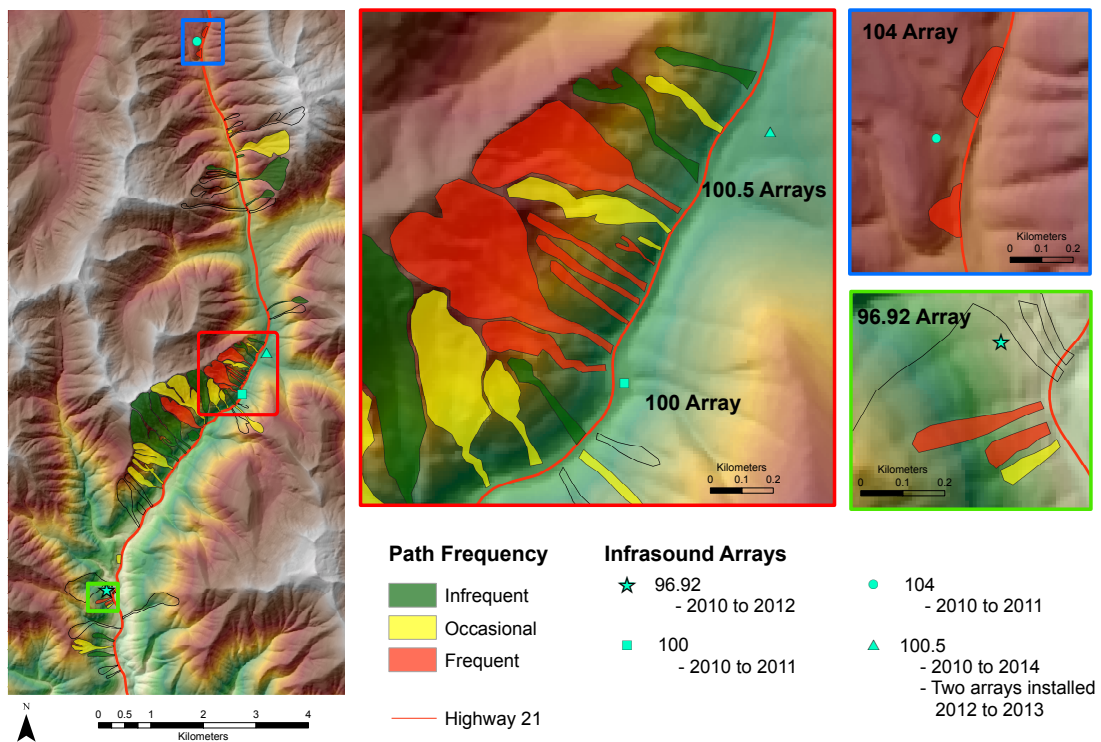
Figure 5.2: Overview of infrasound array installations in relation to the avalanche paths. The avalanche path colors indicate return frequency of avalanches that reach Highway 21 with frequent avalanches (red, ≥ 2 per year), occasional avalanches (yellow, 1-2 per year), and infrequent avalanches (green, ≤ 1 per year).

Leveraging a previous project with ITD to forecast direct action avalanches using snow stability modeling (Chapter 2), I deployed infrasound arrays to determine accu-

rate avalanche timing for model improvement. The infrasound arrays have been active along Highway 21 since the winter of 2010/2011 with the number of arrays ranging from a maximum of four to one arrays located near the most frequent avalanche paths. The following table summarizes the array types installed.

Table 5.1: Summary of the infrasound array installations along Highway 21.

Winter	Number of Arrays	Number of sensors	Configuration
2010/2011	4	3	Arranged in a triangle with 30 meter spacing
2011/2012	2	3	Arranged in a triangle with 30 meter spacing
2012/2013	2	7	Spoke with 15 and 30 meter spacing, one geophone
2013/2014	1	5	Square with one in middle, one geophone, real time prototype

5.3   Background

Processing the raw infrasound data and outputting an event classification requires multiple steps. The following outlines the steps required to produce an event classification:

1. Take the raw infrasound data and use array processing techniques to calculate a coherency metric that indicates if a signal is present.

2. Use non-parametric event detection to determine if a signal is present from the previously calculated coherency metric.

3. If an event is detected, pass the relevant data to the classification scheme to

80

determine the type of event.

5.3.1 Array Processing

Arrays are a grouping of multiple instruments within a small area that decrease the signal-to-noise (SNR) ratio from summation of the signal using all sensors. An advantage of arrays is the ability to determine the source direction for location information (*Rost and Thomas*, 2002). For example, the use of arrays in the seismological community has helped to refine velocity models of the Earth's interior (e.g., *Karason and van der Hilst*, 2001) and improve the detection capability of underground nuclear explosions (*Douglas*, 2002). Arrays have also been used with infrasound to detect avalanches (*Scott et al.*, 2007; *Ulivieri et al.*, 2011), study eruptions from volcanoes (*Johnson*, 2004), and determine the location of thunder (*Arechiga et al.*, 2011).

Many array processing techniques have been developed by the seismic community to interpret array seismic data and can be adapted for use with infrasound. *Rost and Thomas* (2002) provide an excellent overview of many of these methods listed below.

Array processing techniques assume a plane wave crossing the array. This is a good assumption for a large source-receiver distance. The two concepts for the foundation of array processing are the slowness vector and beam forming.

Slowness Vector

A wave front can be described by two parameters: (1) the incidence angle i and (2) the back azimuth θ (Figure 5.3). The incidence angle is related to the inverse of the apparent velocity (v_{app}) of the wave across the array and has units that are the

inverse of velocity (s/m). The slowness s is defined as:

$$s = \frac{1}{v_{app}} = \frac{\sin i}{v_0} \tag{5.1}$$

where v_0 is the speed of sound through air.

a) Vertical plane
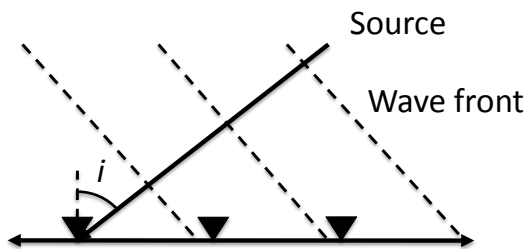
b) Horizontal plane
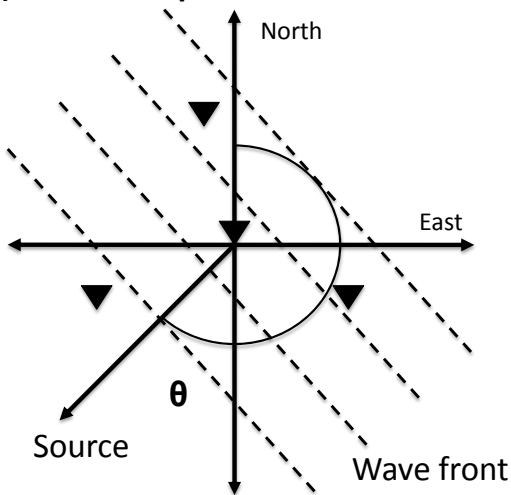
Figure 5.3: a) The incidence angle i is the angle from vertical at which the wave front reaches the array. b) The bearing from North to the source is the back azimuth θ. Triangles are example sensor locations.

The back azimuth (θ) is the direction in degrees from North that the wave front passes the array in the horizontal plane (Figure 5.3). Both incidence angle and back

azimuth are combined to determine the slowness vector $\mathbf{s}$, which points in the direction of wave propagation (Figure 5.4). The slowness vector $\mathbf{s}$ is related to the incidence angle and back azimuth by:

$$
\begin{aligned}
\mathbf{s} &= (s_x, s_y, s_z) \\
&= \left(\frac{\sin\theta}{v_{app}}, \frac{\cos\theta}{v_{app}}, \frac{1}{v_{app}\tan i} \right) \\
&= s_{hor} \left(\sin\theta, \cos\theta, \frac{1}{\tan i} \right) \\
&= \frac{1}{v_0} \left(\sin i \sin\theta, \sin i \cos\theta, \cos i \right)
\end{aligned}
\tag{5.2}
$$
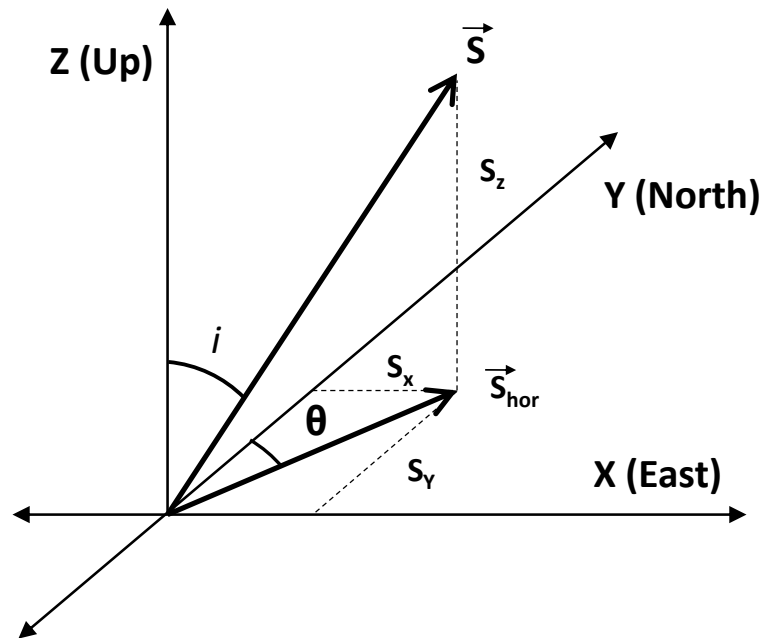
Figure 5.4: Slowness vector $\mathbf{s}$ broken down to it's components s_x, s_y, and s_z. s_{hor} is the slowness vector in the $x - y$ plane.

Beam Forming

Beam forming allows for separation of coherent signals and noise by utilizing all sensors in the array. When a wave crosses the array, the sensors record the signal with a time shift based on the wave's slowness vector. By applying the correct slowness vector to the recorded data, and shifting each sensor in time, the coherent signal can be aligned on all sensors, and the SNR can be increased.

Each sensor in the array has a direction vector $\mathbf{r}_j$ from the array center and represents the sensor's position in the array. The absolute value $r = |\mathbf{r}_j|$ describes the sensors absolute distance from the array center. The travel time of the wave between sensors is dependent on the slowness vector and sensor's direction vector. Given a recorded signal $f(t)$ with noise $n(t)$, the signal recorded at each station j is:

$$x_j(t) = f(t - \mathbf{r}_j \cdot \mathbf{s}_{hor}) + n_j(t) \tag{5.3}$$

To calculate the signal with the time shift removed given the sensor's location $\mathbf{r}_j$ and the horizontal slowness vector $\mathbf{s}_{hor}$:

$$\bar{x}_j(t) = x_j(t + \mathbf{r}_j \cdot \mathbf{s}_{hor}) = f(t) + n_j(t + \mathbf{r}_j \cdot \mathbf{s}_{hor}) \tag{5.4}$$

Summing the signals over all M sensors produces the beam trace $b(t)$ and increases the signal to noise by approximately $\sqrt{M}$.

$$b(t) = \frac{1}{M} \sum_{j=1}^{M} \bar{x}_j(t) = f(t) + \frac{1}{M} \sum_{j=1}^{M} n_j(t + \mathbf{r}_j \cdot \mathbf{s}_{hor}) \tag{5.5}$$

Fisher Statistic

The Fisher statistic was first suggested by *Melton and Bailey* (1957) as a method to detect events across a seismic array with others (e.g, *Smart and Flinn*, 1971; *Blandford*, 1974) further developing the theory. *Blandford* (1974) states the assumptions for the Fisher statistic as:

1. Signals must be perfectly correlated across the array

2. Noise is normally distributed, stationary, and uncorrelated across the array

These assumptions are usually violated for small aperture infrasound and seismic arrays where the signals may not be perfectly correlated and the noise may also be correlated.

Following *Blandford* (1974) and *Arrowsmith et al.* (2008), the Fisher statistic in the time domain is defined as the power of the beam over the residual power:

$$F = \left(\frac{M-1}{M} \right) \times \frac{\sum_{n=1}^{N} \left[\sum_{j=1}^{M} x_j(n+l_j) \right]^2}{\sum_{n=1}^{N} \left[\sum_{j=1}^{M} \left\{ x_j(n+l_j) - \left(\frac{1}{M} \cdot \sum_{m=1}^{M} x_m(n+l_m) \right) \right\}^2 \right]} \quad (5.6)$$

where M is the number of array elements, N is the size of the processing window in samples, l_j is the time lag in samples applied to the signal for a given element, and x_j is the signal measured at each element. When a signal is present, the numerator will increase from the power of the beam and the denominator will be reduced to the residual noise.

The Fisher statistic was calculated for a processing window size of 6 seconds, overlapped by 3 seconds. These values were chosen based on the real time detection computational times in order to have an efficient detection system. Having a smaller

window size, for example 4 seconds with 2 second overlap, will increase the number of computations of a 10 minute signal by 50%. On the other hand, having the window size too large may miss important smaller events. We have decided on a compromise of a 6 second processing window to balance computational time, location accuracy, and the ability to track a moving source. Moving avalanches are usually longer than 30 seconds and can be accurately characterized with the 6 second window.

Frequency Wave-Number Analysis

The frequency wave-number (fk) analysis (*Rost and Thomas*, 2002) allows for the simultaneous calculation of the incidence angle and back azimuth. The fk analysis determines the time shifts required for varying slowness vectors and calculates the Fisher statistic. When the Fisher statistic is maximized, the slowness vector provides a direct estimate of the back azimuth and incidence angle. If the source location is unknown, a grid search is performed over a range of back azimuths and incidence angles.

The fk analysis is performed for a short moving window with a constant step size. Within each window, the Fisher statistic is calculated using a grid search to time shift the infrasound signal depending on the slowness vector at each grid node. To provide the best results, the window size must be large enough to capture the dominant frequency moving across the array. For the small aperture arrays on Highway 21, a 6 second window with 3 second step size has proved to be sufficient to determine the location of moving sources.

5.3.2 Non-parametric Event Detection

Non-parametric Methods

The Fisher statistic follows the Central F-distribution (*Blandford*, 1974) when the data meets the assumption criteria of a perfectly correlated signal and uncorrelated noise. However, the assumptions are violated due to correlated noise recorded across the array, which may be due to the small aperture arrays used (30-50 meters). There are two methods to handle this situation: 1) assume that the data can fit the F-distribution to use parametric methods or 2) estimate the distribution directly from the data with non-parametric methods.

The Central F-distribution has two parameters that determine the shape, based on the signal bandwidth, time length of processing window, and the number of elements in the array. Using a moving window of Fisher statistic values, *Arrowsmith et al.* (2008) fit the window of values to the F-distribution by scaling the values so that the peaks in the distribution lined up. This method will work well with larger aperture arrays ($\sim$1-2 km in the study) but will have great difficulty if the Fisher statistic values do not follow the F-distribution.

Non-parametric methods allow for the Fisher statistic values within the window to be used directly to estimate the distribution. No assumptions are made about the underlying distribution making the method more robust, especially when values do not necessarily follow the Central F-distribution. The non-parametric probability density function (PDF) of Fisher statistic values is estimated using kernel density estimation (*Martinez and Martinez*, 2008). The probability of an observed value x_t

at time t is

$$P(x_t) = \frac{1}{N} \sum_{i=1}^{N} K_\sigma(x_t - x_i) \tag{5.7}$$

where K_σ is a Gaussian kernel function with bandwidth σ, N is the number of background samples, and x_i is the background Fisher statistic values. Other kernel functions can be used, but the results are typically not very sensitive to the kernel and primarily depend on the choice of kernel bandwidth.

Background Model

Signal noise will create a Fisher statistic that falls into a certain type of distribution. The distribution can be modeled by creating a non-parametric PDF for a moving window of Fisher statistic values (similar to *Arrowsmith et al.*, 2008). This becomes the background model for noise with which to compare new values (Figure 5.5). The Fisher statistic value from noise will fall somewhere within the distribution and have a higher probability (Equation 5.7). An event will fall to the right of the distribution and have a low probability that the value has been observed before. A given value is considered an event if the $P(x_t) <$ threshold.

A moving background model will adapt to changes in the Fisher statistic from correlated noise. As the background window moves forward in time, the model is updated by removing the oldest sample and adding the newest sample to the model. This type of update adds all samples to the model and will include samples that are not part of the background model. However, this will lead to false negatives as an event may not be detected if a significant amount of events are already within the model. The effect can be reduced by increasing the window size but this will also increase the number of false positives as adaptation to changes will be slower.
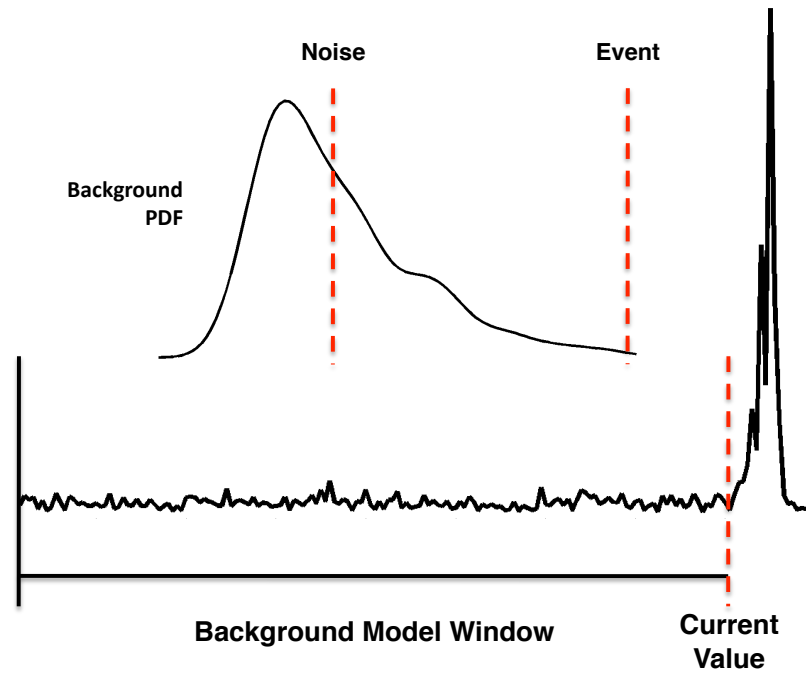
Figure 5.5: A window of Fisher statistic values creates the background model PDF. A new value of the Fisher statistic is then compared to the PDF with noise expected to fall within the distribution and an event to fall to the right of the distribution. Red dashed lines show how the current value, either noise or an event, will fall on the PDF.

False detections occur when the noise becomes correlated and produces a high Fisher statistic value with a probability just below the threshold. To account for these false positives, we calculate the probability (Equation 5.7) of the current observation from multiple frequency bands (similar to *Brachet and Coyne*, 2006). This helps to determine if the signal is confined to one frequency band or is connected over multiple frequency bands. The detection is performed for nine 2 Hz frequency bands between 2 and 20 Hz. If the intersection (product) of the probabilities for all the frequency bands is below a threshold (similar to *Elgammal et al.*, 2002), the current time is considered an event. This process helps reduce the number of false positives due to correlated noise in a specific frequency band.

5.3.3 Event Classification

The event classification was performed by Gabriel Trisca of the Computer Science Department and I will briefly touch on his work as it is a crucial aspect of the project.

Once an event has been detected, the next step is to classify the event. An area of artificial intelligence called machine learning uses prior examples to achieve proficiency at a given task, like classification (*Elman*, 1990). Artificial neural networks attempt to model the human brain where neurons or units are connected together and can control the amount of signal passed between neurons with links of varying conductivity. Instead of conductivity, weights are used within an artificial neural network to connect layers together. Based on the input, the weighted connections will be able to classify the input signal on its own based on what the network has learned from past events (*Quinlan*, 1993). Neural networks are a binary classification scheme where the output will be 1 or 0 (yes or no) for classification of the event type.

5.4 Methods

5.4.1 Sensitivity Analysis of Input Parameters

Two parameters control the event detection results: the window size and the significance level (alpha). To determine how these parameters affect event detection, an avalanche signal and a 2-day avalanche cycle was tested for varying window sizes and significance levels. To quantify the error, the l^2-norm (i.e., the vector magnitude, Equation 5.8) was calculated for the difference between the true event indices and

the detected events indices:

$$|\mathbf{r}|_2 = \sqrt{\sum_{k=1}^{n} |x_k - y_k|^2} \tag{5.8}$$

where x_k is the true event indices, y_k is the detected event indices, and $|\mathbf{r}|_2$ is the l^2-norm. The l^2-norm value will include information about false negative detections and any error between the actual event and the automatic detection. A low l^2-norm indicates the automatic detection matched the true event indices.

5.4.2 Avalanche Signal

A small wet avalanche was recorded during the 2-day avalanche cycle (Figure 5.6). The avalanche provides a typical signal for wet avalanches that we expect to encounter throughout deployment. The signal has a small pressure amplitude and was hard to visually distinguish above the noise. However, the Fisher statistic value was well above 55 in the 4-12 Hz bandwidth, indicating a highly correlated signal. The signal also has some high frequency instrument noise just prior to the avalanche, with higher Fisher statistic values and a large amplitude, uncorrelated signal caused by wind. This proves to be a great test as the detection algorithm should not detect this noise.

5.4.3 Avalanche Cycle

126 events were identified through manual observation for a 60-hour period between January 25, 2013 12:00 UTC and January 28, 2013 00:00 UTC. Six different types of events were classified (Table 5.2) based on the timing, back azimuth, and
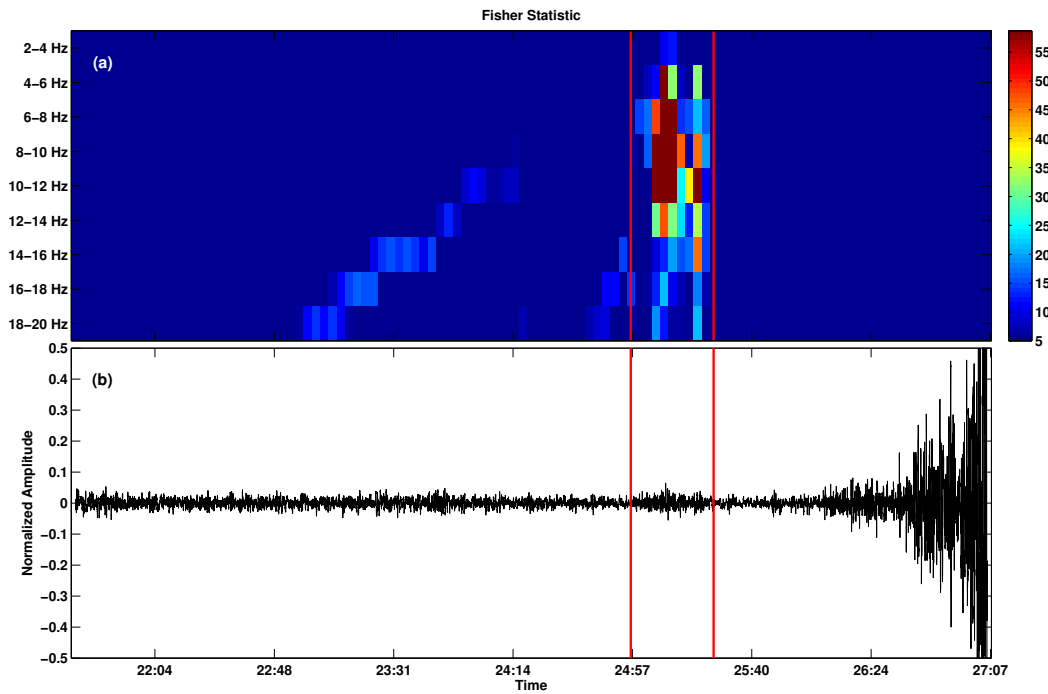
Figure 5.6: Small wet avalanche that occurred during the 2-day avalanche cycle. (a) The Fisher statistic was calculated over nine, 2 Hz frequency bands with most correlated energy in the 4-12 Hz bandwidth. (b) Amplitude signal of the avalanche. The start and end times of the avalanche are shown in red. Note that the avalanche has a small amplitude signal followed by uncorrelated wind signal. This signal is an avalanche as the back azimuth and v_{app} correspond to a known avalanche path.

apparent velocity of the signal. Forty vehicle signals were identified before and after the road was closed at approximately January 25, 2013 19:40 UTC. Four possible avalanche signals were identified during the 3 hours after January 26, 2013 17:32 UTC, while the road was closed. Other events include likely aircrafts from Mountain Home Air Force Base (MHAFB) out of the southwest, planes flying overhead, and the possible clean up effort. Sixty-five unknown signals were found that might contain already identified events but were not convincing.

The Fisher statistic values for each event are shown in Figure 5.7 as compared to

Table 5.2: Events manually identified during the 2-day avalanche cycle.

Event Type	Number of Events
MHAFB	4
Plane	6
Possible Avalanche	4
Rotary (Possible)	7
Unknown	65
Vehicle	40
Total	**126**

the background Fisher statistic values for the 2-20 Hz bandwidth. Most of the events had a higher median Fisher statistic value than the background.
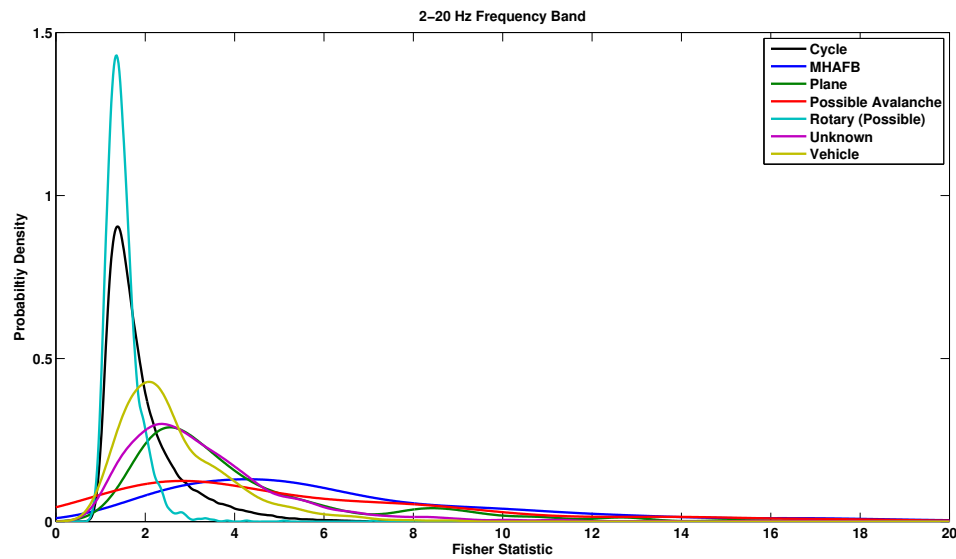
Figure 5.7: Cycle background compared to the six events.

5.4.4 Event Classification

Once an event was detected, the necessary event properties were calculated for event classification. The neural network uses the Fisher statistic, power between 1-

5 Hz, power between 5-10 Hz, power between 10-15 Hz, and the back azimuth for classification. The properties were input to the neural network, which returns a time series of the network output. If the maximum output was above a given threshold, the event is classified for the given network.

Training a neural network requires a large dataset of previous events. However, we do not have a large number of events picked from previous seasons. To test the detection and classification, we have created two neural networks. One for vehicle classification, which has the largest number of events, and another for avalanches.

5.5 Results

For this dissertation, the results will focus on the detection algorithm and only touch on the classification results. For in-depth classification results, please refer to the Idaho Transportation Department's technical report for this project (*Havens et al.*, In Prep).

The results will first go over the sensitivity analysis of the event detection for the single avalanche and the 2-day avalanche cycle. Secondly, the results from the neural network training and classification will be briefly touched on for an avalanche and vehicle neural network.

5.5.1   Event Detection

Avalanche Signal

A range of values for the window size and alpha value were chosen for detection of a single avalanche event. The l^2-norm of the residual is shown in Figure 5.8. Small
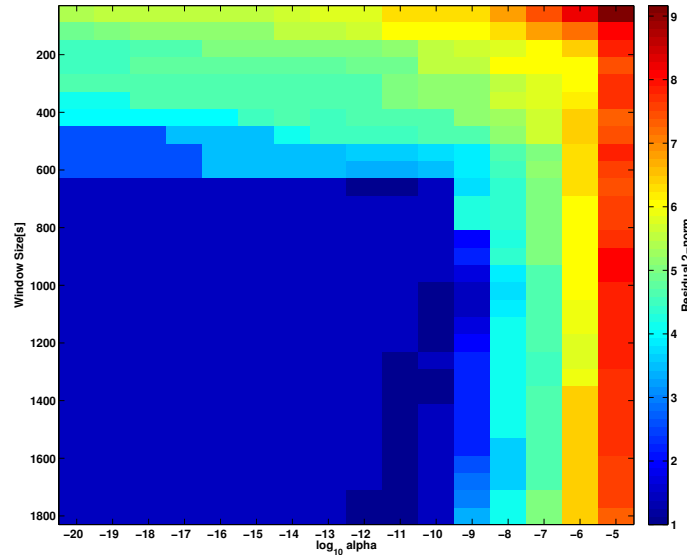
Figure 5.8: Sensitivity of the window size and significance level on the l^2-norm of the residual. High significance level and small window sizes produce the most error in the detection with almost perfect detection in dark blue. The most accurate detection occurs with an alpha value around 10^{-10} and a window size greater than 600 seconds.

window sizes under 600 seconds tended to have a larger error for all alpha values. Large alpha values over 10^{-9} had a large error for all window sizes. For both large window sizes and small alpha values, the error was attributed to not detecting the start and end times perfectly, but detecting the middle of the avalanche. Almost perfect detection (dark blue in Figure 5.8) occurred for alpha values in the 10^{-12} to 10^{-10} range with window sizes generally larger than 1000 seconds.

Using the results obtained from Figure 5.8, a window size of 900 seconds and an alpha value of 10^{-10} were chosen for this avalanche. The detection results in Figure 5.9(b) show low probabilities that the Fisher statistic has been previously observed when the avalanche occurs. The instrument noise has low probabilities but are confined to non-overlapping frequency bands that do not trigger an event

detection. The start and end times of the automatic detection match well with the manually picked start and end times for the avalanche (Figure 5.9c).
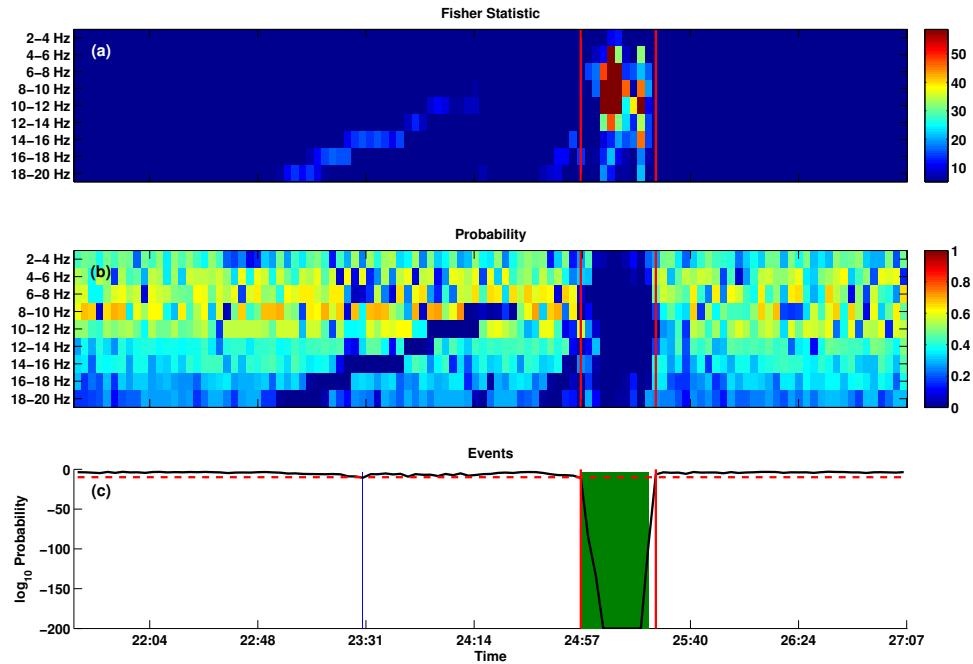
Figure 5.9: Detection of the small wet avalanche. (a) Fisher statistic values. (b) Probability of the current observation, low values indicate a new observation and high values indicate a value that has been observed before. (c) Product of the probabilities in black with the automatic detection in green. The red lines indicate the actual start and end time of the avalanche.

Avalanche Cycle

Each event was treated as a single detection to determine how well the various window sizes and alpha values could detect the start and end times as well as reducing false positives around the event. The mean and standard deviation of the l^2-norm is shown in Figure 5.10. Small windows sizes under 600 seconds tended to have slightly
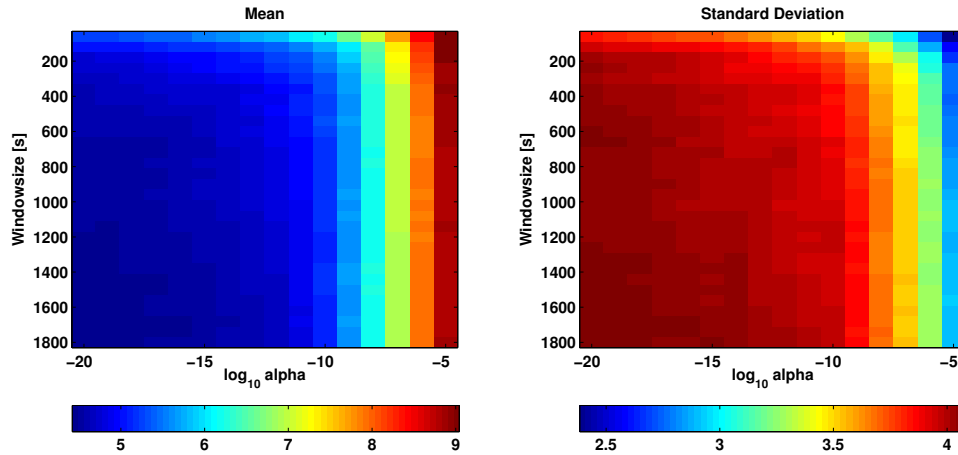
Figure 5.10: The mean and standard deviation of the l^2-norm for all the events.

higher l^2-norm values. Large alpha values over 10^{-9} tended to have a large error for all window sizes. However, when the alpha value was decreased, the standard deviation of the l^2-norm increased, indicating less consistent detections. Therefore, the best values will be around an alpha of 10^{-10} and a window size of around 900 seconds. These values provide a good trade off between consistent and accurate detections while reducing the number of false positives.

Each event type has a different window size and alpha value combination that optimizes the detection (Figure 5.11). All events have larger l^2-norm when the alpha value is above 10^{-9}. Window sizes around 900 seconds and an alpha value of 10^{-10} have lower l^2-norm values for all events.

5.5.2 Event Classification

Two neural networks were created for classification, one for vehicles and the second for avalanches. The avalanche neural network (Figure 5.12) outputs a high value that is above the threshold, which indicates that the event was classified as an avalanche.
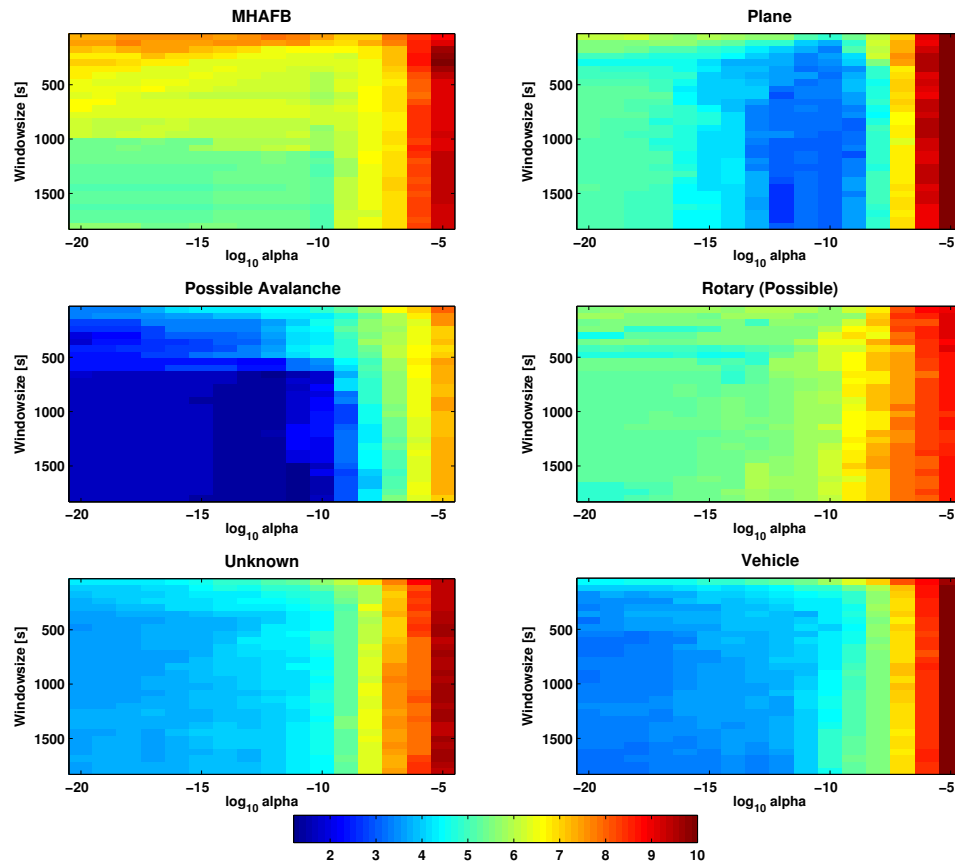
Figure 5.11: Median values of the l^2-norm for all six event types identified.

The avalanche neural network outputs close to zero for an airplane signal, which is below the threshold and is classified as "not an avalanche." The same was true for the vehicle neural network (Figure 5.13) that correctly classifies a vehicle and does not classify the avalanche as a vehicle.
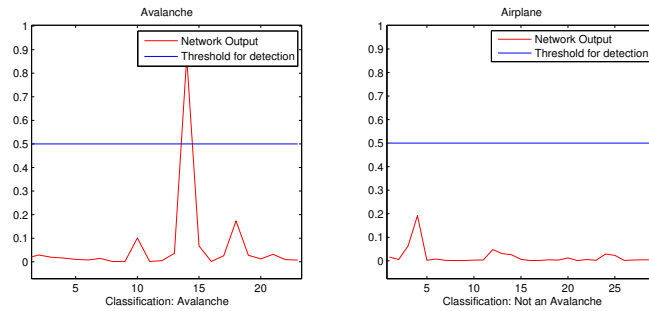
Figure 5.12: Avalanche neural network results for classifying an avalanche as an avalanche and an airplane as not an avalanche. From *Havens et al.* (In Prep).
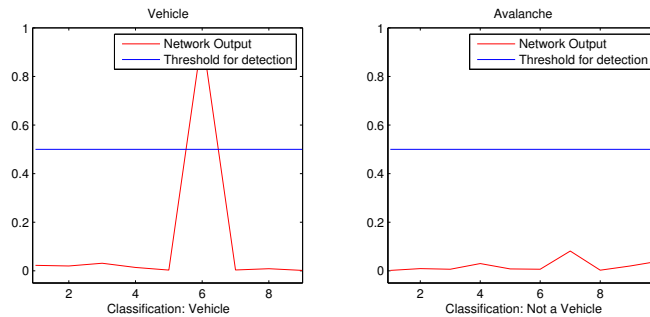
Figure 5.13: Vehicle neural network results for classifying a vehicle as a vehicle and an avalanche as not a vehicle. From *Havens et al.* (In Prep).

5.6   Discussion and Conclusion

This chapter has outlined a new method for signal detection using non-parametric methods and array processing techniques. Non-parametric methods are advantageous over fitting the data to a certain distribution (*Arrowsmith et al.*, 2008) as no assumptions need to be made about the underlying distribution. A window of Fisher statistic data was used as a background model with which to compare new values. A larger window will create a more stable background model that will be less adaptive to changes in the noise, but will be better at filtering out false positives.

Sensitivity analysis performed on a 2-day avalanche cycle and a single avalanche

showed that the automatic event detection was highly dependent on the alpha value. A large alpha increased the number of false positives and decreasing alpha lowered the number of false positives but still had trouble correctly identifying the full event. A trade off between more accurate detection and increased false positives occurred with a window size of 900 seconds and an alpha value of 10^{-10}.

The neural networks could correctly classify the six event types observed in the 2-day avalanche cycle. However, the limited number of training events for avalanches, airplanes, MHAFB, and the rotary make the neural network output sensitive to new events due to over-training on the samples. This may lead to false negatives where an event was incorrectly misclassified due to underrepresentation in the training sample. Therefore, a larger dataset for avalanches will be required for robust classification.

It is better to automatically detect more events using a slightly higher alpha rather than missing a small but significant event. All detected events are sent to the neural networks for classification, which will filter out significant events from non-significant events. However, the neural network is just the first step and a human analyst will still be required to confirm the networks classification.

The ability to train separate artificial neural networks to classify different types of events allows the system to be highly accurate in its results. In other words, instead of having an expert that can always correctly classify any kind of event, we use multiple expert classification systems that are only accurate in classifying a single kind of event and then conducting a vote among them to determine the most likely classification.

The value of this approach is that, while the network training is more time consuming than having a single network, we can detect events in two scenarios: by direct vote or by exclusion. We can confidently say that vehicles will always produce a

similar signal in our sensor array, while other natural phenomena, like avalanches, are bound to change. With this information, we can assume that an event is an avalanche not only if the "avalanche classification network" labels the event as an avalanche, but also if all the other networks (a vehicle, explosion, airplane network, etc.) classify the event as not any of those labels. If the event is not any of the well-known types of events, there is a higher probability that it is an avalanche.

CHAPTER 6:

CALCULATING AVALANCHE VELOCITY

Summary

Besides detecting avalanches, infrasound can be used to estimate avalanche properties. On January 19, 2012, a large avalanche was recorded on a nearby infrasound array. The array geometry in relation to the avalanche path allowed for a high resolution estimation with uncertainty of the avalanche velocity as it moved down the avalanche path both spatially and temporally. In this chapter, we present a new technique for calculating the velocity using array processing techniques and Monte Carlo simulations to estimate the probable source location.

Just prior to the avalanche, a small signal originated from the start zone. We believe this signal to be the failure of the snowpack and the movement of the snow surface creating a small but detectable signal. This is the first published reference of snowpack failure recorded with infrasound. Ten seconds after the failure, the avalanche could be detected and tracked as it moved downslope.

The manuscript presented here was published September 2014 in the *Geophysical Research Letters* (GRL) and is my second published paper (*Havens et al.*, 2014). This paper targets a broad audience and we hope to show that infrasound can be used as tool not only for detection but for estimating avalanche properties. In the future, infrasound combined with video, wave propagation modeling, and avalanche dynamics modeling could provide much needed insight into avalanche dynamics.

This work was presented at the International Snow Science Workshop in Banff, Alberta in September 2014.

Some minor changes were made to the following version to address questions from my committee.

Calculating the Velocity of a Fast Moving Snow Avalanche Using an Infrasound Array

Scott Havens[*], Hans-Peter Marshall[*], Jeffery Johnson,[*] and Bill Nicholson[†]

[*]Center for Geophysical Investigation of the Shallow Subsurface, Boise State University, Boise, Idaho, USA

[†]Idaho Transportation Department, Boise, Idaho, USA.

6.1   Abstract

On 19 January 2012, a large D3 avalanche (approximately 10^3 tons) was recorded with an infrasound array ideally situated for observing the avalanche velocity. The avalanche crossed Highway 21 in Central Idaho during the largest avalanche cycle in the 15 years of recorded history and deposited approximately 8 meters of snow on the roadway. Possible source locations along the avalanche path were estimated at 0.5 second intervals and were used to calculate the avalanche velocity during the 64-second event. Approximately 10 seconds prior to the main avalanche signal, a small infrasound signal originated from the direction of the start zone. We infer this to be the initial snow pack failure, a precursory signal to the impending avalanche. The avalanche accelerated to a maximum velocity of $35.9 \pm 7.6 ms^{-1}$ within 30 seconds before impacting the highway. We present a new technique to obtain high spatial and temporal resolution velocity estimates not previously demonstrated with infrasound for avalanches and other mass wasting events.

6.2   Introduction

Avalanche generated infrasound was first detected on infrasound sensors deployed by the National Oceanic and Atmospheric Administration (NOAA) in Boulder, CO (*Bedard Jr.*, 1989, 1994; *Bedard Jr. et al.*, 1988). The authors found avalanches generate acoustic signals in the 1-5 Hz region and the work led others to develop infrasound systems focused on avalanche detection (*Chritin et al.*, 1996; *Scott et al.*, 2007; *Ulivieri et al.*, 2011). Several systems are now used operationally by highway forecasters in the United States, which provide necessary information on avalanche activity to avalanche forecasters (*Yount et al.*, 2008).

One method previously demonstrated for tracking avalanches uses seismometers in the avalanche path and detects when the avalanche reaches each station (e.g., *Vilajosana et al.*, 2007a). Using the location of the seismometers and the time the avalanche moves over the seismometers, the velocity between stations can be calculated. *Lacroix et al.* (2012) deployed a seismometer array away from the avalanche path and used beam forming to calculate the velocity as a function of time. Typical avalanche velocities using seismic methods from previous studies are shown in Table 6.1. Avalanche velocities calculated using seismic methods show avalanche average velocities vary between 5 and 57 ms^{-1} for dry and wet avalanches.

Other techniques for tracking avalanche velocity include videogrammetry (*Vallet et al.*, 2004), arrays of pressure pylons placed directly in the avalanche path (*Kogelnig et al.*, 2011), or upward looking Frequency Modulated Continuous Wave (FMCW) radars (*Gubler and Hiller*, 1984). A FMCW doppler radar placed at the base of the path (*Vriend et al.*, 2013) can calculate the avalanche velocity over time using feature tracking but is constrained to monitor only a single avalanche path and can

be prohibitively expensive.

Table 6.1: Avalanche velocities calculated using different methods.

Source	Avalanche Type	Method	Velocity (ms^{-1})
Kishimura and Izumi (1997)	Dry avalanches	Seismic	25-57
Lacroix et al. (2012)	Dry and wet avalanches	Seismic	12-32
Takeuchi et al. (2003)	Dry and wet avalanches	Seismic	20-43
Vilajosana et al. (2007a)	Dry avalanches	Seismic	5-55
Caplan-Auerbach et al. (2004)	Ice avalanche from volcano, triggered by earthquakes	Seismic	14-70
van der Woerd et al. (2004)	Earthquake triggered ice avalanche	Seismic	21-35
Huggel et al. (2007)	Large ice avalanches from volcano	Seismic	22-70
Vallet et al. (2004)	Dry avalanche	Video-grammetry	10-55
Kogelnig et al. (2011)	Dry and wet avalanches	Pressure pylons	20-55
Vriend et al. (2013)	Dry avalanches	FMCW radar	5-40

Other mass wasting events, like pyroclastic flows, have similar flow dynamics and behaviors to avalanches. *Ripepe et al.* (2009) tracked a pyroclastic flow with an infrasound array and first gave insight into calculating the velocity with infrasound. However, the authors only looked at the average velocity of the flow during the entire event. *Yamasato* (1997) tracked pyroclastic flows using both seismic and infrasound sensors deployed around the volcano. The velocity was estimated using the Doppler shift of the infrasound microphones.

Here we present an avalanche event that was recorded on a nearby infrasound array that was ideally situated to record the avalanche over a large change in backazimuth. Using array processing techniques and Monte Carlo simulations of probable source

locations, we calculate the velocity with uncertainties for the avalanche.

6.3   The 96.92 Avalanche Event

6.3.1   Avalanche Cycle

The avalanche cycle on 19 January 2012 proved to be one of the largest avalanche cycles that the Highway 21 corridor has ever experienced (Figure 6.1a). Two separate avalanche cycles occurred during the 7-day storm: the first avalanche cycle produced large dry avalanches, and the second avalanche cycle produced medium wet avalanches. In the two and a half days leading to the first avalanche cycle, the storm produced 0.07 meters of water and approximately 0.56 meters of snow at a automated weather station (2180 m above sea level (a.s.l)) 16 kilometers to the north at Banner Summit.

After the storm cleared, the storm totals were 1.34 meters of snow, 0.129 meters of water, and 57 reported avalanches. Debris on the highway ranged from 1.5 to 8 meters deep from 37 different avalanches. Figure 6.1a provides an overview of the highway corridor and the avalanche paths that were active during the avalanche cycle.

6.3.2   Path Characteristics

The 96.92 avalanche path is a small avalanche path with a high return interval (about 2.5 avalanches per year). The starting zone is relatively small, estimated to be 60 to 100 meters wide, with a maximum elevation of 1970 m a.s.l. The avalanche track (Figure 6.1b) is a maximum of 620 meters in length, has an average slope of 31° with a maximum slope of 37° in the middle of the path, and has a vertical drop
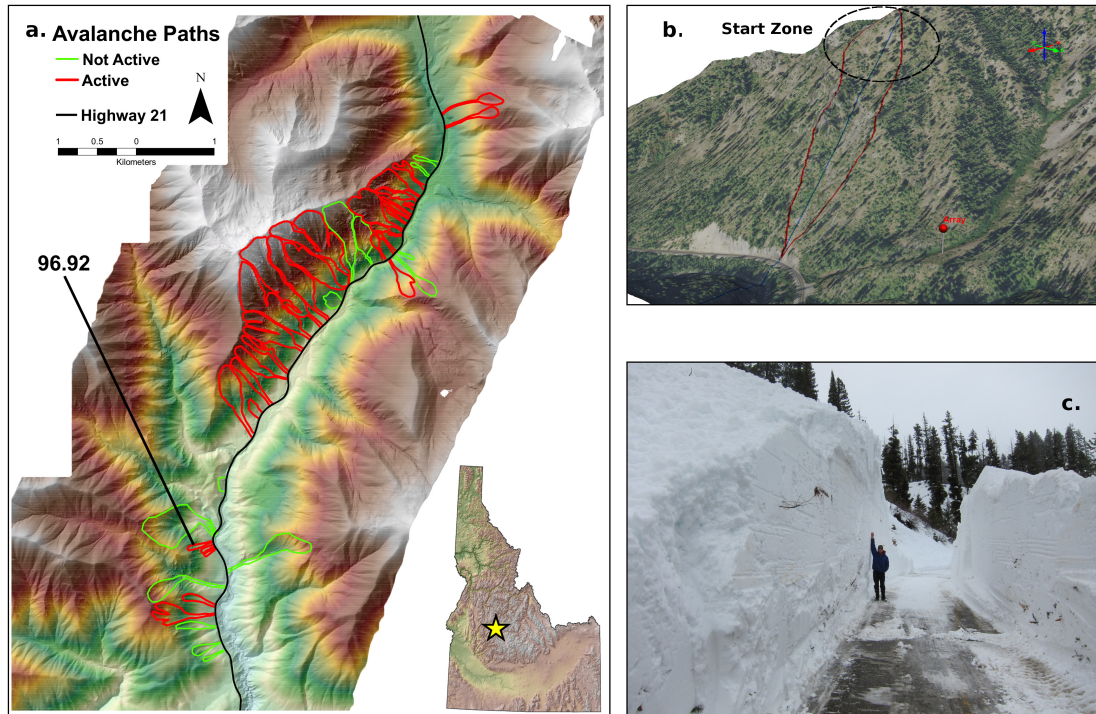
Figure 6.1: a) Overview of Highway 21 through the Canyon Creek corridor in Central Idaho. A significant number of the major avalanche paths had evidence of extremely large dry avalanches, which occurred during the 19 January 2012 cycle. A total of 57 avalanches were reported in the area, with 37 avalanches that covered the highway with 1.5 to 8 meters of snow. b) Three-dimensional rendering obtained from a 2 meter aerial LiDar survey, overlain with 0.5 meter ortho photo. The maximum extent of 96.92 is outlined in red with the path profile in blue. The infrasound array was located at the red marker. c) Head avalanche forecaster standing in the middle of the debris pile a day after the 96.92 avalanche event. The debris was approximately 8 meters high on the highway and continued to flow into the creek below. The array location is on the small ridge directly behind the forecaster.

of 370 meters to the highway (1600 m a.s.l.). The path does not have a run out zone where the avalanche can slowly lose momentum. Instead, the avalanche funnels through a 15-meter channel immediately before reaching the highway (Figure 6.1c). Large events typically continue across the highway and into the creek below.

6.3.3   Avalanche Characteristics

The avalanche occurred on 19 January 2012 at 16:36 UTC and lasted approximately 64 seconds. The signal amplitude (Figure 6.2a) shows the classic infrasound signal characteristics of an avalanche with a gradually increasing (t=30s) amplitude as the avalanche gains momentum and size (*Kogelnig et al.*, 2011), then decreasing amplitude (t=60s) as the avalanche reaches the highway and stops. A maximum pressure of just under 1.5 Pascals (t=55s) was recorded when the avalanche was approximately 300 meters from the array.

Prior to the avalanche at t=14 seconds (Figure 6.2), there was a small precursory signal before the signal direction moves downslope. We hypothesize that the signal was from the snowpack fracture propagation, which displaced the snowpack and caused the pressure wave in the air (i.e., a "whumpf," *McClung and Schaerer*, 2006). We believe that this is the first published example of a potential snowpack failure event captured remotely on an infrasound array. Snowpack failure has been observed during one opportunistic seismic study (*Johnson et al.*, 2004) but has not been recorded with infrasound.

The power spectrum (Figure 6.2b) of the avalanche indicates that most energy was in the 1-10 Hz bandwidth and agrees with previous work (e.g., *Bedard Jr.*, 1994; *Ulivieri et al.*, 2011). High frequency components were prevalent after the avalanche
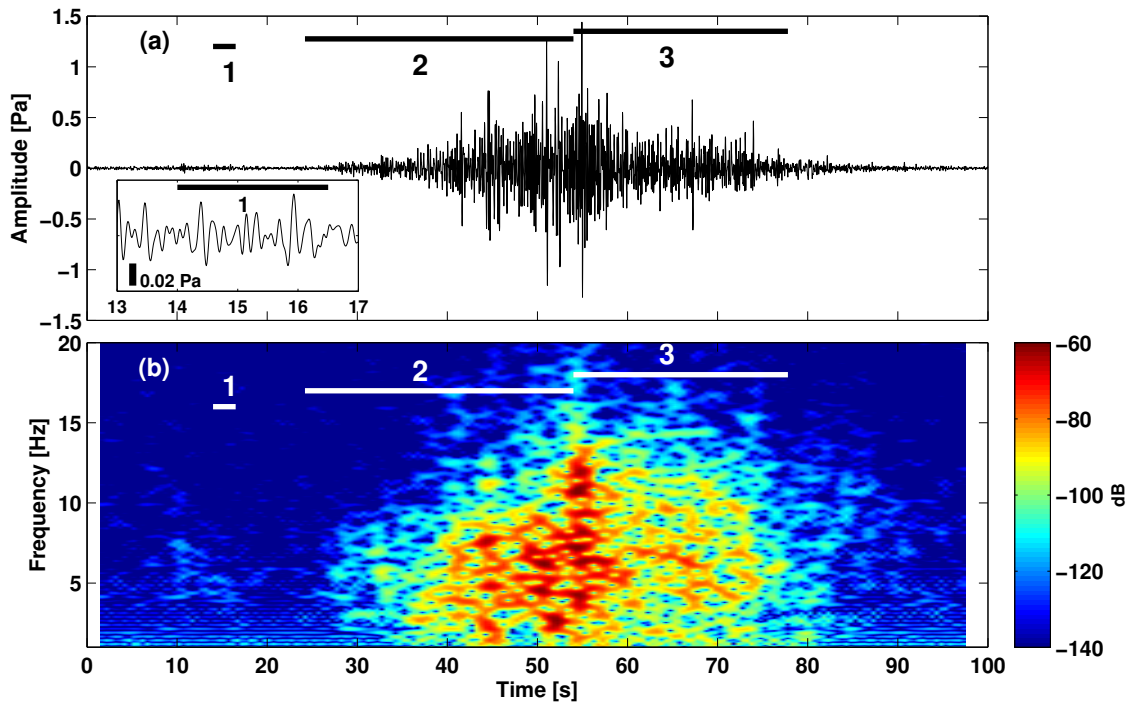
Figure 6.2: (a) Avalanche signal with the three phases marked. The highest amplitude recorded at the array of 1.5 Pa occurred when the avalanche reached the highway. Inlay shows the whumpf signal with a two order of magnitude difference in amplitude. (b) Power spectrum of avalanche with the most power in the 1-10 Hz bandwidth. Higher frequencies appear after avalanche reaches the highway.

reached the highway.

6.4   Methods

6.4.1   Array Configuration

The array was located approximately 550 meters away from the start zone and 270 meters away from where the avalanche path intersects the highway. The back azimuth ranged from 216 (start zone) to 162 (highway) degrees, a 54-degree sweep,

providing an ideal array placement for calculating velocity. The array consisted of 3 infrasound sensors with a flat frequency response in the 1-20 Hz frequency band (*Marcillo et al.*, 2012) and 30 meter spacing in a triangular arrangement. The sensors were recorded on a RefTek 130 at 100Hz and 24-bit analog-to-digital conversion.

6.4.2 Calculating the Fisher Statistic

The Fisher statistic (e.g., *Smart and Flinn*, 1971; *Blandford*, 1974) is a measure of signal coherence and is the power of the beam divided by the average difference in power of the beam and individual channels, where the beam is the shifted and summed signal over all sensors. The Fisher statistic assumes a single point source with perfectly correlated signal and perfectly uncorrelated noise (*Blandford*, 1974). Following *Smart and Flinn* (1971), the Fisher statistic in the frequency domain is defined as:

$$F(\omega, \mathbf{s}) = \frac{E(\omega, \mathbf{s})}{E(\omega) - E(\omega, \mathbf{s})} \cdot (N - 1) \tag{6.1}$$

where

$$E(\omega, \mathbf{s}) = \left| \frac{1}{N} \sum_{j=1}^{N} A_j(\omega) \cdot \exp(-i\omega \mathbf{s} \cdot \mathbf{r_j}) \right|^2 \tag{6.2}$$

and

$$E(\omega) = \frac{1}{N} \sum_{j=1}^{N} |A_j(\omega)|^2 \tag{6.3}$$

with N sensors located at position vectors $\mathbf{r_j}$, $A_j(\omega)$ contains the amplitude information from the Fourier transform, and slowness $\mathbf{s}$.

The slowness vector $\mathbf{s}$ points from the array to the possible source location with the exponential in Equation 6.2 applying the necessary time shifts for the array geometry given the source location. The slowness vector was calculated every 2 meters

horizontally along the path profile (Figure 6.4c), which was derived from a 2 meter Digital Elevation Model (DEM). The avalanche path profile consisted of 497 possible source locations. The speed of sound was calculated using an air temperature of -1.1 Celsius (331 ms^{-1}) recorded by a nearby remote weather station. The Fisher statistic (Equation 6.1) was evaluated at each slowness vector **s** along the path. When the Fisher statistic is maximized, the slowness vector provides a direct estimate of the back azimuth and incidence angle to the potential source location.

The frequency wave-number (fk) analysis (*Rost and Thomas*, 2002) determines the time shifts required and evaluates the Fisher statistic for varying slowness vectors. The fk analysis can be performed for a short moving window with a constant step size, but the window size must be large enough to capture the dominant frequency moving across the array. The fk analysis was performed with a 1-10 Hz band-passed signal for a moving window of 4 seconds, overlapped by 3.5 seconds. Therefore, all potential source locations are evaluated along the path for each overlapping time window.

A 10-minute period where no signals were present just prior to the avalanche was used to evaluate the threshold value of the Fisher statistic. In the 1-10 Hz bandwidth, the Fisher statistics fell into the probability density function (PDF) shown in Figure 6.3 with a 0.99 quantile of 3.52. The quantile became the Fisher statistic threshold value to evaluate whether or not a signal was present above the noise.

6.4.3   Calculating Velocity

Avalanches, similar to other mass wasting events like pyroclastic flows, are a complex moving source believed to produce the majority of infrasound near the front of the flow (*Yamasato*, 1997). To determine the most probable source location of
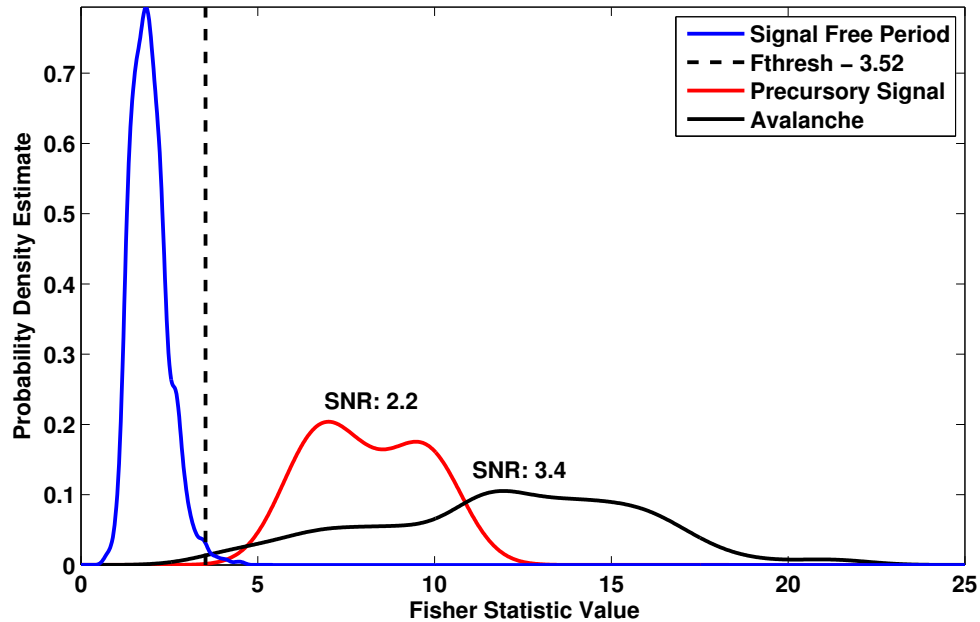
Figure 6.3: The probability density function (PDF) of the 10 minute signal-free period, the precursory signal, and the avalanche are compared. The Fisher statistic threshold was the 0.99 quantile of the signal-free period. The median value of the signals over the threshold was the signal-to-noise ratio (SNR), with the precursory and avalanche signal well above the Fisher statistic threshold value.

the avalanche, the Fisher statistic was calculated as a function of position along the avalanche path (Figure 6.4c). High Fisher statistic values represent a higher probability of the source location, similar to a PDF. The higher the probability density (or Fisher statistic value) the more likely the source came from that particular location along the avalanche path.

The estimated source location as a function of time was determined by randomly sampling the probable source locations based on the Fisher statistic at each time step. At each time step, a cumulative distribution function (CDF) is calculated for all Fisher statistic values along the avalanche path. The CDF provides a distribution for the

Fisher statistic values at the current time step, with higher Fisher values having a higher probability on the CDF. The CDF is randomly sampled where a higher Fisher statistic has a higher probability of being randomly chosen. The associated location of the sampled Fisher statistic value became the potential source location for that time step.

The velocity is the derivative downslope with a 2 meter horizontal distance and 0.5 second time interval. To reduce the effect of large location jumps due to random sampling, the velocity was smoothed with a 12 second Gaussian kernel corresponding to a 2.5 second bandwidth. The kernel length was chosen to reduce the amount of high frequency noise in the velocity estimate. This would provide a smooth velocity solution that would represent the velocity of the bulk avalanche flow and not track small signals from the avalanche that may not be moving at a smaller than 2.5 second time scale.

One thousand Monte Carlo simulations were performed to randomly sample the Fisher statistic values to determine the median and interquartile range (IQR) of the velocity. This provides an estimate of the velocity and uncertainty as a function of time for the 64-second event. Monte Carlo methods are favored over direct calculation of the velocity from the maximum Fisher location as the maximum location will be corrupted with sources that do not represent the bulk avalanche flow. With the Monte Carlo methods and Gaussian smoothing, the smaller sources will be smoothed and the velocity estimate will follow more closely to the velocity of the bulk avalanche flow.

6.5 Results and Discussion

6.5.1 The Three Avalanche Phases

The avalanche can be described in three different phases: the initial failure, acceleration in the track, and impact with the highway (Figure 6.4).

First Phase

The first phase was a small signal originating from the start zone at t=14 seconds and lasting approximately 2.5 seconds. The signal has a peak amplitude of 0.035 Pa with the majority of the energy in the 4-9 Hz bandwidth. The signal was well above the background level of the Fisher statistic during the signal-free period (Figure 6.3) with a signal-to-noise ratio (SNR) of 2.2. This indicates a significant signal originated from the avalanche start zone (Figure 6.4a) just prior to the avalanche.

We interpret the precursory signal as the fracture initiation and propagation within the snowpack. *Johnson et al.* (2004) measured a propagating failure using a string of geophones on the snow surface in a flat meadow. The fracture propagated away from the trigger point at 20 ms^{-1} from a compressive fracture that created a bending wave in the overlaying slab due to the sudden vertical movement. Similar fracture propagation velocities of 27 to 36 ms^{-1} have been observed in snow stability tests recorded with high speed video (*van Herwijnen et al.*, 2010). *Bair et al.* (2012) used high speed video to estimate the vertical displacement of the slab and measured 1-2 mm of vertical movement in storm snow. The vertical slab movement induces a vibration in the atmosphere just above the slab, causing the "whumpf" sound (*Schweizer et al.*, 2003).
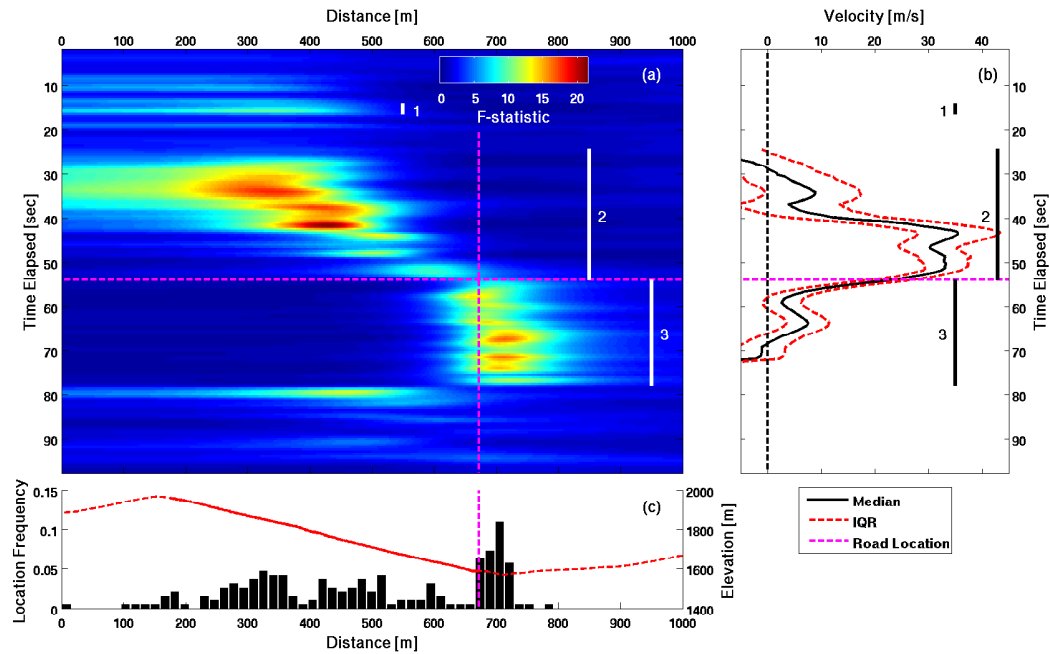
Figure 6.4: (a) F-statistic evaluated at each point along the path profile in the 1-10 Hz bandwidth. The three avalanche phases are shown with the highway location highlighted in purple. (b) Velocity of avalanche was slow to start, but reaches a maximum of $35.9 \pm 7.6 ms^{-1}$ just before reaching the highway. (c) The 96.92 path profile in dashed red with a histogram of the maximum F-statistic locations through time. The solid red shows the maximum extent of the 96.92 avalanche path with the snowpack failure and avalanche motion originating around 300-320 meters.

The precursory signal has a small amplitude, which is consistent for a small vertical displacement of the slab (Figure 6.2a). If the fracture propagated across the entire start zone of 60 meters over a measured 2.5 seconds, the average propagation velocity would be 24 ms^{-1}, which agrees with values observed by *van Herwijnen et al.* (2010).

Second Phase

The second phase starts at 24.2 seconds with the first detectable signal from the avalanche and lasts until the avalanche reaches the highway at 54.0 seconds (Figure

6.4a). The time delay between the first and second phase could be due to the time needed for the failure to propagate across the slope and for the avalanche to reach the minimum momentum to generate detectable infrasound caused by atmospheric displacement (*Kogelnig et al.*, 2011). Between the first and second phases, the Fisher statistic ranges between 2.0 and 3.5, which was below the threshold. This indicates that there was no significant signal detected.

As an avalanche moves down the path, a suspension layer forms at a velocity of approximately 10 ms^{-1} (*McClung and Schaerer*, 2006) due to the turbulent eddies caused by the friction between the avalanche and atmosphere. We believe a suspension layer formed sometime between 24.2 and 43.3 seconds as the avalanche gained momentum. Once the suspension layer formed, the avalanche quickly accelerated to the maximum velocity of $35.9 \pm 7.6 ms^{-1}$ approximately 300 meters from the highway (43.3 seconds). A small decrease in velocity can be seen in Figure 6.4b before increasing to $33.5 \pm 4.2 ms^{-1}$ at 48.8 seconds right before impact with the highway. Our velocity observations are smoothed in space and time and this therefore provides a lower-bound estimate of the velocity.

Third Phase

The third phase occurs after the avalanche impacts the highway at 54.0 seconds. The infrasound signal recorded comes from a constant location at the intersection of the avalanche path and highway, as the avalanche continues to deposit snow on the highway and overflows into the creek for 23.8 seconds.

6.5.2 Avalanche Velocity

The average velocity of the avalanche was 14.5 ms^{-1} from the first major signal at 24.2 seconds to the impact with the highway at 54.0 seconds and was in the lower range of previous observations (Table 6.1). The average velocity was of reasonable magnitude but is highly path dependent as the avalanche did not likely have enough time to reach a steady terminal velocity and was possibly still accelerating when it impacted the highway due to the uncertainty in the velocity estimate.

The measured avalanche velocity can be described by the velocity of a mass gaining momentum as it moves down slope (Figure 6.4b). Initially, the velocity was small as the initial snow mass began to move. As the avalanche gained momentum, a suspension layer likely formed and produced a high-amplitude infrasound signal (*Kogelnig et al.*, 2011) with high Fisher statistic values. The avalanche accelerated quickly to a maximum velocity of $35.9 \pm 7.6 ms^{-1}$ within approximately 300 meters of the highway as more snow was entrained right before it impacted the highway.

6.6 Conclusions

For the first time, the velocity time series of an avalanche was tracked from beginning to end using an infrasound array with optimal placement. Most seismic studies of avalanches have only been able to determine the average avalanche velocity, with a few studies calculating velocity time series for a specific path from radar (Table 6.1). The average velocity we calculated (14.5 ms^{-1}) was significantly less than the estimated maximum velocity of $35.9 \pm 7.6 ms^{-1}$ and was in the lower range of previous observations, likely due to the relatively short avalanche path.

The large avalanche had three distinct phases. The avalanche started with the failure of the weak layer 10 seconds prior to the first detectable signal of the avalanche. We believe this to be the first time a possible weak layer failure has been captured using infrasound. Having the array 550 meters from the start zone allowed for the detection of the small amplitude signal. Once the avalanche gained momentum, it quickly accelerated downslope to a maximum velocity of $35.9 \pm 7.6 ms^{-1}$ before impacting the highway. After the avalanche front impacted the highway, it takes 23.8 seconds for the remaining mass of the avalanche to lose momentum as it reached the highway and filled the creek below.

The technique presented is promising for estimating the velocity of a moving source when the infrasound array is ideally located close to the avalanche path with a large change in back azimuth. However, the technique may not apply to events further away from the array as there may not be the necessary back azimuth range needed to calculate a high resolution velocity estimate.

In the future, infrasound combined with video and time lapse photography will help determine the sources of infrasound generated by the avalanche. The measured air pressure and velocity estimates, combined with an avalanche dynamics modeling, could allow infrasound estimates of the volume and mass of snow deposited on the highway, which would be useful for estimating highway clean up requirements for multi-day closures.

Acknowledgments

CHAPTER 7:

AVALANCHE DETECTION SYSTEM

7.1 Introduction

7.1.1 Description of the Research Problem

Avalanches routinely occur on Highway 21 between Lowman and Stanley, Idaho each winter, which poses a threat to the safety of maintenance workers and the traveling public. When Highway 21 was first opened during the winter, the avalanche hazard mitigation was to close the road for long periods of time. Once a formal avalanche forecasting program was developed, the number of days closed has been significantly reduced (Figure 7.1). The goal of the real time avalanche detection system is to provide another tool for ITD avalanche forecasters to utilize when making decisions about avalanche hazards along Highway 21.

7.1.2 Purpose of Project

A real time avalanche detection system will allow the Idaho Transportation Department (ITD) avalanche forecasters to remotely monitor the major avalanche paths. This information will:

1. Alert ITD forecasters when smaller avalanches are occurring that do not block the road, which indicates regional avalanche activity and instability trends.

2. Monitor avalanches at night when traffic volume is low and emergency response
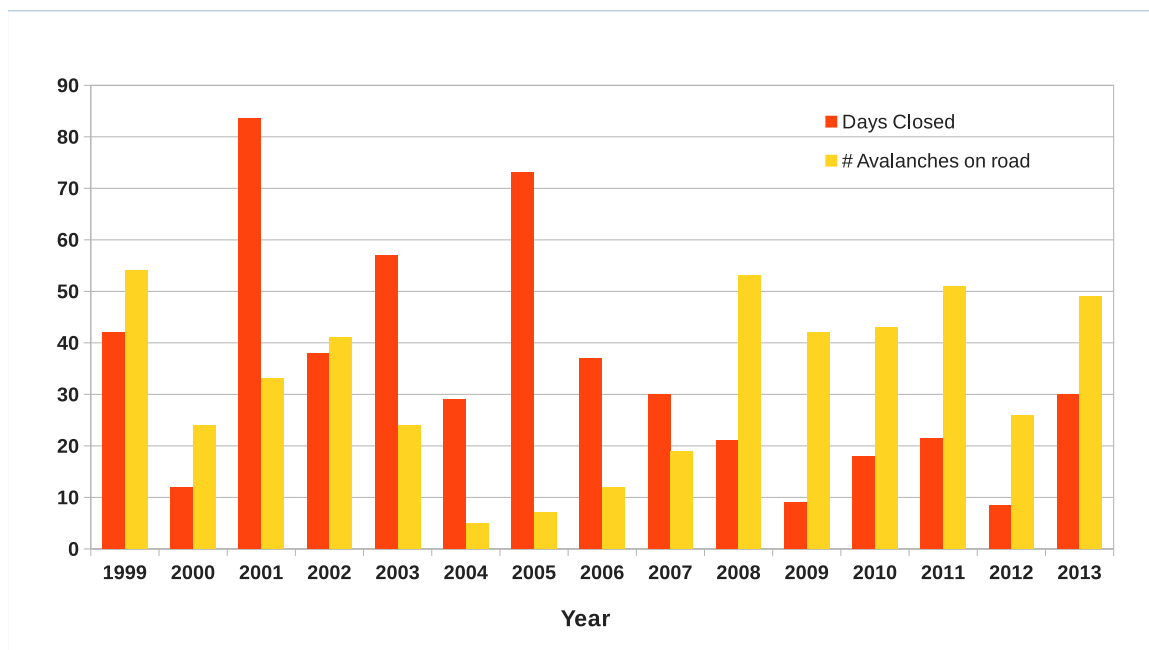
Figure 7.1: The number of avalanches that hit Highway 21 in relation to the number of days Highway 21 is closed.

    is limited.

3. Provide an emergency alert in the unlikely event that the road is open when avalanches occur, as the highway could be closed immediately following any remotely detected avalanche events.

4. Improve information about timing of avalanche events when the road is already closed, aiding in future forecasts and in turn providing avalanche information for when the road is safe to open

5. Provide an expandable avalanche detection system design that can be deployed in other areas around Idaho, especially the Highway 12 area.

The objective of this research project was to maintain infrasound arrays for a minimum of two years and develop software for processing and interpretation of avalanche

signals by ITD forecasters.

7.1.3   Real Time Application

Avalanche detection in real time poses a handful of design challenges: 1) the remote location of the avalanche area with no cell phone, radio, or power, 2) must have data available to avalanche forecasters a minimum of 35 miles away within a reasonable time frame, and 3) must be a standalone system that can be deployed anywhere and telemeter back avalanche information.

To decrease the amount of data to transmit, we use a small low power computer to process the infrasound data on-site. The infrasound signals from the sensors are recorded on the data logger, which is connected to the on-site computer (Section 7.2). The on-site computer continuously collects data from the data logger and performs the necessary steps for event detection (Section 7.3). The events are stored in a database on the computer and communicates over telemetry to an event database on the server. The avalanche forecasters can access the event database through a web application. The avalanche forecasters will confirm events in the event database, which will be used to periodically retrain the neural network. A flow chart of the entire real time application is shown in Figure 7.2.

The system allows us to deploy the hardware in remote locations (Section 7.2), process the data on-site (Section 7.3), and telemeter out avalanche information.
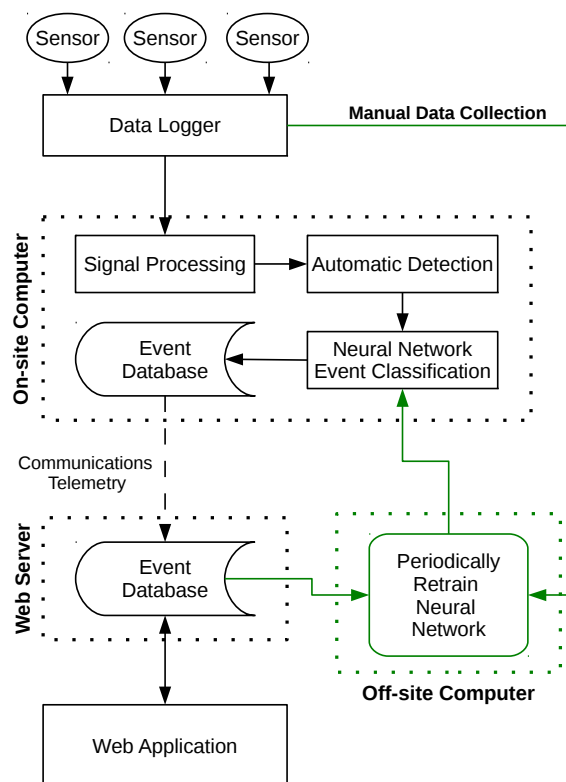
Figure 7.2: Flow chart representing the processing steps for the real time implementation.

7.2   Hardware Development

7.2.1   Hardware

The infrasound hardware consists of four main components: seismic data logger, small low power on-site computer, infrasound sensors, and telemetry. The hardware is powered using a bank of deep cycle batteries charged by a solar panel.

Figure 7.3: Quanterra Q330S data logger from Kinemetrics. Figure from www.kmi.com.

Data Logger

The data acquisition is performed using the Quanterra Q330S data logger (Figure 7.3) from Kinemetrics (www.kmi.com). The Q330S is a 6 channel, high resolution, ultra-low power seismic data logger that has proven performance in the polar regions and excels at telemetering data. Various sample rates exist for the Q330S and we have chosen to use a 100 Hz sampling rate to ensure that all waveforms in the infrasound bandwidth (1-20 Hz) are captured. Timing is obtained from a GPS receiver attached to the Q330S. Table 7.1 shows selected specifications that are used for this project; more can be found at www.kmi.com.

On-site Computer

On-site computing is performed by a low-power computer from fitPC (www.fitpc.com, Figure 7.4). For this project, we have selected the fit-PC2i which is a small energy-efficient computer that has 2GB of RAM, a 1.6GHz processor and runs at 10% the power of a regular PC (Table 7.2). A 120GB solid state hard drive ensures fast reading and writing of data with better performance at lower temperatures. The fitPC runs the XUbuntu Linux distribution. The fitPC automatically restarts when power is applied in the event that power is lost.

Table 7.1: Selected specifications for the Quanterra Q330S. A full data sheet can be found at http://www.kmi.com/Uploads/pdfs/Q330S 20Datasheet.pdf

Channels	6
Gain	30
Sample Rate	100
Resolutions	24-bit A/D
Timing	Precision TCXO, locked to GPS
Telemetry	UDP or TCP IP over Ethernet connection.
Temperature	Fully specified -20 to +50C
	Operative -40 to +70C
Memory	32Mb RAM standard
Network	Dual Ethernet
Serial Ports	1 console ports
Media	Dual USB up to 32G total
Power	<0.8W avg. 12VDC, additional 1.2W for continuous Baler operation.
Size	17 x 4 x 6 in., 9 lbs.

The data processing (Section 7.3.3) is very fast and does not require the computer to be on full time but is put to sleep between processing windows to further conserve power. Typically the computer may be on for 10 to 20 minutes per hour, which is equivalent to a 2-4 Watt power consumption.

Infrasound Sensors

The first two years of this project (2010-2012) used a piezoresistivity pressure traducer (PPT) manufactured with micro-electromechanical systems (MEMS) technology developed at New Mexico Institute of Mining and Technology (Infra-NMT *Marcillo et al.*, 2012). Infra-NMT sensors use the change in resistance due to the displacement of a diaphragm to measure the infrasound signals. The sensors have a flat frequency response in the infrasound bandwidth and a sensitivity of $\sim 45\mu V Pa^{-1}$,

Figure 7.4: The fit-PC2i from fitPC. Figure from www.fitpc.com.

Table 7.2: Selected specifications for the fit-PC2i. More information can be found at http://fitpc.com/products/fit-pc2i.

Weight	13 oz
Size	4 x 4.5 x 1.05 in.
Power	Low load 6W
	Full load 8W
	<1W standby
Network	2 x ethernet ports, 802.11 wifi
Ports	miniSD, HDMI, audio, 2 ethernet ports, 4 USB 2.0
Memory	2GB
Processor	Intel Atom Z530 1.6 GHz

making it an ideal sensor for research purposes. However, this sensor was developed for volcanic studies where signals are generally above 1 Pa. The signals generated from avalanches are typically much less than 1 Pa and are difficult to detect with the Infra-NMT sensors.

Therefore, we developed a new infrasound sensor that uses an electrical condenser microphone (ECM) typically found in phones and computers. ECMs use one plate of a capacitor as a diaphragm that changes capacitance when deflected, which can be measured. Since ECMs were developed for phones that operate in the threshold

of human hearing (20 to 20,000 Hz), the sensors must be adapted for use in the infrasound bandwidth and can have a different frequency response for each sensor. However, these sensors have proven useful for infrasound studies of volcanoes (*Johnson et al.*, 2003; *Ripepe et al.*, 2007) and previous avalanche detection studies (*Scott et al.*, 2007). The extreme low cost of these sensors and higher signal-to-noise ratio (SNR) than the Infra-NMT, make them ideal for detection of small amplitude signals.

Telemetry

Telemetry is achieved with an Iridium satellite modem for proof-of-concept telemetry. The modem sends small text files (<1 KB) created by the fitPC based on detected events. The satellite modem is for testing purposes only, as sending large amount of data is not economically feasible.

7.2.2 Real Time Installation

Figure 7.5 shows the main components deployed in the field. Power from the solar panel is connected to a battery bank and is controlled with the charge controller. Power from the battery bank is distributed through the power box where the Q330S, fitPC, and modem are connected. The infrasound sensors come into the box and are connected to the sensor input cables of the Q330S. The console port serves two uses, first to connect with the fitPC through the ethernet cable, and second to apply power. When an event is detected, the fitPC creates a telemetry file, which is sent to the Iridium modem for transmission to the off-site server.
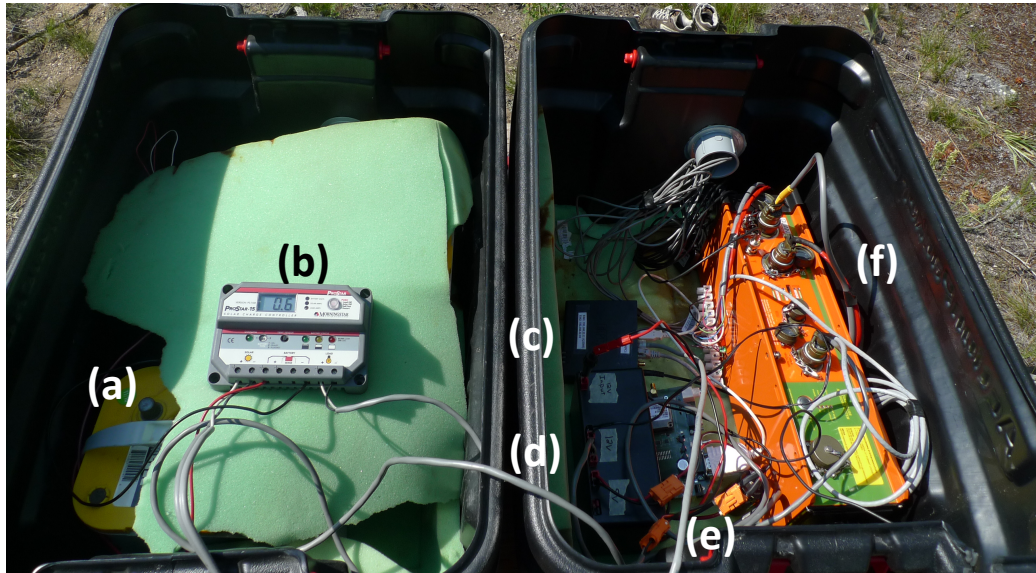
Figure 7.5: Real time system components deployed in the field. (a) Deep cycle batteries, ∼150Ah. (b) Charge controller to manage charging of batteries from solar panels. (c) FitPC. (d) Power box with two 12V and two 5V outputs. (e) Iridium satellite modem. (f) Q330S.

7.2.3 Service Life

We expect the Q330S to have significant service life due to its rugged design and proven use. After each season, we would need to perform laboratory tests to ensure that the data logger is still functioning properly, and after 5 years send it to the manufacturer for service. With proper maintenance and service, we might expect the Q330S to last up to 10 years.

The fitPC comes with a 3-year manufacturer warranty. Similar to the data logger, we would want to inspect and test the computer after each season to ensure that all systems are functioning properly. Due to being out in the elements, we would want to thoroughly inspect the computer after 3 years to ensure that the hard drive and computer hardware are functioning properly. With proper maintenance and service, we would expect the computer to last approximately 5 years. At that point, the computer will most likely be obsolete and an upgrade to a newer and faster computer would greatly enhance the detection.

The ECM infrasound sensors are expected to have a service life of about 2 years. We have deployed ECMs for two winters with no major problems and have only needed to replace 2 sensors. Since the sensors are very inexpensive, if there is any sign that the signal is not perfect, the sensor can be replaced.

7.3   Software Development

7.3.1   On-site Control

A Graphical User Interface (GUI) controls the two major processes on the fitPC, communication with the Q330S and data processing (Figure 7.6). When the computer is initially powered up either through startup, rebooting, or connecting power, the RunNetmon GUI initializes. When RunNetmon starts, it checks whether a connection with the Q330S has been established. If the connection is not present, RunNetmon will start communication and if communication has already been established, Run-Netmon will not try to restart the connection (Section 7.3.2). After the connection with the Q330S is detected or started, RunNetmon will start the data processing
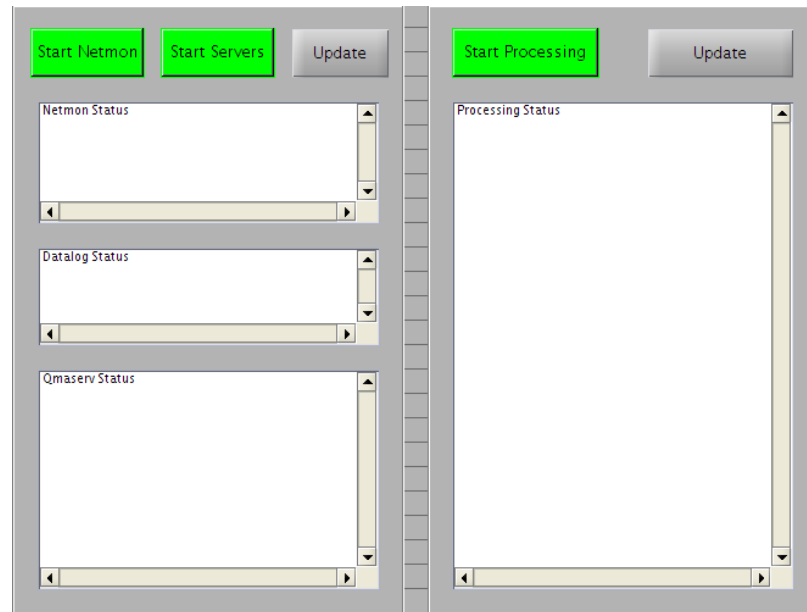
Figure 7.6: GUI on-site that controls the Q330S communication and processing. The left panel buttons control starting and stopping of netmon, qmaserv, and datalog (through netmon). The left panel update button will update the status for netmon, datalog, and qmaserv from the log files. The right panel controls the processing flow and the update button will update the status of the processing from the log file.

scripts (Section 7.3.3). The processing flow is shown in Figure 7.7 and will be covered in detail below.

The RunNetmon GUI allows a user to visit the site and easily control the major aspects of the avalanche detection system. When connected to the fitPC, the user will see the RunNetmon GUI (Figure 7.6). The left panel controls netmon (Section 7.3.2), which controls the communication server (qmaserv) and data logging program (datalog). The left button controls the start/stop of netmon, which will also start/stop qmaserv and datalog. The middle button controls the start/stop of communication and data logging but leaves netmon running. The right button updates the status obtained from the netmon, qmaserv, and datalog log files.

The right panel controls the data processing (Section 7.3.3). The left button

controls the start/stop of the processing and is useful when visiting the site. The processing algorithm will put the fitPC to sleep and this button allows the user to stop processing for servicing. The right button updates the processing status from the log file.

RunNetmon is a simple GUI with limited functionality, making it a robust method of controlling the communications and processing. If for some reason RunNetmon should fail, a script will restart RunNetmon automatically, which ensures that the communications and data processing are always running.
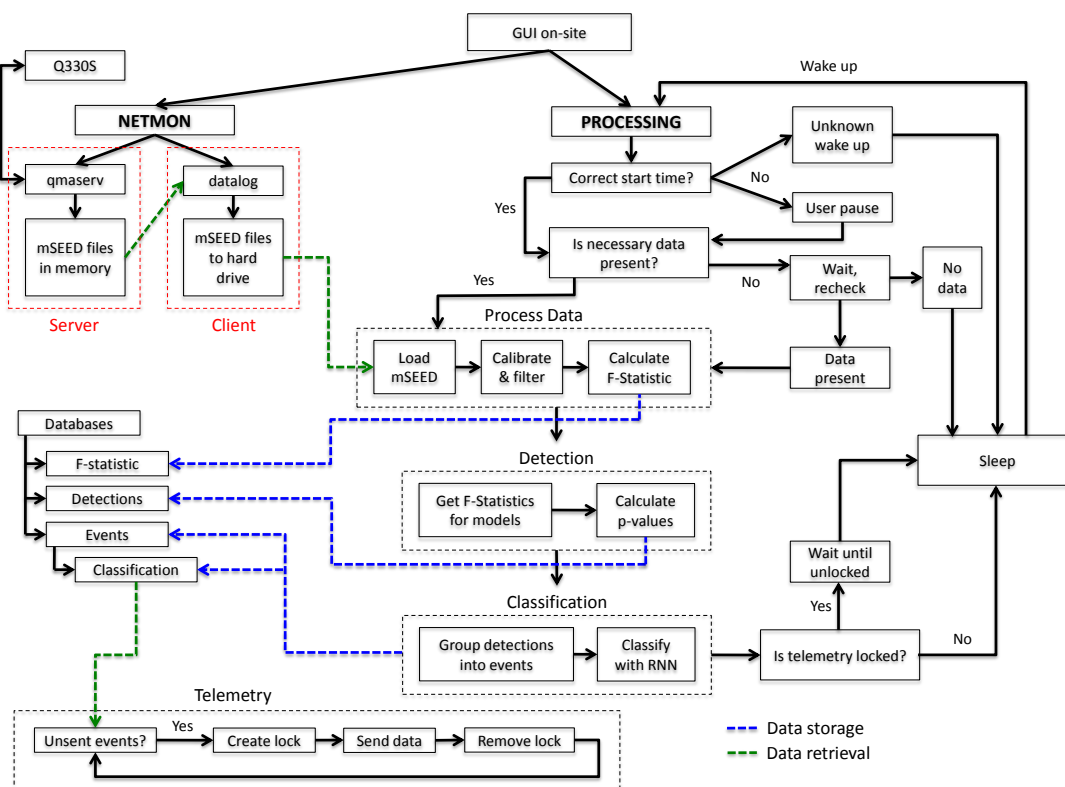
Figure 7.7: Flow chart for the the on-site data retrieval and processing.

7.3.2   Q330S and fitPC Communication

Communication between the Q330S and fitPC is through Comserv software bundle, maintained by ISTI (www.isti.com), UC Berkley, and Quanterra. The library was developed to communicate with Quanterra digitizers in a Windows or Linux environment. Mountain Air (qmaserv) was developed to utilize the advanced IP communication ability of the Q330S. The software bundle consists of the communication server (qmaserv), a set of clients that communicate with qmaserv, and netmon, which controls the startup and shutdown of multiple servers and clients.

qmaserv

The communications server qmaserv controls communication between the fitPC and Q330S through an ethernet cable (Figure 7.7, Server). qmaserv generates miniSEED (Standard for the Exchange of Earthquake Data) packets to provide data and related information from the Q330S to the clients. The data packets are stored in memory for the client programs to read. Each station requires a dedicated qmaserv server and multiple servers can run on a single computer.

datalog

datalog is a client that receives miniSEED data packets from a single qmaserv server and records the data to disk (Figure 7.7, Client). datalog has been configured to only write the miniSEED packets from the five infrasound and one geophone channels. This ensures that only the necessary data is written to disk and reduces unwanted communication between datalog and qmaserv for fast real time application.

netmon

netmon is a management program used to control the startup, shutdown, and restart of the communication servers and clients for multiple stations (Figure 7.7, NETMON). netmon can be used to manually check the status, perform startup, or shutdown operations for a station. For continuous operation, netmon is run in background mode and automatically monitors the status and restart of servers and clients if one were to stop.

7.3.3   Processing Flow

The following section outlines the data processing occurring in near real time on the fitPC. The processing algorithms have been developed by Boise State University for the purpose of avalanche detection using infrasound.

Database Creation

A SQLite database (www.sqlite.org) is an SQL database engine that excels at accessing a local database on the hard drive. A database can contain multiple tables that have columns (fields) representing a variable and rows (records) that represent the data to be stored. Data is inserted into or accessed from a table using SQL commands.

The avalanche detection system uses a database that contains three tables: Fisher statistic data (Table 7.4), detection data (Table 7.5), and events (Table 7.6). The database stores and provides data during processing depending on the current processing step (Figure 7.7, Database). Using a database like SQLite makes the processing more efficient by only retrieving data that is necessary for the current step instead of

loading a large data file that contains more data than needed.

Signal Processing

The main function of the on-site processing is to reduce the amount of data to transfer. Since this requires a small computer to be continually acquiring data from the data logger and computation expense of data processing, power consumption becomes a primary concern. To enhance the power efficiency of the computer, we put the computer to sleep after processing and telemetry are completed. At a pre-determined time, the computer will wake, begin processing, and go back to sleep. The processing flow follows the flow chart in Figure 7.7 (PROCESSING) with processing parameters defined in a configuration file (Table 7.3).

The processing window length (in seconds) is defined in the processing configuration file. The processing window defines the start and end time for data processing and controls when the computer awakes. When the computer awakes, it checks whether or not the current time is close to the defined start time. A large difference could be caused by either an unknown source or a user logging into the computer. If it is an unknown source, the computer will go back to sleep. If a user desires to log into the computer, the processing will pause until the user resumes data processing.

After the start time has been determined, the processing checks to see if all the necessary infrasound data is available. An algorithm checks to see if any miniSeed files from datalog match the start and end time of the processing window. The algorithm will attempt to read the data for a given number of tries defined in the configuration file. This allows the most current data from Q330S to be retrieved and written to disk. If no data is present after all the tries, the computer will be put to sleep.

Table 7.3: Processing parameters defined in the configuration file with default values and variable descriptions.

Variable	Value	Description
WindowLength	600.0 seconds	Processing window length
MaxWindowLength	3.0 hours	Number of hours back to look for miniSEED files
TimeOffset	10.0 minutes	Offset back from current time to end processing window
master_node	1	Channel to base time shifts off for Fisher statistic
c	320.0 m/s	Speed of sound
num_nodes	31	Number of grid nodes to divide slowness space in one dimension
nfft	2048	Number of points to perform the Fast Fourier Transform for Power Bands
WindowSize	6 seconds	Length of window to calculate Fisher statistic
WindowOverlap	3 seconds	Length of overlap between windows
Channels	1 2 3 4 5	Channels to use
sampleRate	100 Hz	Sample rate of Q330S
Freq1	2 4 Hz	Frequency band for processing
Freq2	4 6 Hz	Frequency band for processing
Freq3	6 8 Hz	Frequency band for processing
Freq4	8 10 Hz	Frequency band for processing
Freq5	10 12 Hz	Frequency band for processing
Freq6	12 14 Hz	Frequency band for processing
Freq7	14 16 Hz	Frequency band for processing
Freq8	16 18 Hz	Frequency band for processing
Freq9	18 20 Hz	Frequency band for processing
FreqB	2 20 Hz	Broadband for Neural Network processing
Power1	1.0 5.0 Hz	Frequency range to calculate power
Power2	5.0 10.0 Hz	Frequency range to calculate power
Power3	10.0 15.0 Hz	Frequency range to calculate power
Power4	15.0 20.0 Hz	Frequency range to calculate power
Power5	20.0 50.0 Hz	Frequency range to calculate power
EventBuffer	5	Number of windows to buffer the front and back for event database
WindowBack	900 seconds	Non-parametric window length
alpha	10^{-10}	Significance level for event detection
NumberofTries	8	Number of tries to check if data has been loaded
EventThresh	0.5	Neural network output threshold for event classification

Table 7.4: The Fisher statistic data from processing are stored in the Fdata table with the given fields and definitions.

Field	Description
date	Date and time of window
F	2-20Hz Fisher statistic value for Neural Network
BA	2-20Hz Back azimuth to the potential source location for Neural Network
V	2-20Hz Apparent velocity to the potential source location for Neural Network
F1-F9	Fisher statistic for multiple frequency bands
BA1-BA9	Back azimuth for multiple frequency bands
V1-V9	Apparent velocity for multiple frequency bands
Power1	Power in the 1-5 Hz frequency band
Power2	Power in the 5-10 Hz frequency band
Power3	Power in the 10-15 Hz frequency band
Power4	Power in the 15-20 Hz frequency band
Power5	Power in the 20-50 Hz frequency band
Slowness_X	Slowness vector, x component
Slowness_Y	Slowness vector, y component
Slowness_Z	Slowness vector, z component

Once the necessary data is present, data processing can begin (Figure 7.7, Process Data). The infrasound data between the start and end time is loaded, calibrated, and filtered to the desired bandwidths defined in the configuration file. The Fisher statistic (e.g., *Blandford*, 1974, Chapter 5) is calculated for the processing window. For each window, the maximum Fisher statistic, with the corresponding back azimuth, apparent velocity, and slowness vector are saved to the Fdata table in the database (Table 7.4). The power in the frequency domain for five different frequency ranges are also calculated for classification and stored.

Table 7.5: The non-parametric event detection results are stored in the Detection table with the given fields and definitions.

Field	Description
date	Date and time of window
pvalue	P-value of the window
h	If pvalue was less than alpha

Event Detection

After the Fisher statistic is calculated within the processing window, event detection is performed (Figure 7.7, Detection). Detection requires a large amount of data to make up the background models (Chapter 5) and prior Fisher statistic data is loaded from the database. The p-values are calculated for each time window and are stored in the Detection table of the database (Table 7.5).

Event Grouping

Event detection only determines if a single processing window is an event and does not group into larger events. Therefore, the next step is to group the single events into larger groups for classification (Figure 7.7, Classification). The single events are grouped based on how similar the back azimuth and apparent velocity are of two close single detections. If the two single event properties are similar and are reasonably close in time, then they will be grouped together. A new event will occur when the back azimuth and apparent velocity are significantly different or there is a large time gap between two single events. Once the single events have been grouped, the new large event is stored in the database (Table 7.6).

For the classification, padding must be added to the event. Therefore, the EventStart and Duration of the actual event are stored separately from the StartTime and End-

Time of the window around the event. The event properties are a string of comma separated values that allow time series data to be stored in the database. Each event gets a unique ID for identification.

Event Classification

Event classification is achieved using a neural network that uses the events stored in Table 7.6. The neural network classifies either avalanche or no avalanche, which is stored in the database.

When an avalanche is detected, a small text file is created. The file contains important fields from the Events table (Table 7.6) like the StartTime, EndTime, EventStart, Duration, Classification, Backazimuth, v_app, and F. The file is saved with a time stamp as the file name that is used by the telemetry process to determine new events.

7.3.4 Telemetry

The telemetry is a separate process that runs in parallel to the signal processing and event detection (Figure 7.7, Telemetry). The telemetry process looks for the most recent event text files that have not been sent. When a file needs to be sent, the process locks the computer from going to sleep while the file is sent to the Iridium modem. Once the messages have been sent, the lock file is removed and the computer may go to sleep.

Once the file is sent, it is routed to a server waiting for the message. The raw message is inserted into a database table on the server without any processing. Once the raw message is in the table, the message content can be parsed into the fields that

Table 7.6: The event data are stored in the Events table with the given fields and definitions.

Field	Description
ID	Integer ID for each event, auto increments
StartTime	Start time of the event window
EndTime	End time of the event window
EventStart	Estimated start time of the event
Duration	Duration in seconds of the event
Classification	Classification of the event
Sent	Whether or not the event has been classified/sent
Backazimuth	Back azimuth for entire event, string with values separated by commas
v_app	Apparent velocity for entire event, string with values separated by commas
F	Fisher statistic for entire event, string with values separated by commas
pvalue	P-value for entire event, string with values separated by commas
Power1	Power1 for entire event, string with values separated by commas
Power2	Power2 for entire event, string with values separated by commas
Power3	Power3 for entire event, string with values separated by commas
Power4	Power4 for entire event, string with values separated by commas
Power5	Power5 for entire event, string with values separated by commas

were sent, making it easier to view the data on the web application.

7.4   Installation Budget

The following outlines an estimated budget for the installation of the infrasound array (Table 7.7). The budget includes all the hardware costs, personnel costs for installation, and personnel costs for maintenance during the first year.

Table 7.7: Array hardware and installation budget.

Item	Qty.	Price	Amount
Array			
Quanterra Q330S 6-ch	1	$ 13,000.00	$ 13,000.00
Electronics enclosure	1	$ 500.00	$ 500.00
Infrasound sensor	5	$ 20.00	$ 100.00
Geophone 4.5Hz short period	1	$ 150.00	$ 150.00
Infrasound cable (500' roll)	1	$ 300.00	$ 300.00
Cable conduit (500' roll)	1	$ 600.00	$ 600.00
Sensor poles	5	$ 50.00	$ 250.00
Sensor housing	5	$ 50.00	$ 250.00
		Subtotal	**$ 15,150.00**
Power System at Array			
Tower	1	$ 5,000.00	$ 5,000.00
Solar panels (80W)	3	$ 300.00	$ 900.00
Charge controller	1	$ 300.00	$ 300.00
Deep cycle battery (50-85 A hr)	4	$ 300.00	$ 1,200.00
Electrical safety equipment	1	$ 200.00	$ 200.00
Mounting equipment	1	$ 1,000.00	$ 1,000.00
Conduit	1	$ 300.00	$ 300.00
Sunwize E4-500 4 Battery Enclosure	1	$ 450.00	$ 450.00
Cables	1	$ 300.00	$ 300.00
		Subtotal	**$ 9,650.00**
Communications			
Iridium 9603-U from JouBeh Technologies	1	$ 325.00	$ 325.00
Activation fee	1	$ 40.00	$ 40.00
Monthly subscription fee		$ 16.00	
Data charge per Kbyte		$ 1.40	
		Subtotal	**$ 365.00**
Signal Processing			
FitPC 2i running Xubuntu	1	$ 500.00	$ 500.00
Backup hard drive (minimum 1TB)	1	$ 200.00	$ 200.00

Table 7.7 – *Continued from previous page*

Item	Qty.	Price	Amount
		Subtotal	**$ 700.00**
Installation Costs			
Travel to and from site	1	$ 3,000.00	$ 3,000.00
Additional labor	20	$ 150.00	$ 3,000.00
		Subtotal	**$ 6,000.00**
Maintenance and Running Costs			
Maintaining site for year 1	1	$ 10,000.00	$ 10,000.00
Maintaining processing and databases	1	$ 10,000.00	$ 10,000.00
Tuning NN to new events	1	$ 10,000.00	$ 10,000.00
		Subtotal	**$ 30,000.00**
Array			**$ 15,150.00**
Power System			**$ 9,650.00**
Communications			**$ 365.00**
Signal Processing			**$ 700.00**
Installation			**$ 6,000.00**
Maintenance and Running			**$ 30,000.00**
Miscellaneous Expenses			**$ 5,000.00**
Total			**$ 66,865.00**

7.5   Discussion and Conclusion

On August 8, 2014, the prototype version of the real time infrasound detection system was installed at the 100.5 array. The neural network was trained to detect vehicles, a much easier task in the summer. During testing, the system detected approximately 146 events between August 8th 20:30 UTC and August 9th 08:15 UTC.

The system sent out 16 messages with information about the vehicle detections. The events could be viewed on a simple webpage.

The test has been successful in processing the data in real time, detecting events, correctly classifying vehicles, and relaying the information over an Iridium satellite modem. However, the test came to an end with a bug in the code that shut down the processing steps. The test brought to light areas to improve the system prior to operational deployment.

Using a computer on-site allows the system to be deployed in remote locations where reliable access to data transmission is complicated. Since all data processing, event detection, and event classification are performed on-site, a satellite Iridium modem can be used to telemeter small text files about the relevant event detections. This makes a robust system that can be deployed anywhere and telemeter back relevant avalanche information.

In the future, we hope to take advantage of the computer on-site. The cost of the infrasound array could further be reduced by using a low cost data acquisition device to replace the Q330S, since these devices must be connected to a computer. This would further allow experimentation with deploying a higher number of sensors (upwards of 32 sensors) as all the raw data does not need to be transmitted but processed on-site.

To cover the majority of the Highway 21 corridor, a minimum of 4 arrays would be needed. Further testing of multi-array processing and data transfer on-site would produce a unique problem of inter-array communication, as the arrays would need to "share" the data with other arrays to pinpoint the potential source location.

CHAPTER 8:

CONCLUSION

Three major factors influence avalanche formation: snowpack, weather, and terrain. The factors are further complicated due to a high spatial variability of the snowpack, making it difficult to evaluate. My work focused on the validation of the snow slope stability (SNOSS) model using information from the SMP about the microstructure of the snowpack at a point and further validating the model using avalanche times recorded on infrasound arrays.

Chapter 1 brought to our attention the need to understand avalanches as they have the ability to affect a broad spectrum of users and cause significant economic impact. However, avalanches are difficult to predict but can be understood through the use of snowpack models, new snowpack measurement techniques, and recording avalanches with infrasound.

Chapter 2 introduced the snow slope stability (SNOSS) model that can be used to forecast for direct action avalanches. SNOSS was adapted to run in near real time using weather data from nearby weather stations along Highway 21 and 12 in Idaho. Working with the ITD avalanche forecasters, I produced 3 different figures to present the results in a concise and simple manner. The final product was an interactive chart to plot the minimum stability index value and the depth from the surface to the minimum for the current time step. SNOSS results from a large avalanche cycle in January 2012 were compared to 2 avalanches recorded on a nearby infrasound array. Further improvement of the model will require a large catalog of avalanche times,

which is still under development using the infrasound arrays.

Chapter 3 used weather data and SNOSS results to forecast the probability of an avalanche occurring given the current conditions. The study was performed with a large dataset of weather and avalanche observations from 2001-2010 in Little Cottonwood Canyon, UT. SNOSS forecasts for direct action avalanches that occur naturally during large storms, and with that criteria, 42 avalanche days and 358 non-avalanche days were found in the avalanche dataset. To predict an avalanche day, 88 meteorological and 20 SNOSS inputs variables were used with balanced random forests. Results showed a low overall correct classification rate between 0.57 and 0.67 depending on the combination of weather and SNOSS variables with SNOSS variables having lower correct classification rates. There were four variables that were important for three out of the four tests: PeakTempMax48, SnowDriftMin48, snossSI48, and snossSTRENGTH12.

To understand the snowpack microstructure at a point, Chapter 4 used the SMP signal to classify the snow grain types. The grain types from a manual snowpit were classified with a random forest using the microstructural and micromechanial properties inverted from the SMP signal. The overall error rate for classifying new snow, rounds, and facets was 17.8% and 27.8% for the Colorado and Switzerland data, respectively. The important variables used to differentiate between grain types were those properties that contained information about grain type, i.e. N_T, σ_{micro}, N_m, and L_n.

Calibration of SNOSS with avalanche times requires a significant catalog of avalanche events. Chapter 5 provides background information on infrasound generation from avalanches, current array processing techniques, non-parametric event detection, and

event classification. This work introduced a method of event detection using the Fisher statistic values for when the background values are constantly changing. With non-parametric event detection, I was able to continually adapt to the changes in the background noise, automatically detecting coherent events, and reduce the number of false detections. Finally, the chapter provided a brief overview of the artificial neural network used to classify detected events.

Besides detection, infrasound can be used to estimate the velocity of an avalanche (Chapter 6). The possible source locations of the avalanche could be estimated along the avalanche path profile. From the locations, an estimate of the velocity and the uncertainty was calculated using a Monte Carlo sampling approach, with an achieved maximum velocity of $35.9 \pm 7.6 ms^{-1}$. Three different phases to the avalanche were determined, first with a small signal from the snowpack failure, followed by the avalanche gaining momentum, and finally the avalanche reaching the highway.

The infrasound processing described in Chapter 5 was developed into a real time avalanche detection system outlined in Chapter 7. A description of the hardware and software developed for avalanche detection were presented. The prototype real time detection system was successfully deployed in the summer and could detect, classify, and telemeter events of interest.

REFERENCES

Anderson, D. L., and C. S. Benson (1963), Densification and diagenesis of snow, *Ice and Snow (W.D. Kingery, ed), M.I.T. Press*, pp. 391–411.

Arechiga, R. O., J. B. Johnson, H. E. Edens, R. J. Rison, and W. Rison (2011), Acoustic localization of triggered lightning, *JOURNAL OF GEOPHYSICAL RESEARCH-ATMOSPHERES*, *116*, doi:{10.1029/2010JD015248}.

Arrowsmith, S. J., R. Whitaker, S. R. Taylor, R. Burlacu, B. Stump, M. Hedlin, G. Randall, C. H., and D. ReVelle (2008), Regional monitoring of infrasound events using multiple arrays: application to Utah and Washington State, *GEOPHYSICAL JOURNAL INTERNATIONAL*, *175*(1), 291–300, doi:{10.1111/j.1365-246X.2008.03912.x}.

Azar, A. E., H. Ghedira, P. Romanov, S. Mahani, M. Tedesco, and R. Khanbilvardi (2008), Application of satellite microwave images in estimating snow water equivalent, *Journal of the American Water Resources Association*, *44*(6), 1347–1362.

Baenninger, D., C. S. Bourgeois, M. Matzl, and M. Schneebeli (2008), Reflectance modeling for real snow structures using a beam tracing model, *SENSORS*, *8*(5), 3482–3496, doi:{10.3390/s8053482}.

Bair, E. H., R. Simenhois, K. Birkeland, and J. Dozier (2012), A field study on failure of storm snow slab avalanches, *COLD REGIONS SCIENCE AND TECHNOLOGY*, *79-80*, 20–28, doi:{10.1016/j.coldregions.2012.02.007}.

Bartelt, P., and M. Lehning (2002), A physical snowpack model for the swiss avalanche warning; part i: numerical model, *Cold Reg. Sci. and Tech.*, *35*(3), 123–145.

Bedard Jr., A. J. (1989), Detection of avalanches using atmospheric infrasound, in *Proceedings ofWestern Snow Conference, Fort Collins, CO*, pp. 52–58.

Bedard Jr., A. J. (1994), An evaluation of atmospheric infrasound for monitoring avalanche, in *Proceedings of 7th International Symposium on Acoustic Sensing and Associated Techniques of the Atmosphere and Oceans, Boulder, CO*.

Bedard Jr., A. J., G. E. Greene, J. Intrieri, and R. Rodriguez (1988), On the feasibility and value of detecting and characterizing avalanches remotely by monitoring radiated sub-audible atmospheric sound at long distances, in *Proceedings of A Multidisciplinary Approach to Snow Engineering, Santa Barbara, CA*, pp. 267–275.

Bellaire, S., and J. Schweizer (2011), Measuring spatial variations of weak layer and slab properties with regard to snow slope stability, *COLD REGIONS SCIENCE AND TECHNOLOGY*, *65*(2), 234–241, doi:{10.1016/j.coldregions.2010.08.013}.

Bellaire, S., C. Pielmeier, M. Schneebeli, and J. Schweizer (2009), Stability algorithm for snow micro-penetrometer measurements, *JOURNAL OF GLACIOLOGY*, *55*(193), 805–813.

Bessason, B., G. Eiriksson, O. Thorarinsson, A. Thorarinsson, and S. Einarsson (2007), Automatic detection of avalanches and debris flows by seismic methods, *JOURNAL OF GLACIOLOGY*, *53*(182), 461–472, doi:{10.3189/002214307783258468}.

Blandford, R. R. (1974), An automatic event detector at the tonto forest seismic observatory, *Geophysics*, *39*(5), 633–643.

Brachet, N., and J. Coyne (2006), The current status of infrasound data processing at the international data center, *28th Seismic Research Review: Ground-Based Nuclear Explosion Monitoring Technologies*, pp. 873–881.

Breiman, L. (1996), Bagging predictors, *MACHINE LEARNING*, *24*(2), 123–140, doi:{10.1007/BF00058655}.

Breiman, L. (2001), Random forests, *MACHINE LEARNING*, *45*(1), 5–32, doi:{10.1023/A:1010933404324}.

Brenning, A. (2009), Benchmarking classifiers to optimally integrate terrain analysis and multispectral remote sensing in automatic rock glacier detection, *REMOTE SENSING OF ENVIRONMENT*, *113*(1), 239–247, doi:{10.1016/j.rse.2008.09.005}.

Cansi, Y. (1995), An Automatic Seismic Event Procesing for Detection and Location - the P.M.C.C. Method, *Geophysical Research Letters*, *22*(9), 1021–1024, doi:{10.1029/95GL00468}.

Caplan-Auerbach, J., S. Prejean, and J. Power (2004), Seismic recordings of ice and debris avalanches on iliamna volcano (alaska), *Acta Vulcanologica, 16 (1-2)*, 9–20.

Chen, C., A. Liaw, and L. Breiman (2004), Using random forest to learn unbalanced data, *Tech. rep.*, University of California at Berkeley.

Chritin, V., M. Rossi, and R. Bolognesi (1996), Acoustic detection system for operational avalanche forecasting, in *Proceedings of the 1996 International Snow Science Workshop, Banff, Canada*, pp. 129–133.

Comey, R., and T. Mendenhall (2004), Recent studies using infrasound sensors to remotely monitor avalanche activity, in *Proceedings of the 2004 International Snow Science Workshop, Jackson Hole, Wyoming*.

Conway, H., and C. Wilbour (1999), Evolution of snow slope stability during storms, *Cold Reg. Sci. and Tech.*, *30*, 67–77.

Cordy, P., D. M. McClung, C. J. Hawkins, J. Tweedy, and T. Weick (2009), Computer assisted avalanche prediction using electronic weather sensor data, *COLD REGIONS SCIENCE AND TECHNOLOGY*, *59*(2-3), 227–233, doi:{10.1016/j.coldregions.2009.07.006}, International Snow Science Workshop, Whistler, CANADA, SEP 21-27, 2008.

Davis, R., K. Elder, D. Howlett, and E. Bouzaglou (1999), Relating storm and weather factors to dry slab avalanche activity at Alta, Utah, and Mammoth Mountain, California, using classification and regression trees, *COLD REGIONS SCIENCE AND TECHNOLOGY*, *30*(1-3), 79–89, doi:{10.1016/S0165-232X(99)00032-4}, International Snow Science Workshop, SUNRIVER, OREGON, SEP 27-OCT 01, 1998.

Douglas, A. (2002), *Handbook of Earthquake and Engineering Seismology*, chap. Seismometer arrays-Their use in earthquake and test ban seismology, pp. 357–367, Academic.

Durand, M., E. J. Kim, and S. A. Margulis (2008), Quantifying uncertainty in modeling snow microwave radiance for a mountain snowpack at the point-scale, including stratigraphic effects, *IEEE TRANSACTIONS ON GEOSCIENCE AND REMOTE SENSING*, *46*(6), 1753–1767, doi:{10.1109/TGRS.2008.916221}.

Durand, Y., G. Giraud, E. Brun, L. Merindol, and E. Martin (1999), A computer-based system simulating snowpack structures as a tool for regional avalanche forecasting, *JOURNAL OF GLACIOLOGY*, *45*(151), 469–484.

Eckerstorfer, M., and H. H. Christiansen (2011), Relating meteorological variables to the natural slab avalanche regime in High Arctic Svalbard, *COLD REGIONS SCIENCE AND TECHNOLOGY*, *69*(2-3, SI), 184–193, doi:{10.1016/j.coldregions.2011.08.008}.

Elgammal, A., R. Duraiswami, D. Harwood, and L. Davis (2002), Background and foreground modeling using nonparametric kernel density estimation for visual surveillance, *Proceeedings of the IEEE*, doi:10.1109/jproc.2002.801448.

Elman, J. L. (1990), Finding structure in time, *COGNITIVE SCIENCE*, *14*(2), 179–211.

Fierz, C., R. Armstrong, Y. Durand, P. Etchevers, E. Greene, and D. McClung (2009), The international classification for seasonal snow on the ground, *IHP-VII Technical Documents in Hydrology N°83, IACS Contribution N°1, UNESCO-IHP*.

Floyer, J., and D. McClung (2003), Numerical avalanche prediction: Bear Pass, British Columbia, Canada, *COLD REGIONS SCIENCE AND TECHNOLOGY*, *37*(3), 333–342, doi:{10.1016/S0165-232X(03)00074-0}, International Snow Science Workshop, PENTIC-TON, CANADA, SEP 29-OCT 04, 2002.

Fohn, P. M. B. (1987), The stability index and various triggering mechanisms, in *Avalanche Movement and Effects. Proc., Davos Symposium*, 162, pp. 195–214, Int. Ass. Hydrol. Sci.

Gislason, P., J. Benediktsson, and J. Sveinsson (2006), Random Forests for land cover classification, *PATTERN RECOGNITION LETTERS*, *27*(4), 294–300, doi:{10.1016/j.patrec.2005.08.011}, 3rd Pattern Recognition in Remote Sensing Workshop, Kingston Univ, Kingston Upon Thames, ENGLAND, AUG 27, 2004.

Gubler, H., and M. Hiller (1984), The use of microwave FMCW radar in snow and avalanche research, *Cold Reg. Sci. and Tech.*, *9*, 109–119.

Havens, S., H.-P. Marshall, N. Steiner, and M. Tedesco (2010), Snow micro penetrometer and near infrared photography for grain type classification, *Proceedings of the International Snow Science Workshop, Squaw Valley, CA*.

Havens, S., H.-P. Marshall, J. B. Johnson, and B. Nicholson (2014), Calculating the velocity of a fast moving snow avalanche using an infrasound array, *Geophysical Research Letters*, *41*, doi:10.1002/2014GL061254.

Havens, S., H.-P. Marshall, G. Trisca, and J. Johnson (In Prep), Rp219 - real time avalanche detection for high risk areas, *Tech. rep.*, Boise State University for Idaho Transportation Department.

Havens, S., H.-P. Marshall, C. Pielmeier, and K. Elder (2013), Automatic Grain Type Classification of Snow Micro Penetrometer Signals With Random Forests, *IEEE TRANSACTIONS ON GEOSCIENCE AND REMOTE SENSING*, *51*(6, 1), 3328–3335, doi: {10.1109/TGRS.2012.2220549}.

Hendrikx, J., I. Owens, W. Carran, and A. Carran (2005), Avalanche activity in an extreme maritime climate: The application of classification trees for forecasting, *COLD REGIONS SCIENCE AND TECHNOLOGY*, *43*(1-2, SI), 104–116, doi:{10.1016/j.coldregions.2005.05.006}, 1st General Meeting of the European-Geosciences-Union, Nice, FRANCE, APR 25, 2004.

Horel, J., et al. (2002), Mesowest: Cooperative mesonets in the western united states, *Bull. Amer. Meteor. Soc.*, *83*(2), 211–225, doi:10.1175/1520-0477(2002)083⟨0211:MCMITW⟩2.3.CO;2.

Huggel, C., J. Caplan-Auerbach, C. F. Waythomas, and R. L. Wessels (2007), Monitoring and modeling ice-rock avalanches from ice-capped volcanoes: A case study of frequent large avalanches on Iliamna Volcano, Alaska, *JOURNAL OF VOLCANOLOGY AND GEOTHERMAL RESEARCH*, *168*(1-4), 114–136, doi:{10.1016/j.jvolgeores.2007.09.009}.

Ivanov, B., G. Xu, and T. Buell (2008), Storm related closures of i-5 and i-90: Freight transportation economic impact assessment report, *Tech. rep.*, Washington State Department of Transportation.

Jain, P., and J. D. Hirst (2010), Automatic structure classification of small proteins using random forest, *BMC BIOINFORMATICS*, *11*, doi:{10.1186/1471-2105-11-364}.

Jamieson, B., and C. Johnston (2001), Evaluation of the shear frame test for weak snowpack layers, *ANNALS OF GLACIOLOGY*, *32*, 59–69, doi:{10.3189/172756401781819472}, International Symposium on Snow, Avalanches and Impact of the Forest Cover, INNSBRUCK, AUSTRIA, MAY 22-26, 2000.

Jamieson, J. B. (1995), Avalanche prediction for persistent snow slabs, Ph.D. thesis, Dept. Civil Eng., Univ. Calgary, Alberta, Canada, 258pp.

Johnson, B., J. Jamieson, and R. Stewart (2004), Seismic measurement of fracture speed in a weak snowpack layer, *COLD REGIONS SCIENCE AND TECHNOLOGY*, *40*(1-2), 41–45, doi:{10.1016/j.coldregions.2004.05.003}.

Johnson, J. (2004), Source location variability and volcanic vent mapping with a small-aperture infrasound array at Stromboli Volcano, Italy, *BULLETIN OF VOLCANOLOGY*, *67*(1), 1–14, doi:{10.1007/s00445-004-0356-8}.

Johnson, J., R. Aster, M. Ruiz, S. Malone, P. McChesney, J. Lees, and P. Kyle (2003), Interpretation and utility of infrasonic records from erupting volcanoes, *Journal of Volcanology and Geothermal Research*, *121*(12), 15 – 63, doi:http://dx.doi.org/10.1016/S0377-0273(02)00409-2.

Johnson, J. B., and M. Schneebeli (1999), Characterizing the microstructural and micromechanical properties of snow, *Cold Regions Science and Technology*, *30*, 91–100.

Karason, H., and R. D. van der Hilst (2001), Tomographic imaging of the lowermost mantle with differential times of refracted and diffracted core phases (pkp, pdiff), *Journal of Geophysical Research: Solid Earth*, *106*(B4), 6569–6587.

Kellam, J. K. (2012), The urban avalanche interface and community impacts a case study: Ketchum, sun valley, and the wood river valley, idaho, in *Proceedings, International Snow Science Workshop, Anchorage, Alaska.*

Kishimura, K., and K. Izumi (1997), Seismic signals induced by snow avalanche flow, *NATURAL HAZARDS, 15*(1), 89–100, doi:{10.1023/A:1007934815584}.

Kogelnig, A., E. Surinach, I. Vilajosana, J. Huebl, B. Sovilla, M. Hiller, and F. Dufour (2011), On the complementariness of infrasound and seismic sensors for monitoring snow avalanches, *NATURAL HAZARDS AND EARTH SYSTEM SCIENCES, 11*(8), 2355–2370, doi:{10.5194/nhess-11-2355-2011}.

Kojima, K. (1967), Densification of seasonal snowcover, in *Physics of Snow and Ice, Proc. Int. Conf. on Low Temp. Sci.*, vol. 1, edited by H. Oura, pp. 929–952, Hokkaido Univ., Sapporo.

Lacroix, P., J. R. Grasso, J. Roulle, G. Giraud, D. Goetz, S. Morin, and A. Helmstetter (2012), Monitoring of snow avalanches using a seismic array: Location, speed estimation, and relationships to meteorological variables, *JOURNAL OF GEOPHYSICAL RESEARCH-EARTH SURFACE, 117*, doi:{10.1029/2011JF002106}.

LeBaron, A. M., D. A. Miller, and A. van Herwijnen (2014), Measurements of the deformation zone around a split-axis snow micropenetrometer tip, *COLD REGIONS SCIENCE AND TECHNOLOGY, 97*, 90–96, doi:{10.1016/j.coldregions.2013.10.008}.

Lehning, M., P. Bartelt, B. Brown, C. Fierz, and P. Satyawali. (2002a), A physical snowpack model for the swiss avalanche warning; part ii. snow microstructure, *Cold Reg. Sci. and Tech., 35*(3), 147–167.

Lehning, M., P. Bartelt, B. Brown, C. Fierz, and P. Satyawali. (2002b), A physical SNOW-PACK model for the Swiss avalanche warning; Part III: meteorological forcing, thin layer formation and evaluation, *Cold Reg. Sci. and Tech.*, *35*(3), 169–184.

Lehning, M., C. Fierz, B. Brown, and B. Jamieson (2004), Modeling snow instability with the snow-cover model SNOWPACK, *38*, 331–338, doi:{10.3189/172756404781815220}, International Symposium on Snow and Avalanches, Davos, SWITZERLAND, JUN 02-06, 2003.

Leprettre, B., J. Navarre, and A. Taillefer (1996), First results from a pre-operational system for automatic detection and recognition of seismic signals associated with avalanches, *JOURNAL OF GLACIOLOGY*, *42*(141), 352–363.

Lutz, E. (2009), Spatial and temporal analysis of snowpack strength and stability and environmental determinants of an inclined, forest opening, Ph.D. thesis, Montana State University.

Maeno, N., N, and T. Ebinumae (1983), Pressure Sintering of Ice and its Implication to the Densification of Snow at Polar Glaciers and Ice Sheets, *Journal of Physical Chemisty*, *87*(21), 4103–4110, doi:{10.1021/j100244a023}.

Marcillo, O., J. B. Johnson, and D. Hart (2012), Implementation, Characterization, and Evaluation of an Inexpensive Low-Power Low-Noise Infrasound Sensor Based on a Micromachined Differential Pressure Transducer and a Mechanical Filter, *JOURNAL OF ATMOSPHERIC AND OCEANIC TECHNOLOGY*, *29*(9), 1275–1284, doi: {10.1175/JTECH-D-11-00101.1}.

Marshall, H.-P. (2009), Inversion source code for snow micro penetrometer.

Marshall, H.-P., and J. B. Johnson (2009), Accurate inversion of high-resolution snow penetrometer signals for microstructural and micromechanical properties, *JOURNAL OF GEOPHYSICAL RESEARCH-EARTH SURFACE*, *114*, doi:10.1029/2009JF001269.

Marshall, H. P., H. Conway, and L. A. Rasmussen (1999), Snow densification during rain, *Cold Reg. Sci. and Tech.*, *30*(1-3), 35–41.

Marshall, H. P., M. Schneebeli, and G. Koh (2007), Snow stratigraphy measurements with high-frequency FMCW radar: comparison with snow micro-penetrometer, *Cold Regions Science and Technology*, *47*, 108–117, special issue: papers from the International Snow Science Workshop 2004.

Marshall, H.-P., C. Pielmeier, and F. Techel (in review), Predicting rutschblock and extended column test stability of primary and secondary failures using multiple snowmicropen measurements and robust classification trees, *Cold Regions Science and Technology*.

Martinez, W. L., and A. R. Martinez (2008), *Computational Statistics Handbook with MATLAB, 2nd Edition*, Cahpman & Hall/CRC.

McClung, D. M., and P. Schaerer (2006), *The Avalanche Handbook*, The Mountaineers, Seattle, WA.

Mears, A. I. (1992), Snow-avalanche hazard analysis for land-use planning and engineering, *Tech. rep.*, Colorado Geological Survey Bulletin 49.

Melton, B. S., and L. F. Bailey (1957), Multiple signal correlators, *Geophysics*, *22*(3), 565–588, doi:10.1190/1.1438390.

Peters, J., B. De Baets, N. E. C. Verhoest, R. Samson, S. Degroeve, P. De Becker, and W. Huybrechts (2007), Random forests as a tool for ecohydrological distribution mod-

elling, *ECOLOGICAL MODELLING*, *207*(2-4), 304–318, doi:{10.1016/j.ecolmodel.2007.05.011}.

Pielmeier, C., and H.-P. Marshall (2009), Rutschblock-scale snowpack stability derived from multiple quality-controlled SnowMicroPen measurements, *COLD REGIONS SCIENCE AND TECHNOLOGY*, *59*(2-3), 178–184, doi:{10.1016/j.coldregions.2009.06.005}, International Snow Science Workshop, Whistler, CANADA, SEP 21-27, 2008.

Pielmeier, C., and M. Schneebeli (2003), Stratigraphy and changes in hardness of snow measured by hand, ramsonde and snow micro penetrometer: a comparison with planar sections, *Cold Regions Science and Technology*, *37*(3), 393–405.

Purves, R., K. Morrison, G. Moss, and D. Wright (2003), Nearest neighbours for avalanche forecasting in Scotland - development, verification and optimisation of a model, *COLD REGIONS SCIENCE AND TECHNOLOGY*, *37*(3), 343–355, doi:{10.1016/S0165-232X(03)00075-2}, International Snow Science Workshop, PENTICTON, CANADA, SEP 29-OCT 04, 2002.

Quinlan, J. R. (1993), *Combing instance-based and model-based learning*, Morgan Kaufmann.

Rees, W. (2006), *Remote sensing of snow and ice*, New York: Taylor and Francis, 285pp.

Ripepe, M., E. Marchetti, and G. Ulivieri (2007), Infrasonic monitoring at stromboli volcano during the 2003 effusive eruption: Insights on the explosive and degassing process of an open conduit system, *Journal of Geophysical Research: Solid Earth*, *112*(B9), doi:10.1029/2006JB004613.

Ripepe, M., S. DeAngelis, G. Lacanna, P. Poggi, C. Williams, E. Marchetti, D. D. Donne,

and G. Ulivieri (2009), Tracking pyroclastic flows at soufrière hills volcano, *EOS, Transactions, American Geophysical Union, 90*, 229–236.

Rost, S., and C. Thomas (2002), Array seismology: Methods and applications, *REVIEWS OF GEOPHYSICS, 40*(3), doi:{10.1029/2000RG000100}.

Rott, H., et al. (2010), Cold Regions Hydrology High-Resolution Observatory for Snow and Cold Land Processes, *PROCEEDINGS OF THE IEEE, 98*(5), 752–765, doi:{10.1109/JPROC.2009.2038947}.

Satyawali, P. K., M. Schneebeli, C. Pielmeier, T. Stucki, and A. K. Singh (2009), Preliminary characterization of Alpine snow using SnowMicroPen, *COLD REGIONS SCIENCE AND TECHNOLOGY, 55*(3), 311–320, doi:{10.1016/j.coldregions.2008.09.003}.

Schirmer, M., J. Schweizer, and M. Lehning (2010), Statistical evaluation of local to regional snowpack stability using simulated snow-cover data, *COLD REGIONS SCIENCE AND TECHNOLOGY, 64*(2, SI), 110–118, doi:{10.1016/j.coldregions.2010.04.012}, International Snow Science Workshop, Davos, SWITZERLAND, SEP 27-OCT 02, 2009.

Schneebeli, M., and J. B. Johnson (1998), A constant-speed penetrometer for high-resolution snow stratigraphy, *Ann. of Glac., 26*, 107–111.

Schweizer, J., J. Jamieson, and M. Schneebeli (2003), Snow avalanche formation, *REVIEWS OF GEOPHYSICS, 41*(4), doi:{10.1029/2002RG000123}.

Schweizer, J., S. Bellaire, C. Fierz, M. Lehning, and C. Pielmeier (2006), Evaluating and improving the stability predictions of the snow cover model SNOWPACK, *COLD REGIONS SCIENCE AND TECHNOLOGY, 46*(1), 52–59, doi:{10.1016/j.coldregions.2006.05.007}.

Scott, E. D., and C. Lance (2002), Infrasonic monitoring of avalanche activity, in *International Snow Science Workshop, Penticton, British Columbia.*

Scott, E. D., C. T. Hayward, R. F. Kubichek, J. C. Hamann, and J. W. Pierre (2004), Results of recent infrasound avalanche monitoring studies, in *Proceedings of the International Snow Science Workshop, Jackson Hole, Wyoming.*

Scott, E. D., C. T. Hayward, R. F. Kubichek, J. C. Hamann, J. W. Pierre, B. Comey, and T. Mendenhall (2007), Single and multiple sensor identification of avalanche-generated infrasound, *COLD REGIONS SCIENCE AND TECHNOLOGY*, *47*(1-2), 159–170, doi:{10.1016/j.coldregions.2006.08.005}, International Snow Science Workshop, Jackson Hole, WY, SEP 19-24, 2004.

Shapiro, L. H., J. B. Johnson, M. Sturm, and G. L. Blaisdell (1997), Snow mechanics: Review of the state of knowledge and applications, *CRREL Technical Report 97-3, 36pp.*

Smart, E., and E. A. Flinn (1971), Fast frequency-wavenumber analysis and fisher signal detection in real-time infrasonic array data processing, *Geophysical Journal International*, *26*(1-4), 279–284, doi:10.1111/j.1365-246X.1971.tb03401.x.

Sturm, M., J. Johnson, and J. Holmgren (2004), Variations in the mechanical properties of arctic and subarctic snow at local (1-m) to regional (100-km) scales, in *Proceedings of the International Symposium on Snow Monitoring and Avalanches (ISSMA-2004)*, Manali, India.

Surinach, E., F. Sabot, G. Furdada, and J. Vilaplana (2000), Study of seismic signals of artificially released snow avalanches for monitoring purposes, *PHYSICS AND CHEMISTRY OF THE EARTH PART B-HYDROLOGY OCEANS AND ATMOSPHERE*, *25*(9), 721–727, doi:{10.1016/S1464-1909(00)00092-7}, General Assembly of the European-Geophysical-Society, THE HAGUE, NETHERLANDS, APR 22, 1999.

Surinach, E., G. Furdada, F. Sabot, B. Biescas, and J. Vilaplana (2001), On the characterization of seismic signals generated by snow avalanches for monitoring purposes, in

ANNALS OF GLACIOLOGY, VOL 32, 2001, *ANNALS OF GLACIOLOGY*, vol. 32, pp. 268–274, doi:{10.3189/172756401781819634}.

Takeuchi, Y., K. Yamanoi, Y. Endo, S. Murakami, and K. Izumi (2003), Velocities for the dry and wet snow avalanches at Makunosawa valley in Myoko, Japan, *COLD RE-GIONS SCIENCE AND TECHNOLOGY*, *37*(3), 483–486, doi:{10.1016/S0165-232X(03) 00086-7}, International Snow Science Workshop, PENTICTON, CANADA, SEP 29-OCT 04, 2002.

Ulivieri, G., E. Marchetti, M. Ripepe, I. Chiambretti, G. De Rosa, and V. Segor (2011), Monitoring snow avalanches in Northwestern Italian Alps using an infrasound array, *COLD REGIONS SCIENCE AND TECHNOLOGY*, *69*(2-3, SI), 177–183, doi:{10.1016/ j.coldregions.2011.09.006}.

Vallet, J., B. Turnbull, S. Joly, and F. Dufour (2004), Observations on powder snow avalanches using videogrammetry, *COLD REGIONS SCIENCE AND TECHNOLOGY*, *39*(2-3), 153–159, doi:{10.1016/j.coldregions.2004.05.004}, Snow and Avalanches Conference, Nice, FRANCE, APR, 2003.

van der Woerd, J., L. Owen, P. Tapponnier, X. Xu, F. Kervyn, R. Finkel, and P. Barnard (2004), Giant, similar to M8 earthquake-triggered ice avalanches in the eastern Kunlun Shan, northern Tibet: Characteristics, nature and dynamics, *GEOLOGICAL SOCIETY OF AMERICA BULLETIN*, *116*(3-4), 394–406, doi:{10.1130/B25317.1}.

van Herwijnen, A., J. Schweizer, and J. Heierli (2010), Measurement of the deformation field associated with fracture propagation in weak snowpack layers, *JOURNAL OF GEO-PHYSICAL RESEARCH-EARTH SURFACE*, *115*, doi:{10.1029/2009JF001515}.

Vilajosana, I., G. Khazaradze, E. Surinach, E. Lied, and K. Kristensen (2007a), Snow avalanche speed determination using seismic methods, *COLD REGIONS SCIENCE AND*

TECHNOLOGY, *49*(1), 2–10, doi:{10.1016/j.coldregions.2006.09.007}, General Assembly of the European-Union-of-Geosciences, Vienna, AUSTRIA, APR 24-29, 2005.

Vilajosana, I., E. Surinach, G. Khazaradze, and P. Gauer (2007b), Snow avalanche energy estimation from seismic signal analysis, *COLD REGIONS SCIENCE AND TECHNOLOGY*, *50*(1-3), 72–85, doi:{10.1016/j.coldregions.2007.03.007}, General Assembly of the European-Geosciences-Union, Vienna, AUSTRIA, APR, 2006.

Vriend, N. M., J. N. McElwaine, B. Sovilla, C. J. Keylock, M. Ash, and P. V. Brennan (2013), High-resolution radar measurements of snow avalanches, *GEOPHYSICAL RESEARCH LETTERS*, *40*(4), 727–731, doi:{10.1002/grl.50134}.

Wojcik, R., K. Andreadis, M. Tedesco, E. Wood, T. Troy, and D. Lettenmeier (2008), Multimodel Estimation of Snow Microwave Emission during CLPX 2003 Using Operational Parameterization of Microphysical Snow Characteristics, *JOURNAL OF HYDROMETEOROLOGY*, *9*(6), 1491–1505, doi:{10.1175/2008JHM909.1}.

Yamasato, H. (1997), Quantitative analysis of pyroclastic flows using infrasonic and seismic data at unzen volcano, japan, *Journal of Physics of the Earth*, *45*, 397–416.

Yount, J., A. Naisbitt, and E. D. Scott (2008), Operational highway avalanche forecasting using the infrasonic avalanche detection system, *International Snow Science Workshop Proceedings, Whistler, BC*, pp. 265–276.

Yueh, S. H., S. J. Dinardo, A. Akgiray, R. West, D. W. Cline, and K. Elder (2009), Airborne Ku-Band Polarimetric Radar Remote Sensing of Terrestrial Snow Cover, *IEEE TRANSACTIONS ON GEOSCIENCE AND REMOTE SENSING*, *47*(10), 3347–3364, doi:{10.1109/TGRS.2009.2022945}.

APPENDIX A:

SNOW MECHANICS AND DENSIFICATION

Snow densification is an important aspect for understanding how the snowpack evolves through time. From the moment a snowflake falls on the surface of the snowpack, it begins a metamorphic process that will continually change its structure. Through different metamorphic processes, the snowflake and the surrounding snow will generally become more dense as time moves on. This chapter will describe the metamorphic processes behind snow densification and how densification can be modeled to provide estimates of snow layer densities. At this point, the focus of my study will be vertical densification of snow under natural loading from the accumulation of new snow layers.

The mechanisms of snow densification rely on how effectively material can be transported at the grain scale to make the snow more dense. *Anderson and Benson* (1963) stated that for densification at the polar regions, there are at least seven different mechanisms of densification and these processes may or may not be mutually exclusive at a given time. In polar regions, the density has a strong dependence on the pressure from the overburden snow (Figure A.1) where densification mechanisms change at three critical densities.
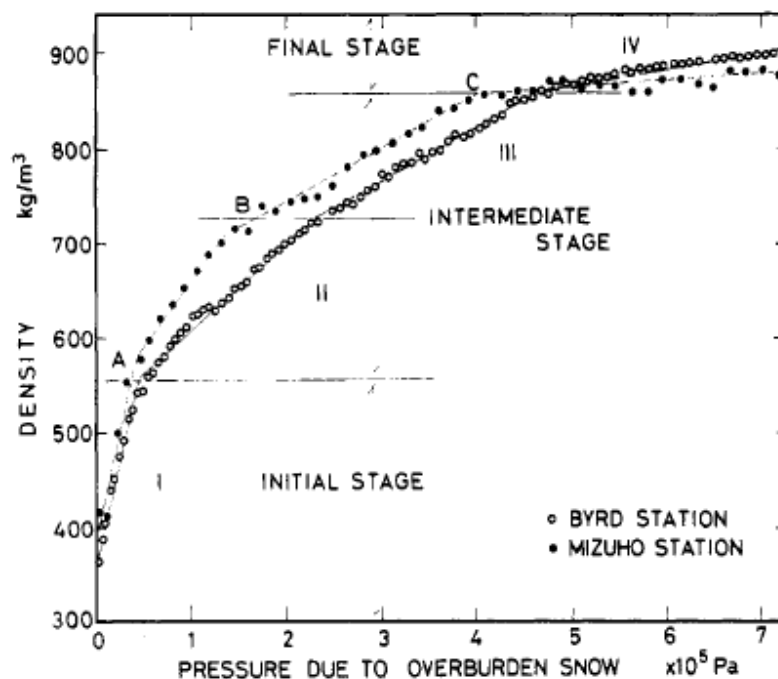
Figure A.1: Compaction of polar snow in Antarctica where the pressure from the overburden changes the density of the snow and ice. From *Maeno and Ebinumae* (1983).

A.1   Initial Stage: Seasonal Snow

The first stage of densification occurs in seasonal snow with densities between 0 to 550 kg/m^3. The densification at this stage is mainly due to the repacking of the snow particles as individual snow crystals move to fill up empty pore space (*Anderson and Benson*, 1963). If snow were thought of as perfect spheres of equal size, the maximum density that could be achieved through packing of granular aggregates is ~550 to 580 kg/m^3. For packing to be efficient, grains undergo mechanical destruction as the bonds fracture to allow movement (*Maeno and Ebinumae*, 1983).

Another key aspect to densification in this regime is sintering, or building of bonds between grains. The sintering process is governed by mass movement from the grains

towards the bonds in order to reduce the surface energy on the grains. *Maeno and Ebinumae* (1983) state that there are various mechanisms of pressureless sintering that include:

- surface diffusion

- lattice diffusion

- vapor transport

- boundary diffusion

- lattice diffusion from the grain boundary

- lattice diffusion from dislocations

Trying to model all the grain rearrangements and sintering processes are not feasible on a large scale. One way to incorporate all these factors is to assume that snow behaves like a viscous fluid at low strain rates ($\dot{\epsilon} < 1e^{-5}$). The viscosity relates the strain rate to compactive stress through a constitutive equation. From the constitutive equation, the change in density can be calculated for a given viscosity and stress (*Kojima*, 1967).

A.2   Intermediate Stage: Firn

At this stage, grain packing is no longer an effective method to reduce the pore space of the snow. Between 550 to 820 kg/m^3, different processes take over as densification becomes a slower process (Figure A.1). At these higher densities, a significant amount of overburden is required to create enough stress within the snow lattice. The

high pressure leads to plastic deformation of the snow grains and bonds, as they are irreversibly deformed to fill the remaining pore space.

The high pressures lead to pressure sintering, a more complex process than pressureless sintering at lower densities. In addition to the mechanisms of pressureless sintering, other processes like diffusional creep, dislocation, creep, and grain boundary sliding may also play a large role in the densification process (*Maeno and Ebinumae*, 1983). The mechanisms can be operating simultaneously or individually within the snow.

A.3 Final Stage: Ice

Once this stage is reached, most of the pore spaces have closed to create air bubbles. Densification between 820 to 917 kg/m^3 is achieved by reducing the size of the air bubbles. The reduction in the air bubble size can be attributed to large overburden stresses compressing the air within the bubbles.

APPENDIX B:

LITERATURE REVIEW OF SEISMIC

DETECTION OF AVALANCHES

B.1   Avalanche seismic signals

Avalanche detection using seismic equipment can be a useful tool for real-time avalanche monitoring systems (*Leprettre et al.*, 1996; *Bessason et al.*, 2007), however interpretation of the seismic signal can be difficult. Instrumented avalanche paths with multiple geophones were artificially triggered using explosives to perform detailed analysis of the seismic signal generated by avalanches (*Surinach et al.*, 2000, 2001). Seismic signals corresponded to the avalanche impacting obstacles in the avalanche path, a change in the paths slope, change in type of flow or avalanche type, and the stoppage of the avalanche, which all produce different wave trains. However, the beginning of the avalanche appears to not produce a significant seismic signal. *Surinach et al.* (2000, 2001) attribute the time lapse between the avalanche release and detection to the building of enough kinetic energy to generate a seismic signal. Therefore, a large time lapse will occur when the distance between the source and measurement station is large. This can be seen in Figure B.1, where the avalanche starts right after the explosion, E1 represents a change in slope (and the first detection of an avalanche), and E3 and E2 correspond to a change in type of flow (powder cloud develops).

Similar seismic signals can be observed for avalanches following the same path
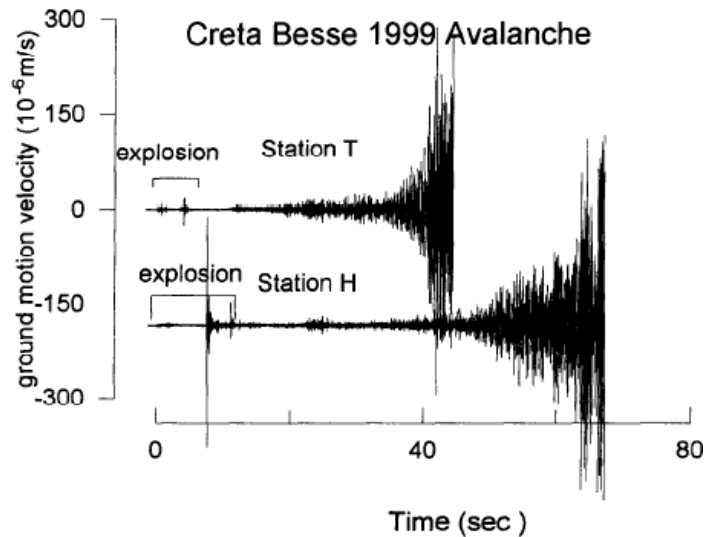
Figure B.1: From *Surinach et al.* (2000). Station H is in the runout zone and station T is mid-path. E1, E2, and E3 correspond to different arrival times of different seismic signals.

in both the time and frequency domain. The distribution of seismic energy in three component signals are also similar, even though the amplitude may differ (*Surinach et al.*, 2000). The amplitude difference is dependent on the avalanche size, as larger avalanches will produce higher ground motion velocities with similar frequency content.

Two geophones that record the same event will have different seismic signals and the distribution of seismic energy will be different at each measurement site. The major conclusion drawn from this study is that each measurement site will produce different seismic signals and therefore a characterization of the avalanche path is needed to understand seismic characteristics. *Surinach et al.* (2000) used the explosion to characterize the seismic characteristics of the avalanche path.

B.2   Equipment and Methods

Avalanche signals are located in the 2-40 Hz frequency band (*Leprettre et al.*, 1996). Monitoring systems that are currently in operation use three-component geophones or three-component accelerometers within the avalanche frequency band at a sampling rate of 100 or 200 Hz.

Two different studies provided details on the type and model of geophone used. The operational avalanche detection system in Iceland (*Bessason et al.*, 2007) uses triaxial and uniaxial accelerometers (Kinemetrics Inc. FBA-23 and Kinemetrics Inc. FBA-11, respectively) with a measurement range of 0.01 mm/s^2 to 9.8 m/s^2. A Sensor Netherland SM-6 geophone with natural frequency of 4.5 Hz was installed next to the accelerometers with a measurement range of 0.10 mm/s^1 to 86.6 mm/s^1. *Vilajosana et al.* (2007b) installed two 3-component Lennartz 3D-5 seismometers at their study site in Norway.

The locations and number of geophones were different from study to study. *Leprettre et al.* (1996) had two instrumented study sites with one geophone at each site. The geophones were placed near power sources, which corresponded to the valley bottom and 400 meters above a road, and both locations were not within the avalanche path. *Kishimura and Izumi* (1997) also placed one geophone adjacent to the avalanche path. *Bessason et al.* (2007) instrumented three different avalanche paths, placing one accelerometer and geophone at the base of each path right above the road. *Surinach et al.* (2000, 2001) used two to five sensors within a ski area boundary at various locations on the slope. One sensor was in the runout zone of a large avalanche path. *Vilajosana et al.* (2007b) also used two geophones, one placed within the runout zone of the avalanche and another placed 410 meters horizontally from the first.

B.3 Avalanche Monitoring Systems

Leprettre et al. (1996) first used geophones to automatically detect when an avalanche has occurred. A database was built up from various signals caused by avalanches, earthquakes, rock fall, thunder, helicopters, and animals. Each signal was divided up into three domains - time, time-frequency, and polarization - in attempt to differentiate between each signal. A signal would be classified as an avalanche through an elimination process by comparing the generated signal against the database of all the signals. Using this process, 12 out of 13 were correctly classified as avalanches. The timing of all the avalanche events occurred as soon as the new snow layer reached 35 cm, leading to a site specific rule, and generally occurred in clusters when the avalanche danger was elevated. Problems that they encountered were the lack of detection of small loose snow avalanches that do not produce significant seismic energy and visual confirmation of an avalanche.

Bessason et al. (2007) built on the previous study to create an operational, real-time avalanche detection system in northwest Iceland. Accelerometers and later geophones were placed at the bottom of three avalanche paths. A database of seismic signals was built, classifying into five categories: avalanches, rock falls and debris flows, earthquakes, traffic, and roadwork. The database includes around 6,000 events from 10 years of observations. Classification is similar to the above by comparing the generated signal to all know events in the database for the same path using the nearest neighbor method with the lowest proportional error. Ten parameters were compared for each signal: peak value, power, total duration, power duration, impact factor, characteristic frequency, half-power bandwidth, lower spectral limit, ratio of maximum to minimum amplitude, and frequency of maximum value. Using this

method, automatic detection of an avalanche was between 43 and 74% for the three paths. An updated classification system will be developed in the future that will use weather data in the classification process.